Title
High Frequency Multiferroic Devices

Author
Hu, Jinzhao

Publication Date
2020

Peer reviewed|Thesis/dissertation

UNIVERSITY OF CALIFORNIA

Los Angeles

High Frequency Multiferroic Devices

A dissertation submitted in partial satisfaction of the
requirements for the degree Doctor of Philosophy
in Mechanical Engineering

by

Jinzhao Hu

2020

ABSTRACT OF THE DISSERTATION

High Frequency Multiferroic Devices

by

Jinzhao Hu

Doctor of Philosophy in Mechanical Engineering

University of California, Los Angeles, 2020

Professor Gregory P. Carman, Chair

This dissertation focuses on high frequency multiferroic devices from both theoretical and experimental aspects. Some potential applications for high frequency multiferroic: antennas, logic and memory, will be presented in this dissertation. The introduction section provides a fundamental explanation on the multiferroic devices as well as the modeling methods for strain-mediated multiferroic systems. Former researches indicate that the composites of piezoelectric substrate and the magnetoelastic material show great potential on reducing both the devices' size as well as energy consumption.

Part I of the dissertation shows multiferroics for antenna applications. Conventionally, antennas such as dipoles and loops rely on an electromagnetic (EM) wave resonance. Therefore, the sizes of such antennas are within the same order of free space wavelength. Multiferroic antenna can transfer the EM wave into an acoustic wave, which has much smaller wavelength compared with the wavelength of the EM wave under the same frequency. In this way, multiferroic antennas

show a promising path for reducing the antenna system's size, weight and volume. Also, three multiferroic antennas: shear wave antenna, lamb wave antenna as well as tunable frequency broadband antenna are introduced in this section. The shear wave antenna and lamb wave antenna are studied experimentally, and the tunable frequency broadband antenna is studied theoretically. All of them show great potential on reducing the antenna's size.

Part II of this dissertation indicates other applications of multiferroic devices: logic and memory. For the logic aspects, a numerical simulation is performed on in-plane mode Bennett clocking systems. For memory aspects, a new concept for breaking the switch symmetry the high frequency control of the magnetization in nanodisk. In this part, a fully coupled finite element model is used to simulate the switch process of the magnetization in the nanodisks. This voltage-controlled process has potential be used in magnetic memory devices with very low energy dissipations.

The dissertation of Jinzhao Hu is approved.

Robert N. Candler

Christopher Lynch

Yuanxun Wang

Abdon E. Sepulveda

Gregory P. Carman, Committee Chair

University of California, Los Angeles

2020

For my beloved Weizhe Zhu

Table of Contents

List of Figures

List of Tables

VITA

Education:

2016-2018 M.S. – Mechanical Engineering
University of California, Los Angeles

2012-2016 B.S. – Aircraft Design and Engineering
Beihang University (BUAA), Beijing, China

Employment History:

2017-2020 Graduate Student Researcher
Translational Applications of Nanoscale Multiferroic Systems (TANMS)

Publications and conference presentations:

[1] **Jin-Zhao Hu**, John P. Domann, Qianchang Wang, Cheng-Yen Liang, Scott Keller, Gregory P. Carman and Abdon E. Sepulveda, "Modeling Incoherent Strain Mediated Multiferroic Bennett Clocking", arXiv preprint arXiv:2001.01405. (2020)

[2] Ruoda Zheng, **Jin-Zhao Hu**, Qianchang Wang, Victor Estrada, Gregory P. Carman and Abdon E. Sepulveda, "Strain-mediated Symmetry Broking Switch with Perpendicular Magnetic Anisotropy", arXiv preprint arXiv:2001.01018. (Co-first Authorship) (2020)

[3] Cai Chen, Justin Sablik, John P. Domann, Robert Dyro, **Jin-Zhao Hu**, Shalin Mehta, Zhuyun Xiao, Robert Candler, Gregory P. Carman and Abdon E. Sepulveda, "Voltage manipulation of magnetic particles using multiferroics", Journal of Physics D: Applied Physics. (2020)

[4] Qianchang Wang, **Jin-Zhao Hu**, Cheng-Yen Liang, Abdon. E. Sepulveda and Gregory P. Carman, "Voltage-induced strain clocking of nanomagnets with perpendicular magnetic anisotropies", Scientific reports, 9(1), pp.1-7. (2019)

[5] Joseph D. Schneider, Qianchang Wang, Yiheng Li, Andres C. Chavez, **Jin-Zhao Hu** and Gregory Carman, "RF voltage-controlled magnetization switching in a nano-disk", Journal of Applied Physics, 126(16), p.163903. (2019)

[6] Abdon E. Sepulveda, Gregory P. Carman, **Jin-Zhao Hu**, Elmer Wu, Zhi Yao, Joseph D. Schneider, Wenzhong Yan, Sidhant Tiwari, "Extremely Electrically Small Antennas Based on Multiferroic Materials", PCT/US Patent, PCT/US2019/045865. (Filed in August 2019)

[7] **Jin-Zhao Hu**, Wenzhong Yan, Gregory Carman, Abdon Sepulveda, "Electrical Small Multiferroic Antenna Enhanced by Energy Reelecting Components", 64th Annual Conference on Magnetism and Magnetic Materials (MMM), November 4-8, 2019, Las Vegas, Nevada, USA.

[8] **Jin-Zhao Hu**, John Domann, Scott Keller, Gregory Carman, & Abdon. E. Sepulveda, "Broadband Electrically Small Antennas with Strain Powered Multiferroics", APS March Meeting 2018, March 5-9, 2018, Los Angeles, California, USA.

[9] Abdon. E. Sepulveda, Cai Chen, Gregory Carman, **Jin-Zhao Hu**, & Kevin Landry, "Deterministic Magnetization Rotation in Nano Magnetoelastic Rings", APS March Meeting 2018, March 5-9, 2018, Los Angeles, California, USA.

[10] **Jin-Zhao Hu**, Qianchang Wang, John P. Domann, Scott M. Keller, Gregory P. Carman* and Abdon E. Sepulveda, "Broadband Electrically Small Antennas with Strain Powered Multiferroics", 62nd Annual Conference on Magnetism and Magnetic Materials (MMM), November 6-10, 2017, Pittsburgh, Pennsylvania, USA.

1. Introduction

1.1 Motivation

Wireless communications systems are ubiquitous in modern times, and antennas thus, play a crucial role in these communication terminals. The most common example is the cell phone, which has broken the limitations of space and distance, changing society significantly. These wireless devices bring humans to an extraordinary information-based society. For these wireless devices and an information-based society, then one of most key pieces of technology are antennas. Antennas are devices designed for reception and transmission of information in the free space. They encode the data in each device into electromagnetic (EM) waves, then form an enormous invisible network of information.

Modern antenna technology is based on James Clerk Maxwell's equations describing the relationship between magnetic and electrical fields which were published in 1865[1], and was invented by Heinrich Hertz in 1887 with a current dipole.[2] That basic design principle has been used, for about 120 years, on different types of antennas, such as wire loop, single dipole or micro stripe. These antennas convert the movement of electrons into EM waves by electrical resonance in conductive structures. Just like in mechanical resonance, system footprint and geometry for antennas have to be carefully manipulated to reach maximize radiation efficiencies. A lot of work has been conducted for that purpose.[3]–[11] Today, the sizes of antennas are usually limited to about $\lambda/4$, where λ is the free space wavelength of EM waves.

The competition between antennas' size and the available space in portable electronic devices is particularly problematic when it comes to longer wavelengths, for instance, VHF and UHF range. The wavelength must be long enough to ensure the diffraction ability for daily

communication. However, this results in antennas becoming relatively large compared to the communication devices. Especially in some space-sensitive devices like, for example, implantable medical devices. They usually work under medical implant communications service (MICS) band, which is relatively low and usually requires large antennas. Figure 1-1 (a) depicts the antennas in a capsule endoscope. The antenna has to be small enough for getting into human body. However, it sacrifices the radiation power and usually is bothered by Specific Absorption Rate (SAR) of the human body.[12], [13] Figure 1-1(b) shows another typical antenna for implantable medical devices. The antenna has better radiation power and efficiency. However, the volume of the antenna become relatively large.[14]

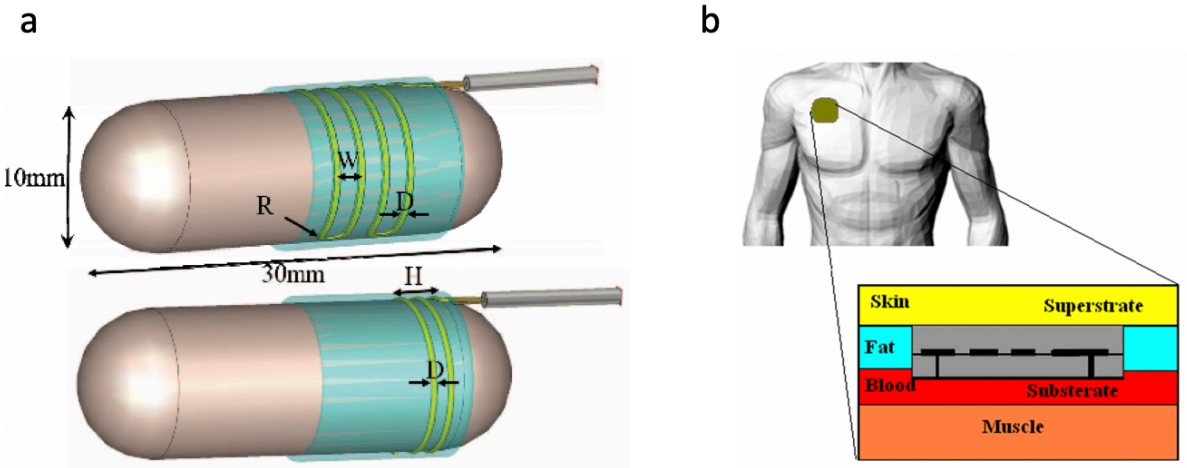

Figure 1-1: Typical antennas for implantable medical devices. (Figures from [13], [14])

Therefore, new approaches for transduction of EM waves are eagerly required. A composite system with multiferroic materials can convert mechanical waves to EM waves or conversely. The mechanical wave caused by a piezoelectric substrate will be transferred to the magnetoelastic material and will excite a magnetic current in it. Proper design will allow multiferroic antennas to be demonstrated under a wide frequency range, from VHF to UHF.

Because of the ultra-small wavelength of mechanical waves, the antennas based on these approaches can be dramatically reduced to small nanostructures. At the same time, the Ohmic losses associated with electron motion inside the conductors will also be significantly reduced.

Multiferroic nano-antennas bypass the limitation of Maxwell's equations and will have incredible application potential. For example, small antennas can be used to control nano-robots within human arteries and monitor the states of organs and report them to doctors in real-time. For daily communication, nano-antenna array will replace the bulky antennas in our cell phones and wearable devices, making more space for batteries or other functional structures. Similarly, for UAV, nano-antenna arrays can be patterned on the skin of the aircraft, save weight and reduce aerodynamic drag. This magnetic-current based nano-device will be the antenna that defines the future of bio-implantable devices, wearable devices and even internet of things.

Another potential application for high frequency multiferroic is magnetic computation. Including magnetic logic as well as magnetic memory. For example, magnetoresistive random-access memory (MRAM), which is widely used for computation systems' memory device due to its characteristics like non-volatility, high speed, and high efficiency.[15]–[17] However, the traditional methods that are used for controlling the magnetization rely on external fields or current to generate "Oersted fields".[15], [18], [19]

Figure 1-2 shows the cutting-edge promising way on controlling the magnetization. Both the current-based methods, spin transfer torque (STT) and giant spin hall effect (GSHE) and the voltage-based methods, (VCMA) and (VCM) have attracted a lot of research interests on both simulation and experiment. Strain-mediated multiferroic has potential to be used for building the most energy-efficient devices.[20]

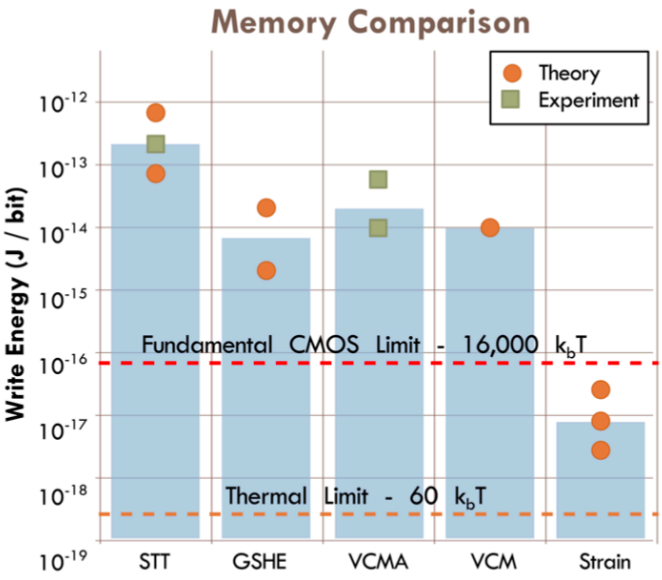

Figure 1-2: Energy dissipated to flip a bit of information. (Figure from [18])

1.2 About Multiferroics

1.2.1 Multiferroics, Magnetoelectric and Magnetoelasticity

Multiferroics are a group of materials that can possesses two or more primary ferroic order properties (ferromagnetism, ferroelectricity, ferroelasticity) in the same phase.[21]–[28] There are very few materials that show both ferroelectric and ferromagnetic properties simultaneously in one phase, especially at room temperature. The magnetoelectric effect (ME) is a phenomenon that describes how the electric and magnetic properties couple within a material. The simplest mathematical model used to understand the magnetoelectric effect, is the free energy equation in materials: [28]

$$F(\vec{E},\vec{H}) = F_0 - P_i^S E_i - M_i^S H_i - \frac{1}{2}\varepsilon_0\varepsilon_{ij}E_iE_j - \frac{1}{2}\mu_0\mu_{ij}H_iH_j - \alpha_{ij}E_iH_j + \cdots \qquad \text{Eq.1-1}$$

Where α_{ij} is magnetoelectric coefficient, P_i^S and M_i^S is the spontaneous electric polarization and spontaneous magnetization. Here the higher order terms are ignored to help simplify the equation. Further, the equation becomes:

$$P(\vec{E},\vec{H}) = -\frac{\partial F}{\partial E_i} = P_i^S + \varepsilon_0 \varepsilon_{ij} E_j + \alpha_{ij} H_j + \cdots \quad \text{Eq.1-2}$$

$$M(\vec{E},\vec{H}) = -\frac{\partial F}{\partial H_i} = M_i^S + \mu_0 \mu_{ij} H_j + \alpha_{ij} E_i + \cdots \quad \text{Eq.1-3}$$

If the value of $\frac{1}{2}\varepsilon_0 \varepsilon_{ij} E_i E_j + \frac{1}{2}\mu_0 \mu_{ij} H_i H_j + \alpha_{ij} E_i H_j$ is forced to be greater than 0, we can get the upper limit of magnetoelectric coefficient α_{ij} described as:

$$\alpha_{ij} > \varepsilon_0 \varepsilon_{ij} \mu_0 \mu_{ij} \quad \text{Eq.1-4}$$

It's clear that multiferroics are not the same as magnetoelectric materials. Multiferroics do not require magnetoelectricity and magnetoelectric materials do not necessarily have two or more primary ferroic order properties. The relationship is depicted in Figure 1-3 (b).

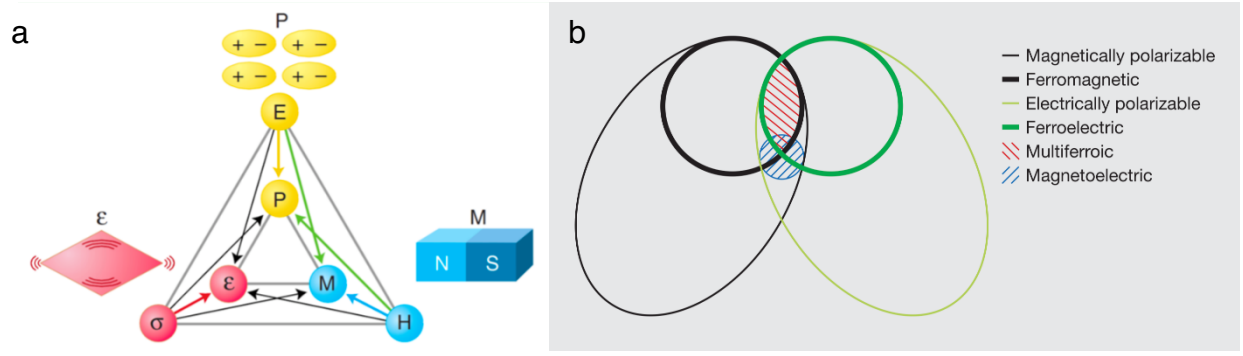

Figure 1-3: (a) Multiferroics (b) The relationship between multiferroic and magnetoelectric materials. (Figures from [27], [28])

One of the most famous multiferroics materials is BiFeO3, also be known as BFO. This material is a kind of perovskite crystal that exhibits both antiferromagnetism and ferroelectricity at room temperature. Since its discovery, BFO has attracted a lot of interest because of its

enormous physical significance and huge application potential. A summary of several types of multiferroic materials is given below.[29]–[34]

Table 1-1: Common multiferroics materials.

	Electric Order	Ferroelectric Transition Temp.	Magnetic Order	Ferromagnetic Transition Temp.
BiFeO3	Ferroelectric	~1103K	Antiferromagnetic	~643K
BiMnO3	Ferroelectric	~800K	Ferromagnetic	~100K
LuFe2O4	Ferroelectric	~330K	Ferrimagnetic	~220K
YMnO3	Ferroelectric	~950K	Antiferromagnetic	~77K
HoMnO3	Ferroelectric	~875K	Antiferromagnetic	~5/76K
…	…	…	…	…

From the table, it is shown that only BFO keeps its multiferroic properties below room temperature. However, the Dzyaloshinskii–Moriya (DM) interaction in antiferromagnetic materials can lead to a canting of the antiparallelly aligned spins. Further, that phenomenon results in weak ferromagnetism. The weak net magnetization will limit the applications for single phased multiferroics materials. As a solution, in some ferromagnetic–ferroelectric heterostructures, magnetoelectric effects can be achieved by the strain transfer between the materials interfaces.

Ferromagnetic–ferroelectric heterostructures achieve magnetoelectric effects using what is known as “magnetoelasticity”. Magnetoelasticity describes the coupling between magnetization and elastic strain. In 1822, James Prescott Joule measured the change in length of a rod of iron in a magnetic field with “a system of levers”[35], he found a strain of only about 1.2ppm in the rod. Following that, in 1864, Villari discovered that strain can also change the magnetization in a material.[36] These two phenomena are commonly referred to as Joulian magnetostriction and the

Villari effect.[18] However, for a long time, these experiments did not attract much interest from scientists. Even Joule himself thought this discovery had little technological merit.[35]

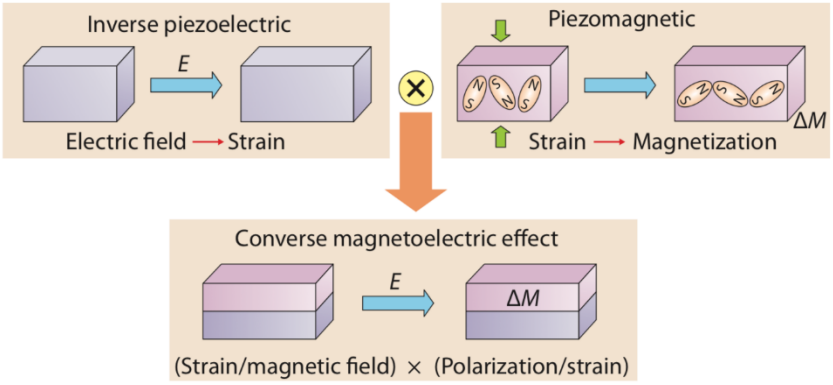

Figure 1-4: Ferromagnetic–ferroelectric heterostructures. (Figure from [37])

The turning point for this technology came after years. With the development of the microelectronics industry and discovery of room temperature magnetoelastic materials, people found that multiferroic magnetoelectric composite systems provide new routes for sensors, transducers, memories, spintronics and RF devices.[37]–[39]

One of the magnetoelastic materials with the most potential for practical applications is Terfenol-D. Terfenol-D is made by combining two binary rare earth alloys TbFe2 and DyFe2. It has high magnetoelasticity, high Curie temperature and low crystalline anisotropy.[40] The magnetostriction of Terfenol-D is the highest in room temperature with a saturation strain near 2400 ppm[34], [35], which indicates that this material has huge potential for converting mechanical energy into magnetization change.

1.2.2 Strain-Mediated Multiferroics Devices

Along with the development of the microelectronics industry, multiferroics devices are attracting more and more interest from both academia and industry. One of the most famous and successful examples is giant magnetoresistance (GMR). Magnetoresistive random-access memory

(MRAM) based on GMR multilayer structures have changed the course of history for humans by making the storage of information more accessible. This technology is non-volatile, has low power consumption and high speed, which makes it possible to store large amounts of information in a small disk.[41] The discoverers of GMR, Albert Fert and Peter Grünberg won the 2007 Nobel Prize in Physics because of this.

However, electric current-based multiferroic devices (including SOT, STT, GMR, MTJ devices) have a high Ohmic losses in nano-scale circuits. That phenomenon limits the operation frequency of the devices.[42]–[46] Under these circumstances, voltage-controlled magnetism that can eliminate the need for electric current has come into researchers' attention.[47]–[49] As mentioned in chapter 1.2.1, multiferroic magnetoelectric composite systems with ferromagnetic–ferroelectric heterostructures allow the strain-mediated control of magnetism. The strain-powered magnetic devices appear to be really energy efficient and can reach very high frequencies.[47]–[49] Figure 1-5 shows a typical strain-mediated ferromagnetic–ferroelectric heterostructure.

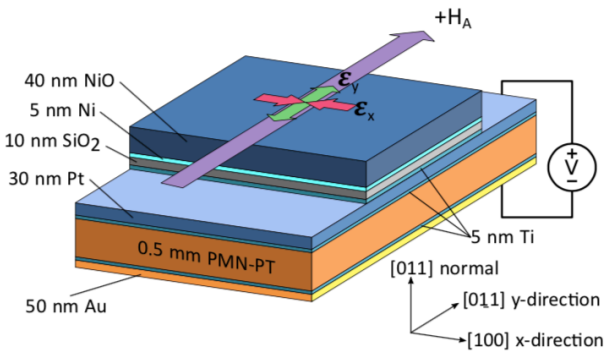

Figure 1-5: A typical ferromagnetic–ferroelectric heterostructure. (Figure from [50])

The magnetoelastic material (e.g., Nickel) is patterned atop of the piezoelectric substrate (e.g., PMN-PT).[50] When an electric field is applied through the PMN-PT substrate, the substrate will translate the piezo-strain to the magnetoelastic material, thereby changing the way in which

the material is magnetized. In this device, voltage, instead of current, is used to switch the magnetic state of the magnetoelastic material. In this way, the system avoids Ohmic losses.

The first device to use local piezo-strain to control the magnetization was fabricated by Jizhai Cui.[50] Figure 1-6 depicts this system.

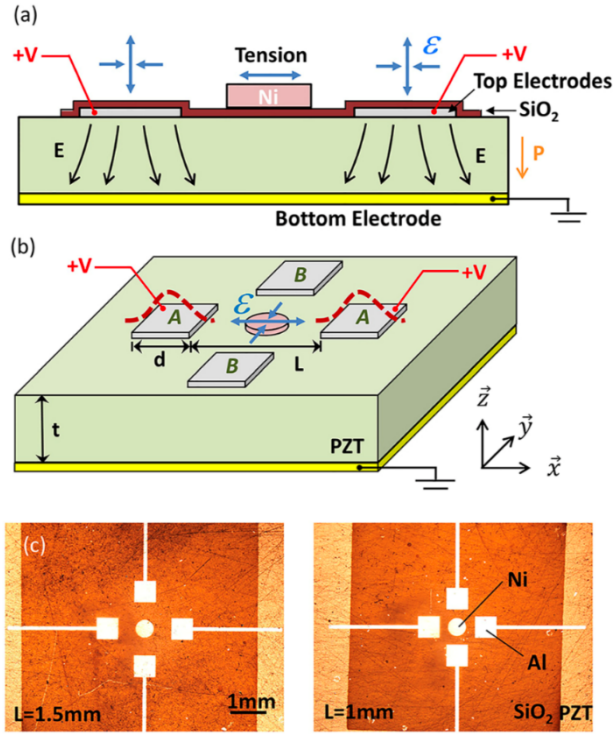

Figure 1-6: First strain-mediated magnetic device that uses local out-of-plane electric field. (Figure from [50])

As shown in Figure 1-6, on the bottom of the Pb[ZrxTi1-x]O3 (PZT) bulk (10mm×10mm×0.5mm), there is a global ground electrode. The control electrodes and magnetoelastic material (Nickel) islands are patterned on the top of the PZT substrate. In this design, the electric field will go from top to bottom. At last, on the top of the system, there is a dielectric layer SiO2 to prevent electric break down. The L in Figure 1-6 (c) and Figure 1-6 (d) indicates the distance between the electrodes and Ni island. Based on this design, Jizhai fabricated two devices: L=1.5mm and L=1mm. When the electric field is applied through from top to the

bottom, the PZT will generate local deformation because of the linear material prosperities of PZT. The local strain will in turn affect the near-by area, further transferring strain to the Ni island. Jizhai Cui et.al. made a finite element analysis (FEA) model to show the bi-axial strain produced by the local electrodes.

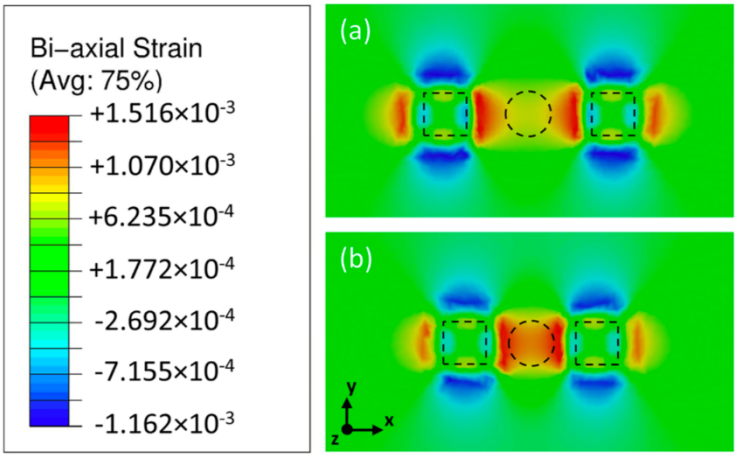

Figure 1-7: FEA simulation results for bi-axial strain with 1.5kV voltage applied. (Figure from [50])

As a result, Jizhai Cui et.al. observed the easy axis changes with magneto-optical Kerr effect (MOKE). This strain-mediated device shows that the local patterned electrodes on PZT substrate can successfully control the magnetism in magnetoelastic materials.[50]

Other strain-mediated devices, like strain-mediated acoustical wave antennas, strain-mediated binary memory devices, and strain-mediated Bennett clocking logic circuits[2], [45], [46] also show that this method is practical and ultra-energy efficient.

1.3 Micromagnetic magnetic simulations

As the strain-mediated devices develop, the systems have become more and more complex. One of the examples is the research on single domain. Magnetic single domain can reach the saturation magnetization. It has small size and extremely high flip energy efficiency. That makes

the multiferroic devices smaller and more efficient. Under these circumstances, simulation methods for strain mediated devices are required now more than ever. The small size of the devices also makes it possible for accurate finite element analysis modelling.

Here, two methods that can simulate the magnetization for single domain dots are introduced. One is based on finite elements methods. This model uses a fully coupled elastodynamics and micromagnetics on a point wise basis. The second system is modeled with an uncoupled single/macro-spin model assuming uniform strain induced magnetic anisotropy within the nanodot. These formulations can be used to predict the magnetization state changes in magnetoelastic nano-dots and/or arrays.

Finite Element Model: The fully coupled finite element approach assumes linear piezoelectricity in the electrostatic approximation, linear elastic, and negligible mechanical losses.[54] The low mechanical loss is reasonable because PZT operating at ultra-high frequencies has fairly low loss ($\tan\delta = 0.05$) and acoustic attenuation (400 dB/cm at 1GHz).[55] In all the formulations temperature effects are ignored.

The elastic strain tensor $\boldsymbol{\varepsilon}_{\mathrm{el}}$ and electric displacement $\mathbf{D}$ are represented as:

$$\boldsymbol{\varepsilon}_{\mathrm{el}} = s_E : \boldsymbol{\sigma} + d^t \cdot \mathbf{E} \qquad \text{Eq.1-5}$$

$$\mathbf{D} = d : \boldsymbol{\sigma} + e_\sigma \cdot \mathbf{E} \qquad \text{Eq.1-6}$$

where $\boldsymbol{\sigma}$ is the stress tensor, $\mathbf{E}$ is the electric field vector, s_E is the piezoelectric compliance matrix measured under constant electric fields, d and d^t are the piezoelectric coupling matrix and its transpose, and e_σ is the electric permittivity matrix measured under constant stress. The values for

s_E , d and e_σ can be found in the material library of the commercial Multiphysics software COMSOL:

$$s_E = \begin{bmatrix} 1.65\text{e}-11 & -4.78\text{e}-12 & -8.45\text{e}-12 & 0 & 0 & 0 \\ -4.78\text{e}-12 & 1.65\text{e}-11 & -8.45\text{e}-12 & 0 & 0 & 0 \\ -8.45\text{e}-12 & -8.45\text{e}-12 & 2.07\text{e}-11 & 0 & 0 & 0 \\ 0 & 0 & 0 & 4.35\text{e}-11 & 0 & 0 \\ 0 & 0 & 0 & 0 & 4.35\text{e}-11 & 0 \\ 0 & 0 & 0 & 0 & 0 & 4.26\text{e}-11 \end{bmatrix} 1/Pa$$

$$d = \begin{bmatrix} 0 & 0 & 0 & 7.41\text{e}-010 & 0 & 0 \\ 0 & 0 & 7.41\text{e}-010 & 0 & 0 & 0 \\ -2.74\text{e}-010 & -2.74\text{e}-010 & 5.93\text{e}-010 & 0 & 0 & 0 \end{bmatrix} \text{C/N}$$

$$e_\sigma = \begin{bmatrix} 3130 & 0 & 0 \\ 0 & 3130 & 0 \\ 0 & 0 & 3400 \end{bmatrix}$$

The precessional magnetization dynamics for the single domain magnetoelastic dot are governed by the Landau-Lifshitz-Gilbert (LLG) equation[49], [50]:

$$\frac{\partial \mathbf{m}}{\partial t} = -\mu_0 \gamma (\mathbf{m} \times \mathbf{H}_{\text{eff}}) + \alpha_{\text{G}} \left(\mathbf{m} \times \frac{\partial \mathbf{m}}{\partial t} \right) \qquad \text{Eq.1-7}$$

where $\mathbf{m}$ is the normalized magnetization vector, μ_0 is the vacuum permittivity, γ is the gyromagnetic ratio (~1.76e11 Hz/T[45]), $\mathbf{H}_{\text{eff}}$ is the effective magnetic field, and α_{G} is the Gilbert damping parameter.

In both the fully coupled and single/macro-spin models, the magnetoelastic dot is amorphous and external applied magnetic fields are absent. The effective magnetic field derived from the total energy density is given by:

$$\mathbf{H}_{\mathrm{eff}} = -\frac{1}{\mu_0 M_s}\frac{\partial \mathrm{E}_{\mathrm{tot}}}{\partial \mathbf{m}} = \mathbf{H}_{\mathrm{ex}} + \mathbf{H}_{\mathrm{d}} + \mathbf{H}_{\mathrm{me}}(\mathbf{m}, \boldsymbol{\varepsilon}) \quad \text{Eq.1-8}$$

where $\mathrm{E}_{\mathrm{tot}}$ is the total energy density, $\mathbf{H}_{\mathrm{ex}}$ is the effective exchange field, $\mathbf{H}_{\mathrm{d}}$ is the effective demagnetization field, and $\mathbf{H}_{\mathrm{me}}(\mathbf{m}, \boldsymbol{\varepsilon})$ is the effective magnetoelastic field. The effective magnetoelastic field is dependent on the total strain ($\boldsymbol{\varepsilon}_{\mathrm{tot}}$) which is the sum of the elastic strain ($\boldsymbol{\varepsilon}_{\mathrm{el}}$-Eq.1-5) and magnetoelastic strain ($\boldsymbol{\varepsilon}_{\mathrm{m}}$). For amorphous materials, the magnetoelastic strains are given by:

$$\varepsilon_{ij}^{m} = 1.5\lambda_s\left(m_i m_j - \frac{1}{3}\right), \quad i = j \quad \text{Eq.1-9}$$

$$\varepsilon_{ij}^{m} = 1.5\lambda_s m_i m_j, \quad i \neq j \quad \text{Eq.1-10}$$

where λ_s is the saturation magnetostriction for the material. The total strain $\boldsymbol{\varepsilon}_{\mathrm{tot}}$ is related to the displacement $\mathbf{u}$ by $\boldsymbol{\varepsilon}_{\mathrm{tot}} = \frac{1}{2}(\nabla\mathbf{u} + (\nabla\mathbf{u})^{\mathrm{T}})$. For the magnetoelastic dot, the stress tensor $\boldsymbol{\sigma}^{\mathrm{dot}}$ is related to the elastic strain $\boldsymbol{\varepsilon}_{\mathrm{el}}^{\mathrm{dot}}$ as $\boldsymbol{\varepsilon}_{\mathrm{el}}^{\mathrm{dot}} = \mathbf{C}^{-1}\boldsymbol{\sigma}^{\mathrm{dot}}$, where $\mathbf{C}$ is the elastic stiffness tensor. Finally, the stress and mechanical displacements distribution is governed by the elastodynamics equation $\rho\frac{\partial \mathbf{u}^2}{\partial^2 t} - \nabla\cdot\boldsymbol{\sigma} = \mathbf{0}$, where ρ is the mass density. [58], [59]

The weak forms of the LLG equation are solved using the finite element method with an implicit time stepping scheme and backward differentiation formula (BDF). To decrease solution time, the system of equations is solved using a segregated solution approach, which splits the solution process into substeps using a damped Newton's method.[60] The above system of equations is fully coupled between magnetics and mechanics. Specially, the point wise strain and magnetic values are re-calculated every time-step and iterated until the solution converges before proceeding into the next time step.

Single/Macro Spin Model: The second formulation uses a single/macro-spin simulation to solve dynamics described by the Landau-Lifshitz-Gilbert (LLG) equation (Eq. 1-7). However, the magnetization is represented as a single spin instead of spatially varying field. Unlike the fully coupled model, $\mathbf{H}_\mathrm{d}$ is derived from the demagnetization factors: $\mathrm{H}_\mathrm{i}^\mathrm{d} = -\mathrm{N}_\mathrm{i} \times \mathrm{m}_\mathrm{i}$, where $\mathbf{N}(\mathrm{N}_\mathrm{x}, \mathrm{N}_\mathrm{y}, \mathrm{N}_\mathrm{z})$ is an oblate spheroid, demagnetization factors are given as[61]:

$$\mathrm{N}_\mathrm{x} = \mathrm{N}_\mathrm{y} = \frac{1 - \mathrm{N}_z}{2} \qquad \text{Eq.1-11}$$

$$\mathrm{N}_\mathrm{z} = \frac{x^2}{(x^2 - z^2)^{3/2}}\{(x^2 - z^2)^{\frac{1}{2}} + z \cdot [\arctan\left(\frac{z}{(x^2 - z^2)^{\frac{1}{2}}}\right) - \frac{\pi}{2}]\} \qquad \text{Eq.1-12}$$

$\mathbf{H}_\mathrm{me}$ is calculated assuming constant strain under a known uniform electric field. Thus, the single/macro spin model uses only elastic strains determined from the piezoelectric part of the finite element formulation at specified voltage inputs. The simulation volume of the single/macro spin simulations is a three-dimensional oblate spheroid.

The single/macro spin model solves the LLG equation using dynamic MH loops resulting in significantly shorter solution times and acceptable error with respect to the fully coupled model. During the calculation, the source fields $\mathbf{H}_\mathrm{eff}$ were re-calculated every time step in increments of 1 ps.

One of the very first fully coupled models, in which the magnetoelastic strain will affects the total strain of the system, was built by Cheng-Yen Liang in 2014. The calculation process is shown in Figure 1-8.

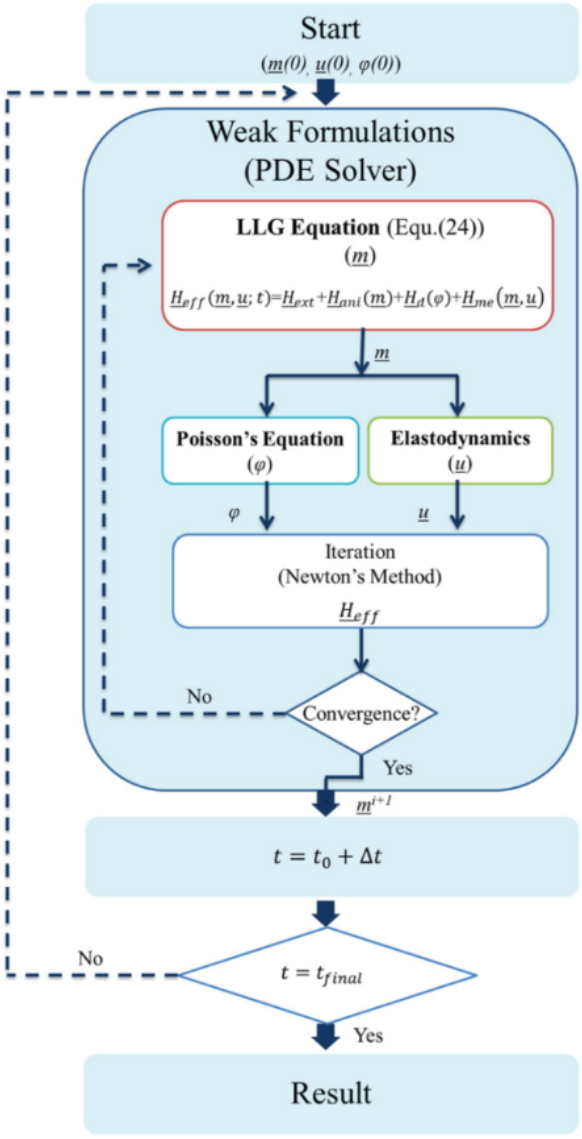

Figure 1-8: Flowchart of the fully coupled FEM simulation. (Figure from [62])

The first publication for this fully coupled model was in 2014. Cheng-Yen Liang designed a bi-stable memory device based on single domain.[63] Figure 1-9 schematically shows the layout and setting of this strain-mediated device.

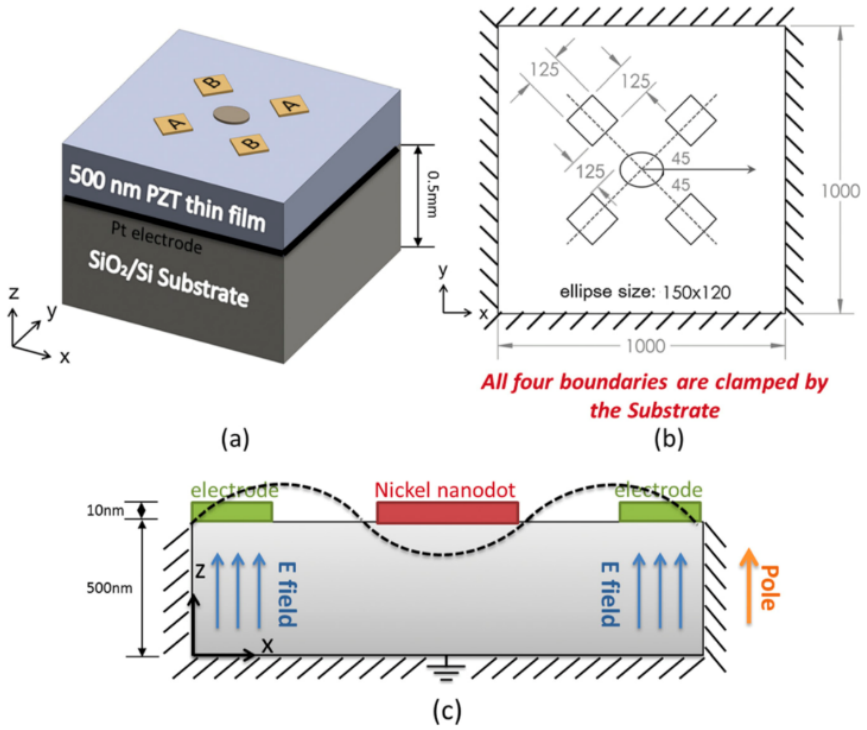

Figure 1-9: Bi-stable single domain memory device. (Figure from [63])

With this model, Liang showed that this bi-stable memory device can switch from one state to another successfully. Figure 1-10 shows the performance of this device. The top row shows the single domain magnetization, while the bottom row shows the principal strains when the electric fields are put through the electrode pairs. With an applied field from the bottom to the top, if voltage is induced on the electrode pairs in the correct sequence, the magnetization can switch from one state to another with an energy cost of 80 femtojoules (fJ).

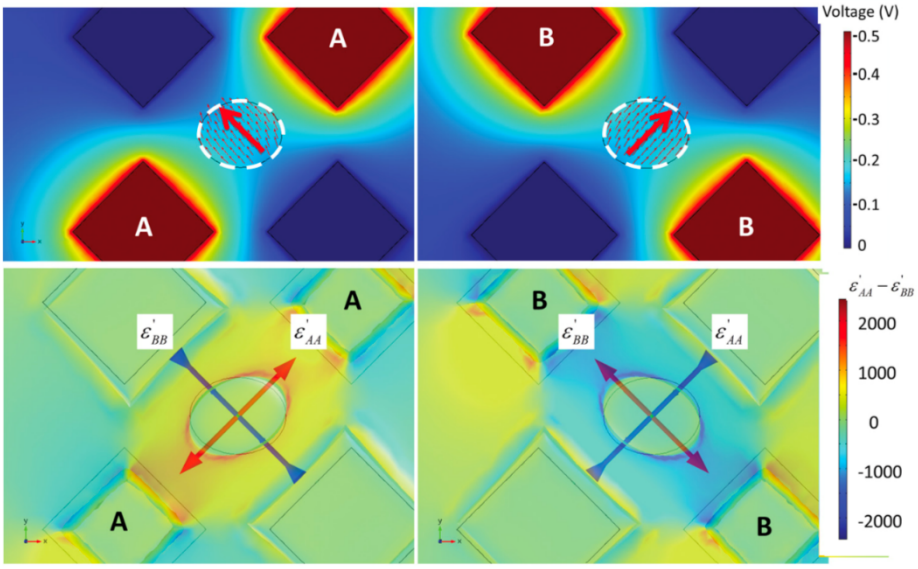

Figure 1-10: Performance of the memory device. (Figure from [63])

Finally, in 2017, Ayan Kumar Biswas fabricated this device successfully. The test results show that the fully coupled model is rather accurate. Figure 1-11 shows the experimental image of this device. The MFM images show that the bi-stable memory device can store the binary information successfully under room temperature ---- just as the model predicted.[63]

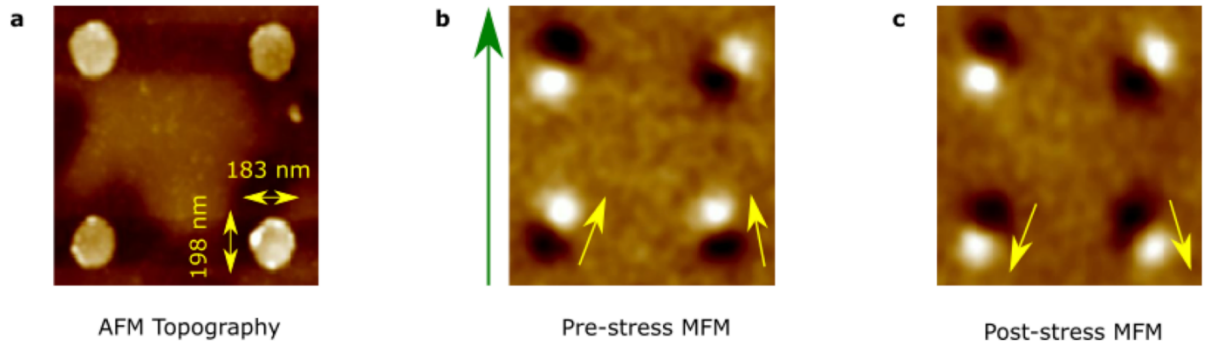

Figure 1-11: Experiment on this device. (Figure from [63])

This model shows great potential and accuracy on predicting the micro-magnetics dynamics. The fully coupled model has been successfully used for predicting the performance of

different devices and phenomena. Such as: spin waves, domain walls in ring, perpendicular magnetic anisotropy and memory devices with pretty accurate results.[64]–[66]

Part I

Multiferroic Antennas

2. Shear Wave Antenna

This chapter introduces a prototype of one kind of electrically small multiferroic antenna that based on shear wave. Conventionally, antennas such as dipoles and loops rely on an electromagnetic (EM) wave resonance, therefore the sizes of such antennas are within the same order of free space wavelength. Electrically small antennas (i.e. size < $\lambda/10$) [67]–[70] at ultra-high frequency hold promises for reducing the antenna system's size, weight and volume, yet state-of-the-art electrically small antennas confront a daunting challenge. So far, electrically small antennas radiate poorly when placed near a conducting surface because of platform effects. Recently, induced strain-mediated multiferroic composites interconvert between alternating magnetization and mechanical strain wave with ultra-high energy efficiency due to negligible current and Ohmic loss.[71]–[76] Several reports of such devices, modified from thin-film bulk acoustic resonator (FBAR), have demonstrated a new concept on electrically small antenna. However, until now, fabrication challenges hindered attempts at forming large scale antenna arrays to improve the signal strength.

In this work, a multiferroic shear wave antenna that based on mechanical resonance is designed. The antenna combines three main parts: the electrodes, the magnetoelastic resonators and the piezoelectric substrate. Here, Gold (Au) is used as the material for electrodes, Nickel (Ni) is used as the material for magnetoelastic resonators and Lithium Niobate ($LiNbO_3$) is used as the piezoelectric substrate. In this work, a numerical finite element model is used to predict the antenna's performance and optimize it. Based on the results, a device is built and tested, the results give us a magnetic-field-dependent signal under the vector network analyzer (VNA) electronics. The results indicate a new path for building a large-scale multiferroic antenna array.

2.1 Introduction of multiferroic antenna

Strain powered antennas have a potential to generate electromagnetic (EM) wave with nanostructure. Figure 2-1 shows the transduction process of multiferroic antenna. The electromagnetic (EM) waves excite the magnetic flux oscillating within the magnetoelastic-material-based resonators. The resonators that are patterned on the top of the piezoelectric substrate will also mechanically oscillate due to the magnetoelastic effect. A mechanical wave is also induced across the piezoelectric substrate that is attached to the resonator. Because of the piezoelectric effect, the substrate will transfer the mechanical wave into an electrical signal through a voltage difference. This process is reversible, which means this antenna can both receive and radiate an EM wave signal.

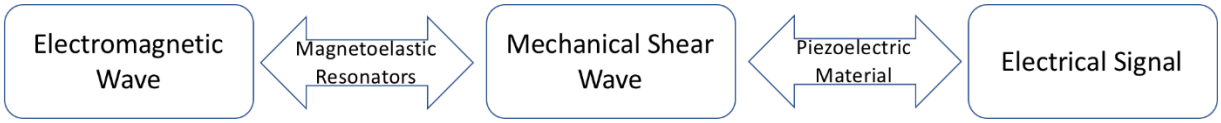

Figure 2-1: Transduction process of multiferroic antenna.

The concept of using magnetic materials to generate electromagnetic radiation can be tracked back to 1961 where Bell Telephone Laboratories. J. H. Bowen et al. developed a method that used high-intensity vibrations in magnetic materials to generate radiation. He used ferromagnetic yttrium iron garnet (YIG) spheres and obtained an output of $6W/cm^3$.[67] Later, from 1973 to 1990, researchers like R. Mindlin and P. C. Y. Lee used piezoelectric materials to provide mechanical vibrations. They analytically proved that this structure could generate $25\mu W/cm^2$ of radiation power.[68], [77], [78] More recently, researchers like Scott Keller and Paul Nordeen considered using acoustical wave propagation to receive EM wave from free space.[2], [62] However, a practical strain powered nano-antenna was finally built and tested in 2017.[80]

This antenna is based on several theoretical works made by different researchers.[71], [72], [75], [76] Here the process on how this antenna was developed is introduced.

In 2015, Zhi Yao from UCLA published a paper: "Bulk Acoustic Wave-Mediated Multiferroic Antennas: Architecture and Performance Bound".[71] In this paper, she developed with a multiferroic sandwich structure design that combined piezoelectric materials and magnetoelastic materials. This structure was designed to use Bulk Acoustic Wave (BAW) to radiate EM wave to free space.

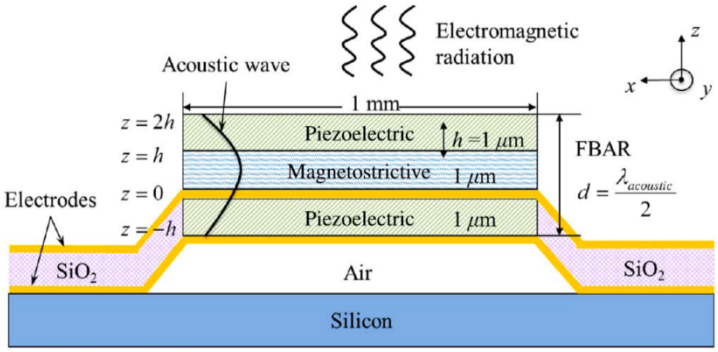

Figure 2-2: A sandwich structure that can generate EM radiation. (Figure from [71])

In this structure, the piezoelectric material provides the mechanical vibration that is generated by the input voltage. The thickness of the structure must also be selected carefully to maximize the radiation efficiency. However, as mentioned before, the wavelength of the mechanical waves is ultra-small compared to the wavelength of electromagnetic waves. In this case, the structure for detecting the mechanical wave will be much smaller than the structure for detecting the original EM wave. That is the key to reduce the size of this antenna.

This structure forms a resonator. When the antenna is vibrating around its natural frequency, the efficiency is maximized. Zhi Yao also calculated the natural frequency of this structure and

found it to be around 1.03 GHz. At last, she predicted that this antenna had a radiation power of 0.3W/mm^2.

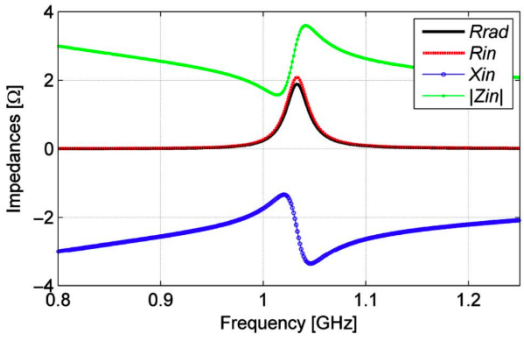

Figure 2-3: Input impedance and radiation resistance for a reference area of 1 mm^2. (Figure from [71])

The first attempt to fabricate this BAW sandwich structure antenna was completed by Sidhant Tiwari in 2016. He employed very clever fabrication steps to build a floating resonator.

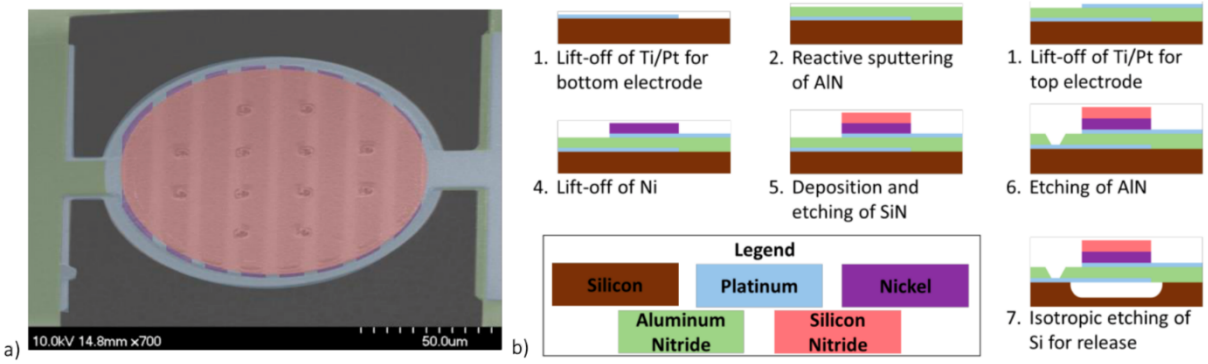

Figure 2-4: Fabrication of the sandwich structure resonator. (Figure from [72])

For the piezoelectric material, Sidhant Tiwari used Aluminum Nitride, because of the ultralow losses in this kind of piezoelectric material. For the magnetoelastic material, he chose

Nickel, because of its mature fabrication protocols. After finishing this device, the researcher tested it with an AC input of 3.2 GHz.

Unfortunately, Tiwari did not get a significant enough signal from this antenna. One of the reasons was that the strain that be transferred to the Nickel is too weak and thus the exiting flux was negligible. However, these tests and fabrication proved to be quite meaningful.

Since Paul Nordeen and Sidhant Tiwari both failed to build a practical nano-antenna, it seemed that strain powered nano-antenna could only function theoretically. However, John Domann reexamined the strain-mediated heterostructures antenna from a mathematical perspective and his calculation showed that strain powered antenna were practical and that it was possible to get enough radiation efficiency, which gave a new possibility to strain powered antennas again.

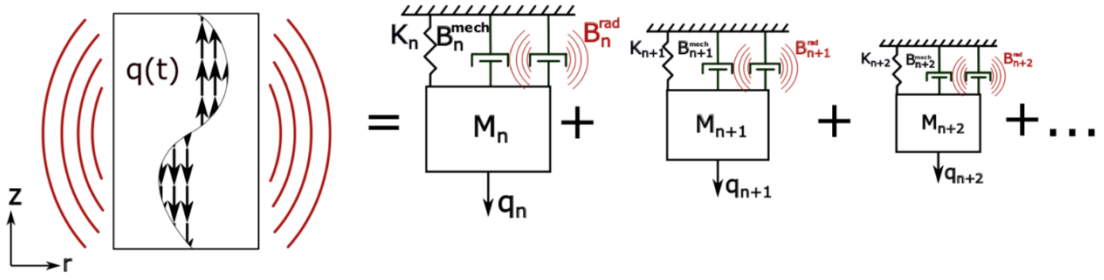

Figure 2-5: Modal representation of EM radiation from a strain powered antenna. (Figure from [76])

John Domann considered the strain powered antennas as a system like the one depicted in Figure 2-5. By solving the model as the response of n uncoupled oscillators, John Domann developed a way to calculate the radiation power and efficiency near the antennas' resonance frequency.

2.2 Design of the shear wave antenna

In order to avoid the strain transfer efficiency problem, a shear wave antenna is designed. In this design, the resonators are patterned between the electrodes on the top of piezoelectric substrate. As shown in Figure 2-6 (a), every single resonator as well as the electrode by its side is a singular small antenna, an antenna array is deployed to increase the signal strength and includes redundancy to accommodate fabrication tolerances. For an antenna array, the structure in Figure 2-6 (a) is laid out periodically and forms the entire structure.

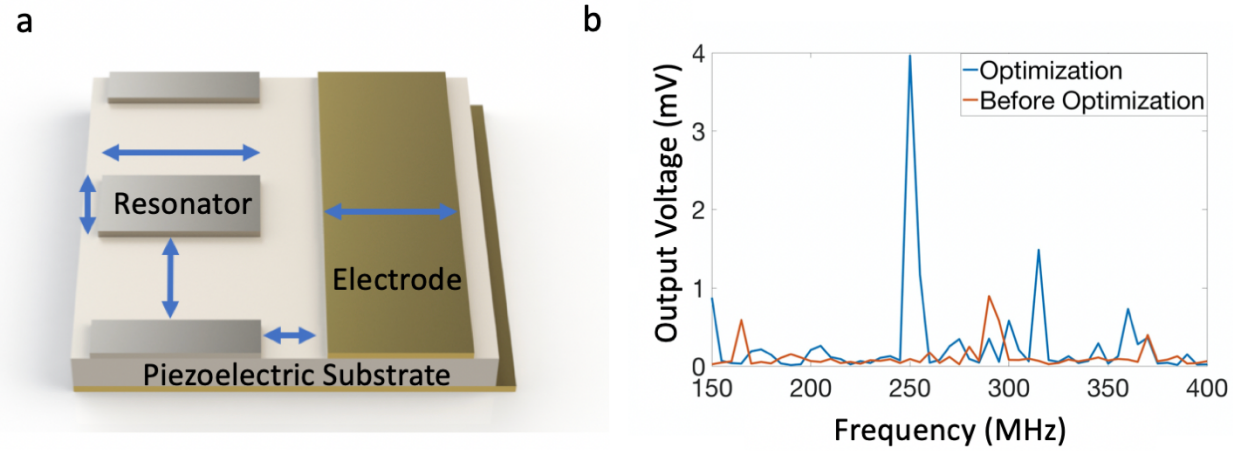

Figure 2-6: (a) Optimized parameters of shear wave antenna. (b) Represented optimization results.

In order to increase the output signal strength, Monte-Carlo optimization method is used to optimize the geometry parameters. The optimized parameters are shown in Figure 2-6 (a), including: the length and width of the resonator, the width of the electrode, the distance between

electrode and the resonators, as well as the distance between resonators. Figure 2-6 (b) shows optimization results of the output voltage on the electrode for the receiving mode of the antenna. After optimization, the output voltage on target frequency is increased dramatically.

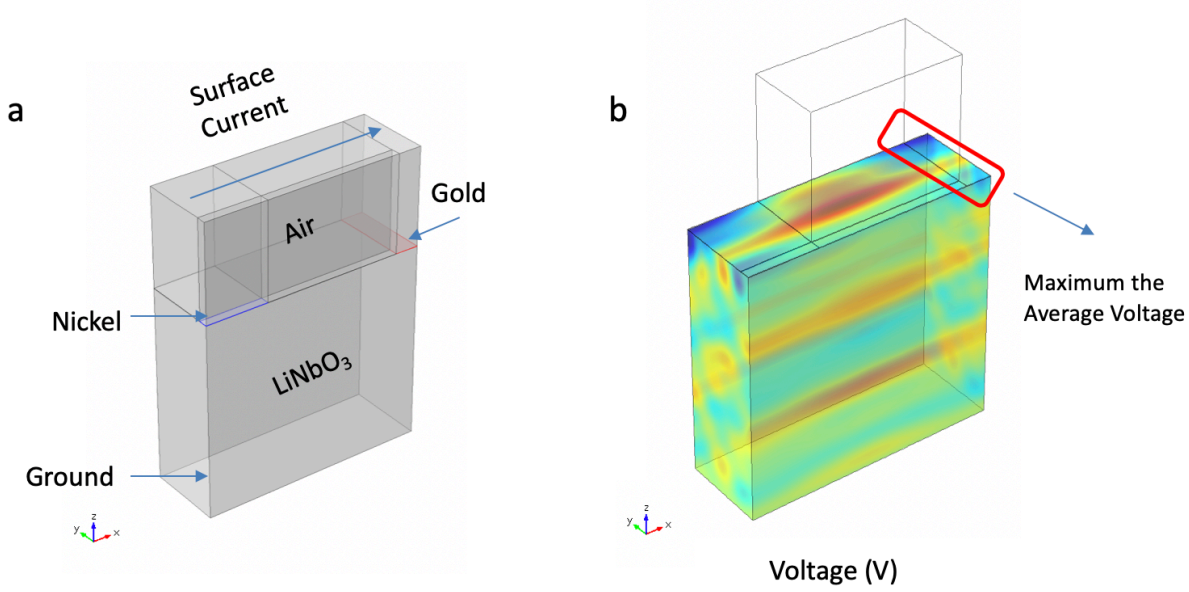

Figure 2-7: Optimization model for multiferroic shear wave antenna. (a) Geometry set-up of the finite element model. (b) Voltage plot in the model and optimization object.

Figure 2-7 (a) shows the simulation set-up of the optimization finite element model. In the model, there are several components: air, Gold electrode, Nickel resonator and Lithium Niobate ($LiNbO_3$) substrate. In order to reduce the calculation difficulties and the degree of freedom in the finite element model, here, the Gold electrode is only half width of the real electrode's width, the Nickel resonator has half of the real resonator's width and length. But both of them have the same thickness as the real one. This model replicates the smallest possible periodic structure of the system. Figure 2-7 (b) shows the voltage plot from the finite element model. The color difference indicates the voltage difference in different region. In this optimization model, Monte-Carlo method is applied for maximum the output voltage on the electrode pad.

In this finite element model, the input is the surface current as shown in Figure 2-7 (a). The surface current here is transferred to the EM wave by the Maxwell equations and electromagnetic wave equations:

$$\begin{aligned} \nabla \cdot \mathrm{E} &= 0 \\ \nabla \cdot \mathrm{B} &= 0 \\ \nabla \times \mathrm{E} &= -\frac{\partial \mathrm{B}}{\partial t} \\ \nabla \times \mathrm{B} &= \mu_0 \varepsilon_0 \frac{\partial \mathrm{B}}{\partial t} \end{aligned} \qquad \text{Eq.2-1}$$

Where E is the electrical field, B is the magnetic field, μ_0 is the permeability in vacuum and ε_0 is the permittivity in vacuum.

After the EM wave is created, the magnetoelastic resonators can sense the magnetic field component in the EM wave and transfer it into strain. By solving the elastodynamics equation as well as the piezoelectricity coupling equation mentioned in section 1.3, the strain can be transferred into voltage. By using the Monte-Carlo method we were able to optimize the geometries of the components in the multiferroic shear wave antenna. These components include: the length and width of the resonator, the width of the electrode, the distance between the electrode and the resonator, and the distance between resonators.

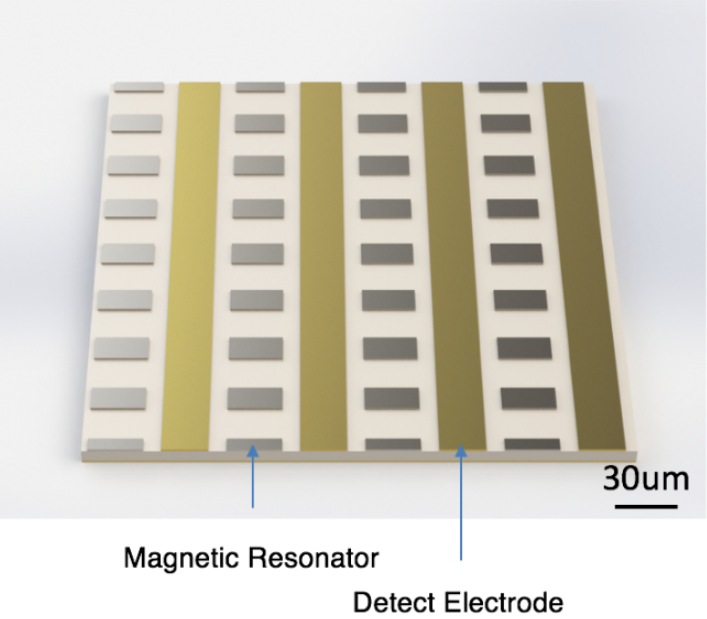

Figure 2-8: Antenna array's structure description.

The Monte-Carlo optimization analysis yielded the antenna array structure shown in Figure 2-8 (not to scale). For the real fabrication, as mentioned before, Nickel is chosen as the material for the magnetoelastic resonators, Au as the material for the electrodes and LiNbO3 as the material for the piezoelectric substrate. As can be seen, there is an array of rectangular Nickel magnetoelastic resonators (~65.2um x 9.6um um for ~250 MHz) on the top surface of the LiNbO3 wafer (100um thick). By adjusting the area of the antenna, different signal strengths can be obtained. The exact thickness, length and width for Ni resonators were optimized using the Monte-Carlo optimization method. There are also strip electrodes on the surface with another ground electrode on the bottom. This produces an induced electric field through the thickness of the substrate. The LiNbO3 wafer is a Z-cut to maintain a low loss factor when operating at ~250 MHz and maximize the out-of-plane voltage through the thickness. The in-plane electrode dimensions

on the LbNbO3 wafer minimize the voltage leakage as well as produces impedance matching to a 50 Ohm feed circuit.

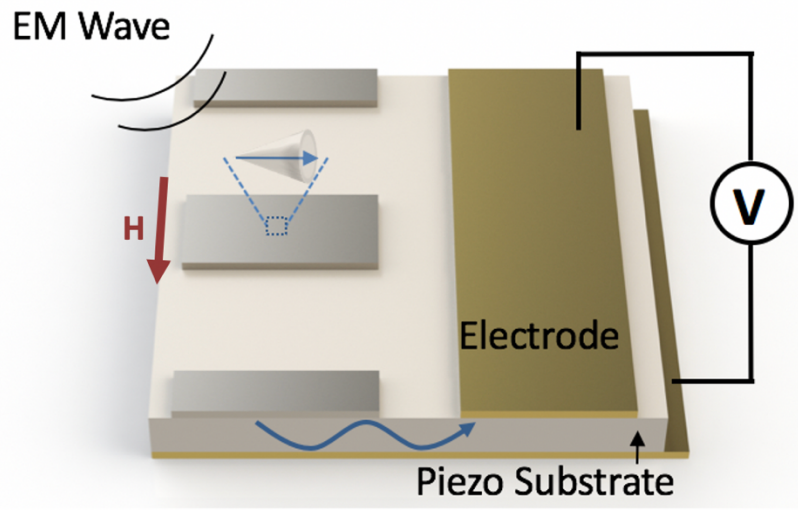

Figure 2-9: Shear wave antenna operating principles.

Figure 2-9 shows the operating principles of this receive antenna. An incoming EM wave impinges upon the Ni resonators producing a magnetic spin oscillation in the Ni elements as shown in the figure, i.e. from the magnetic field (H) component of the EM wave. The spin oscillation of the Ni resonators produces a mechanical shear wave in the piezoelectric substrate. The shear wave in the piezoelectric substrate induces a voltage on the electrodes. The voltage output is recorded using standard VNA electronics. The magnetic resonators ($9.6um \times 65.2um \times 400nm$) are designed to respond to the in-plane magnetic field (H) component aligned to the short axis of the resonators. Figure 2-9 shows the design orientation for the incoming magnetic field.

2.3 Test of the shear wave antenna

With the design discussed in section 2.2, the shear wave antenna was fabricated in the California Nano System Institute (CNSI) using photolithography and e-beam physical vapor

deposition. After the features of the electrodes/resonators are patterned with photoresist, e-beam physical vapor deposition is used to deposit Au electrodes and the Ni resonators with optimized parameters on the top of ultra-thin $LiNbO_3$ substrate (100um). After fabrication, the multiferroic shear wave antenna was assembled with a PCB board with wire bonding technology. Then a loop antenna was used to test the multiferroic shear wave antenna.

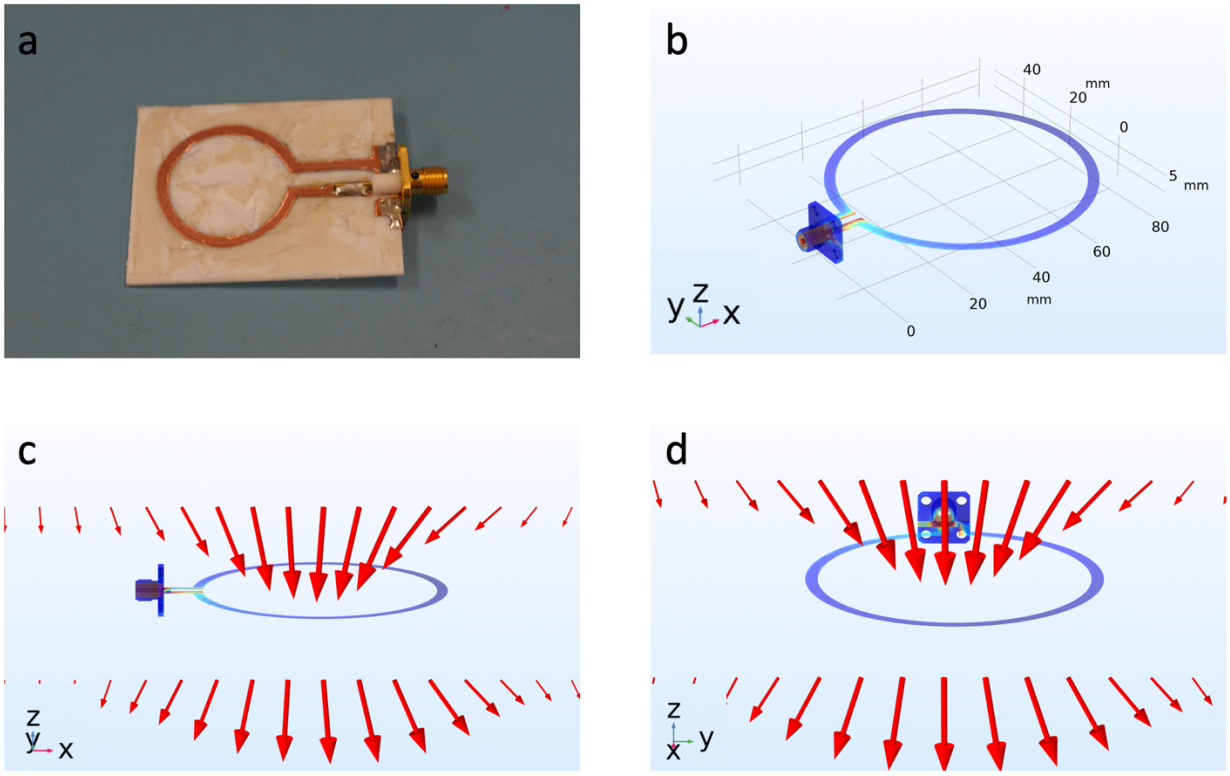

Figure 2-10: (a) A picture of the loop antenna. (b) Finite element model of a loop antenna with SMA connector. (c) Magnetic field distribution of the loop antenna in x-z plane. (d) Magnetic field distribution of the loop antenna in y-z plane.

Figure 2-10 shows the loop antenna used for this testing. Figure 2-10 (a) shows the picture of the real loop antenna. The loop antenna is basically a SMA connector connected to the conducting Copper layer on the PCB board which is patterned as loop shape. Based on this structure, a finite element model is used to predict the magnetic field radiated by this loop antenna. Figure 2-10 (b) shows how the finite element model looks like. This modeled antenna is

surrounded by air and a perfectly matched layer boundary condition is applied to the air. Here, the color difference indicates the current density's difference in different place of the loop antenna. Figure 2-10 (c) shows the magnetic field generated by the loop antenna for 300 MHz's input voltage. This figure mainly focuses on x-z plane. The red arrows here indicate the direction of the magnetic field at different locations. Here, most of the magnetic field is aligned to the z direction. However, there are still some components in x-y plane. Figure 2-10 (d) shows the magnetic field generated by the loop antenna in y-z plane. A similar phenomenon is observed here, i.e., most of the magnetic field is along with the z direction, but there still are some components in x-y plane. As mentioned in section 2.3, the multiferroic antenna will mainly response to the in-plane magnetic field components. Since the loop antenna can provide x-y plane magnetic field components, it can be used for the real test.

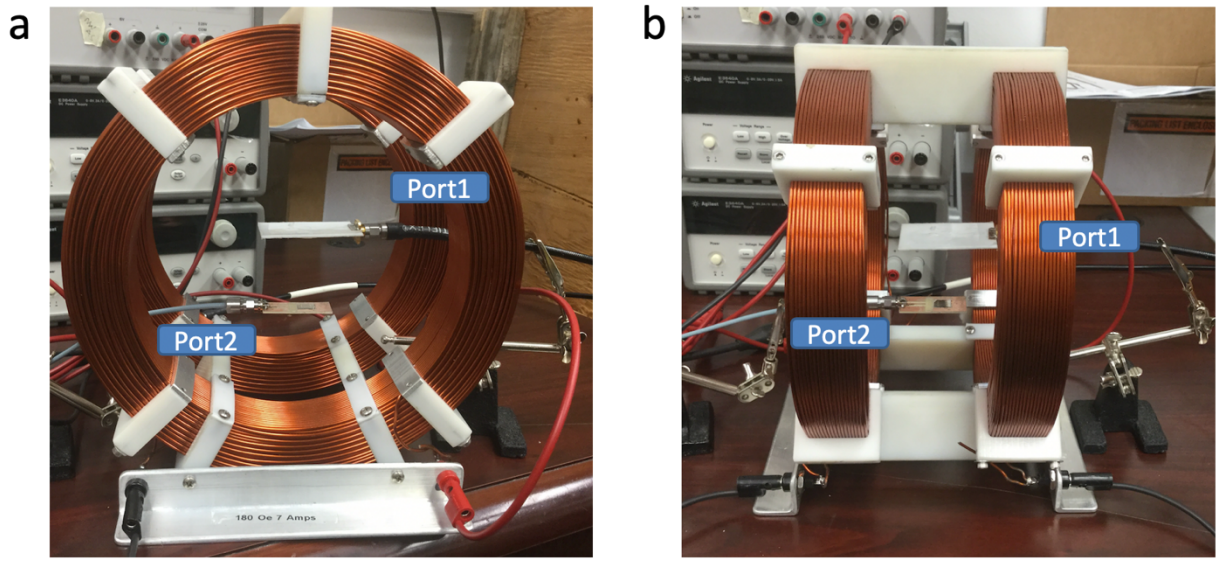

Figure 2-11: (a) Test of the multiferroic shear wave antenna under longitudinal bias field. (b) Test of the multiferroic shear wave antenna under transverse bias field.

After finishing the fabrication of the shear wave antenna, it was assembled with a PCB board. Here, the gold electrode is connected to the transmission line of the PCB board by wire

bonding. At the same time, the ground electrode is connected to the ground electrode of the PCB board by silver epoxy. Then the antenna was connected to the VNA electronics using a SMA connector. Here, a loop antenna was connected to port 1 of the VNA electronics while the multiferroic antenna was connected to port 2 of the VNA electronics. Under this orientation, most of the magnetic field come from the loop antenna is out-of-plane of the multiferroic antenna as well as the magnetic resonators. However, in this test, the multiferroic shear wave antenna is set little off-center from the loop antenna. So, there is also some in-plane components here as shown in Figure 2-10 (c). But, in this test, it is not obvious out which component is dominating. Figure 2-11 shows the orientation of the test. In the figure, the big coils are used for providing a bias field. In Figure 2-11 (a), the coils provide a longitudinal bias field while in Figure 2-11 (b) the orientation of the bias field coil is changed to provide a transverse bias field. For both longitudinal bias field and transverse bias field, the bias field value can be changed from 0 Oersted to 150 Oersted.

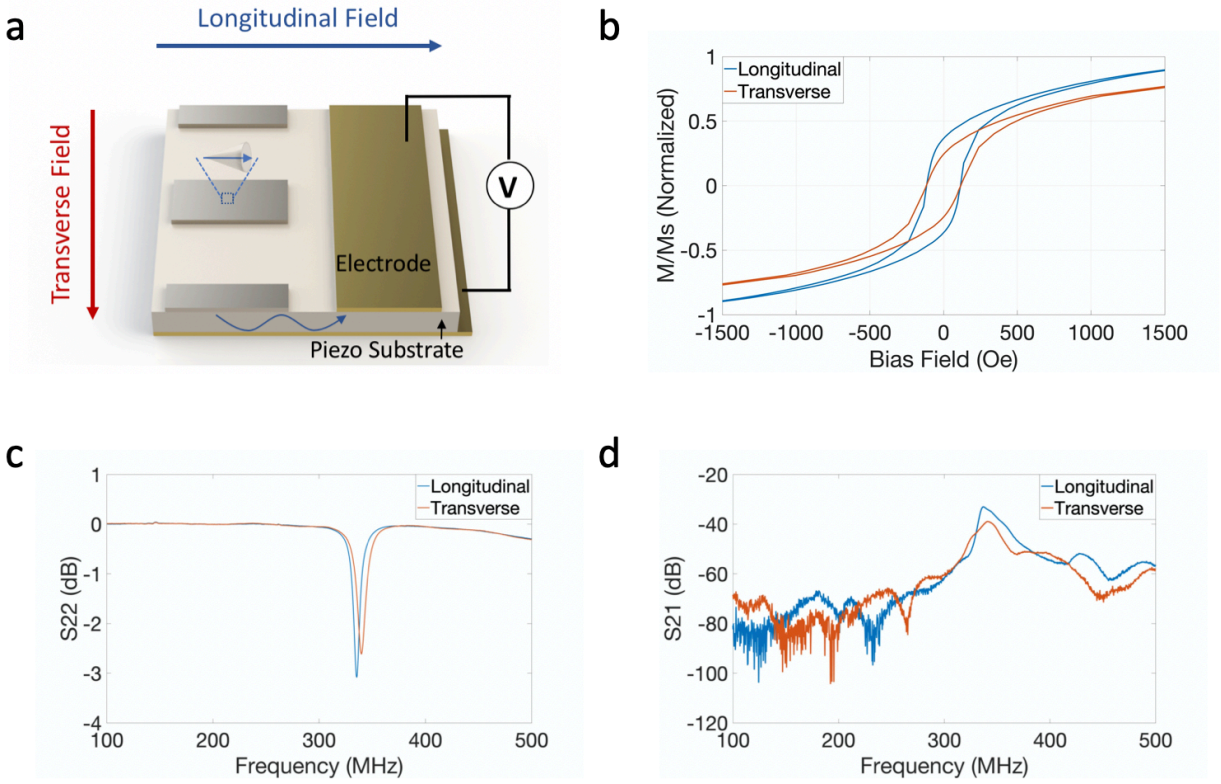

Figure 2-12: Test results of the multiferroic shear wave antenna. (a) Orientation of the longitudinal bias field and transverse bias field under micro scale. (b) M-H curve of the magnetic resonators in both directions. (c) Return loss (S22) of the multiferroic shear wave antenna under different bias field. (d) Receiving coefficient (S21) of the multiferroic shear wave antenna under different bias field.

Several tests under a different bias field are performed for this antenna. Figure 2-12 shows the representative test results of the multiferroic shear wave antenna prototype. Figure 2-12 (a) shows the orientation of the bias fields in the micro scale: the longitudinal bias field is along the long axis of the magnetic resonators while the transverse field is along the short axis of the magnetic resonators. Figure 2-12 (b) shows the M-H curves of the magnetic resonators in both directions. In this plot, the horizontal axis indicates the bias field with the unit of Oersted (Oe), while the vertical axis indicates the normalized magnetization. From this figure, it can clearly tell that the short axis is the hard axis of the magnetic resonators while the long axis is the easy axis of the magnetic resonators. Figure 2-12 (c) shows the return loss (S22) of the multiferroic shear

wave antenna under different bias field. The horizontal axis is the frequency with units of mega-hertz (MHz) while the vertical axis here shows the return loss of the multiferroic shear wave antenna. Because the multiferroic shear wave antenna is connected to port 2 of the VNA electronics, the return loss is labeled as S22. This figure shows that the return loss of the antenna can reach about -3dB at around 330MHz. At the same time, for the longitudinal bias field and transverse bias field, there exists slightly difference. That indicates that the signal is magnetically dependent. Figure 2-12 (d) shows the receiving coefficient (S21) of the multiferroic shear wave antenna under different bias field. The horizontal axis is the frequency with units of mega-hertz (MHz) while the vertical axis here shows the receiving coefficient. Because the detect antenna is connected to the port 1 of the VNA electronics, the receiving coefficient of the multiferroic shear wave antenna is labeled as S21. In this figure, the S21 corresponds to the S22 and has peaks at around 330MHz. Also, just like in the return loss S22, there is a slight difference in S21between the longitudinal bias field and transverse bias field.

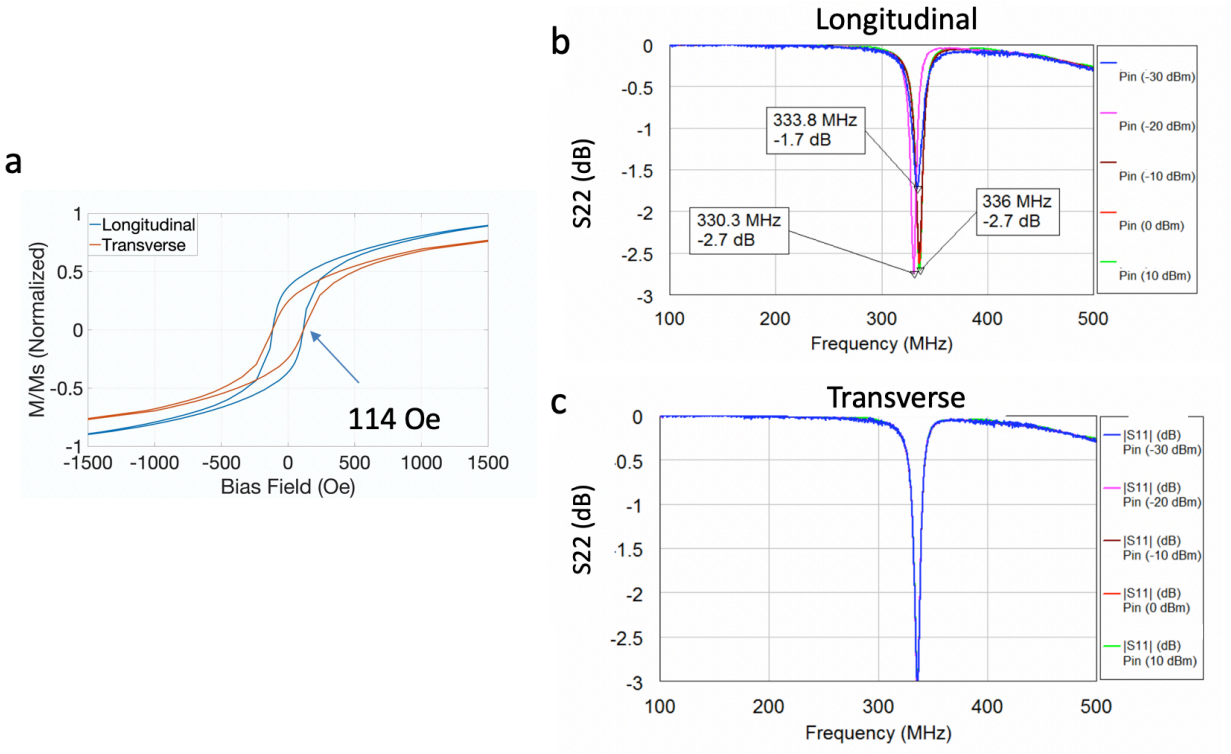

Figure 2-13: (a) M-H curve and coercive field of the magnetic resonators. (b) S22 results under longitudinal bias field with different input power. (c) S22 results under transverse bias field with different input power.

Figure 2-13 shows more evidence that demonstrates the signal is from the magnetic resonators. Under a different bias field, the input power from the VNA electronics is varied and then the return loss (S22 in this test) of the multiferroic antenna is recorded. Figure 2-13 (a) shows the details on the M-H curve as well as the coercive field of the magnetic resonators. The coercive field of both the long axis and short axis of the magnetic resonators is about 114 Oe. Under a 100 Oe bias field, for each bias field orientation, the S22 is tested under different input power from the VNA electronics. Figure 2-13 (b) shows the S22 results under longitudinal bias field (along the easy axis of the magnetic resonators) with different input power. The results show that: under a 100 Oe's longitudinal bias field, the S22 will have big fluctuations. This plot records the S22 with different bias fields under different time. These random fluctuations indicate that: for every

frequency scan, the magnetization in the magnetic resonators will be re-orientated and that cause non-linear phenomena. Figure 2-13 (c) shows the S22 results under a transverse bias field (along the hard axis of the magnetic resonators) with different input power. Under this bias field, there is no fluctuation on the S22 data. The comparison between Figure 2-13 (b) and Figure 2-13 (c) indicates that this fluctuation corresponds to the hard/easy axis of the magnetic resonators. This shows that there is a high chance that part of the S22 response is coming from the magnetic resonators.

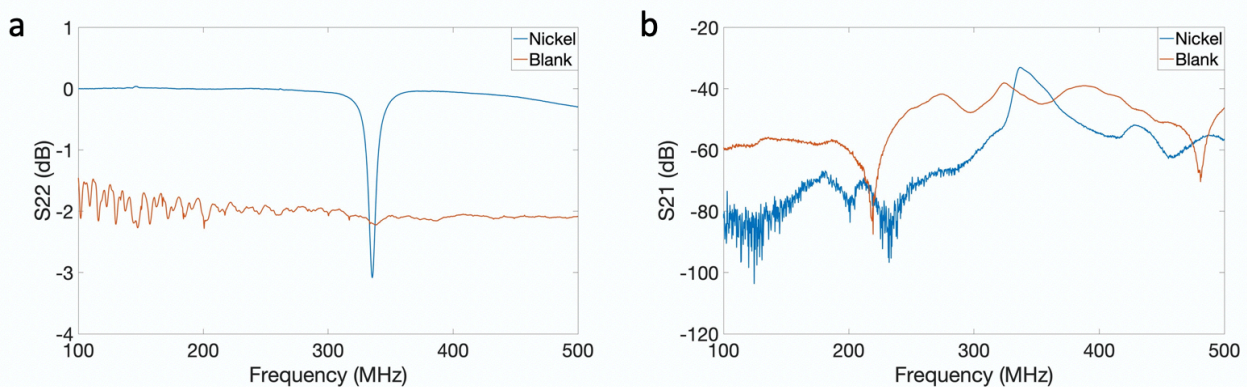

Figure 2-14: Comparison between the sample with Nickel resonators (the "Nickel sample") and without Nickel resonator (only gold electrodes, the "Blank sample"). (a) Return loss (S22) of the Nickel sample and the Blank sample. (b) Receiving coefficient (S21) of the Nickel sample and the Blank sample.

Finally, the sample with the Nickel resonators (the "Nickel sample") and without Nickel resonator (only gold electrodes, the "Blank sample") were compared. Figure 2-14 (a) shows the return loss (S22) for the Ni sample and the Blank sample. Just as Figure 2-12 (c), the horizontal axis is the frequency in mega-hertz (MHz) while the vertical axis shows the return loss for both the Nickel Sample and Blank Sample. In this figure, the blue line indicates the S22 for the Nickel sample while the red line indicates the S22 for the Blank sample. For the Nickel sample, there is clearly a deep peak at around 330MHz, however, for the blank sample, the data are relatively flat

with slightly fluctuations that may be caused by Ohmic losses. Here, the ground electrode is attached to the PCB board through silver epoxy. The different thickness of the silver epoxy may cause the Ohmic losses' difference. That might be the reason why the background noise of the Blank sample is higher than the one for the Nickel sample. Figure 2-14 (b) shows the receiving coefficient (S21) comparison between the Ni sample and the Blank sample. Here the vertical axis shows the receiving coefficient S21. In this figure, just like in the case of the return loss plot, the blue line indicates the S21 for the Nickel sample while the red line indicates the S2 for the Blank sample. We can observe, from the figure, that for Nickel sample there is a peak that corresponds to the same frequency as S22 in Figure 2-14 (a). However, for the Blank sample, there is no obvious peak in the frequency range 100MHz to 500MHz.

2.4 Conclusion

In this chapter, a new multiferroic antenna is introduced: shear wave antenna. The system can easily be assembled into an antenna array to get higher radiation power. The optimization model helped us find the right dimensions for increasing the output power of the antenna at a given frequency. The test results showed a return loss that reaches -3dB. At the same time, the test under different bias indicates that the signal is magnetically dependent. In this work, the cross-arranged electrodes and the resonators decrease the transfer range between electrode and resonators. This makes the making of a high efficiency multiferroic antenna possible. At the same time, the fabrication difficulties of this system are low. The shear wave antenna can easily form an antenna array in order to achieve a higher radiation power and efficiency. However, there is still a probability that the signal is coming from parasitic elements. A better design with higher signal strength is then needed.

3. Lamb Wave Antenna with Energy Reflecting Components

The multiferroic shear wave antenna shows that the cross-arranged electrodes and resonators are effective. However, it is difficult to increase the radiation power even after geometry optimization. The reason for this is that energy dissipates from the sides and bottom of the antenna because of acoustic impedance mismatching. In order to increase the antenna's efficiency as well as the radiation power, new methods for reducing the energy dissipation are needed.

This chapter introduces a new multiferroic antenna: lamb wave antenna with energy reflecting components. Here, the bridge between the EM wave and the RF signal in the circuit is a lamb wave. Here, the lamb wave is formed and transferred in the piezoelectric substrate. When the lamb wave travels to the edge or the bottom of this new antenna it will be reflected back by energy reflecting components such as acoustic Bragg mirror, acoustic gratings or air cavity. Through the use of this technique, most of the mechanical energy in this system can be used for driving the magnetization in the magnetic resonators without dissipation. In this way, the signal strength can be enhanced to useful levels.

3.1 Introduction

The history of Electro-Acoustic technology can be traced back to World War II. Today, the most common Electro-Acoustic technology that is being used for radiofrequency (RF) filters is surface acoustic wave (SAW) and bulk acoustic wave (BAW) technology.[81] For both filter technologies, improving the resonance qualities or Q factor, is a popular research topic.

During the century following the discovery of the surface acoustic wave in 1885[82], there was a significant amount of research on explaining its mechanism.[83] Later in 1969, Tancrell et al built the first interdigital transducer (IDT) using SAW resonators.[84] However, the

unidirectional problem of IDTs limits their efficiency. In order to solve that problem, people placed metal gratings on the sides of the IDT in order to reflect the surface acoustic waves.[81] These metal gratings reflect the surface acoustic wave back and increase the efficiency of the system.

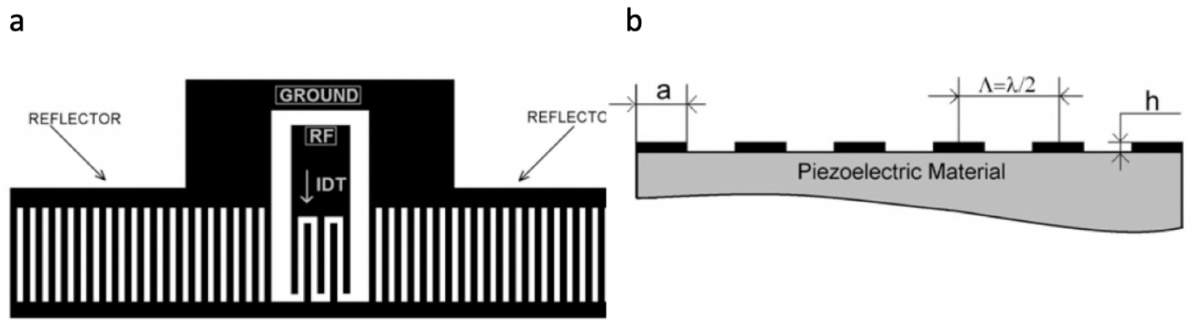

Figure 3-1: (a) IDT structure with side reflectors. (b) Side view of a typical SAW resonator. (Figure from [81])

For bulk acoustic wave, the typical topology is a sandwich structure with one piezoelectric substrate and two electrodes.[84] A representative technology with this topology is Thin Film Bulk Acoustic Resonator (FBAR). These FBAR devices are typical freestanding BAW devices. Due to the big acoustic parameter difference between the interface of solid and air, the acoustic energy is reflected by the interface. In this way, the acoustic energy is trapped in the resonator and increases the Q factor of the system.

Another piece of technology used for reflecting acoustic energy is called solidly mounted resonators (SMR). It was first introduced in 1995.[85] In this system, an acoustic Bragg mirror is underneath the BAW resonator. The acoustic Bragg mirror is comprised of pairs of high/low impedance materials. By increasing the number of these layer pairs, the acoustic Bragg mirror can reflect most of the acoustic energy coming from the BAW resonator. The advantage of SMR is that it avoids the usage of an air cavity, thus increasing the yield in the manufacturing process by

significantly reducing the complexity of the design. SMR also significantly reduces the temperature sensitivity of the resonator.

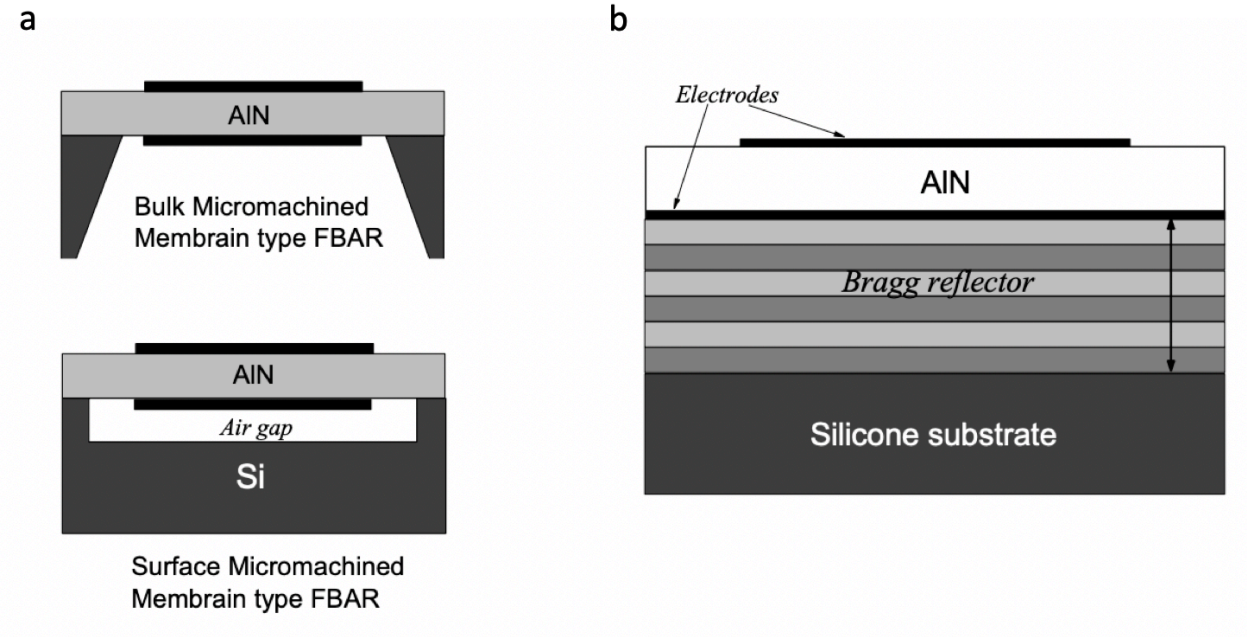

Figure 3-2: (a) Thin Film Bulk Acoustic Resonator (FBAR). (b) Solidly Mounted Resonator (SMR). (Figure from [81])

3.2 Design and Modeling

In order to solve the energy dissipation problem that shear wave antennas confront, the energy reflecting components need to be designed carefully. As shown above there is mature energy reflecting technology on both SAW and BAW resonators. They can be combined for the lamb wave multiferroic antenna. The energy reflecting components form an energy trap for concentrating the mechanical energy within multiferroic antenna. Thus, the design of the lamb wave antenna starts from the design of the energy trap. The energy trap here prevents the acoustic energy from leaking from both the sides and the bottom of the antenna. In this way, most of the acoustic energy can be transferred into strain on the magnetic resonators. Therefore, the energy trap can significantly increase the efficiency of the multiferroic antenna.

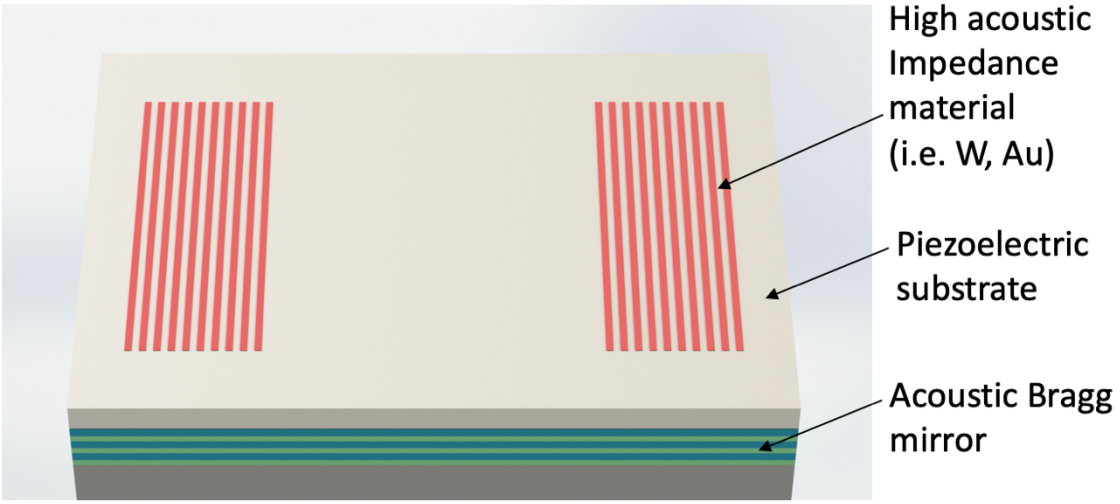

Figure 3-3: Energy trap formed by acoustic gratings and acoustic Bragg mirror.

The energy trap used here is comprised of two parts: the acoustic gratings and the acoustic Bragg mirror. The acoustic gratings are formed by high acoustic impedance material, for example, tungsten (W) and molybdenum (Mo). Unlike in SAW resonators, where the width of the acoustic gratings is usually $\frac{\lambda}{2}$the width of the acoustic gratings is designed to be $\frac{\lambda}{4}$, where λ is the mechanical wavelength in the piezoelectric substrate for certain frequency.

The acoustic Bragg mirror is a set of multilayer materials. For example, W/SiO_2 pairs and Mo/Al pairs. For each layer, the thickness is determined by $\frac{\lambda}{2}$, where λ is the mechanical wavelength in each layer. However, in this lamb wave multiferroic antenna, there exists two types of mechanical waves propagating simultaneously: a shear wave and longitudinal wave. Seeing as the wavelength is different for both waves two kinds of acoustic Bragg mirror are needed and require a proper design to increase their reflecting efficiency.[86]

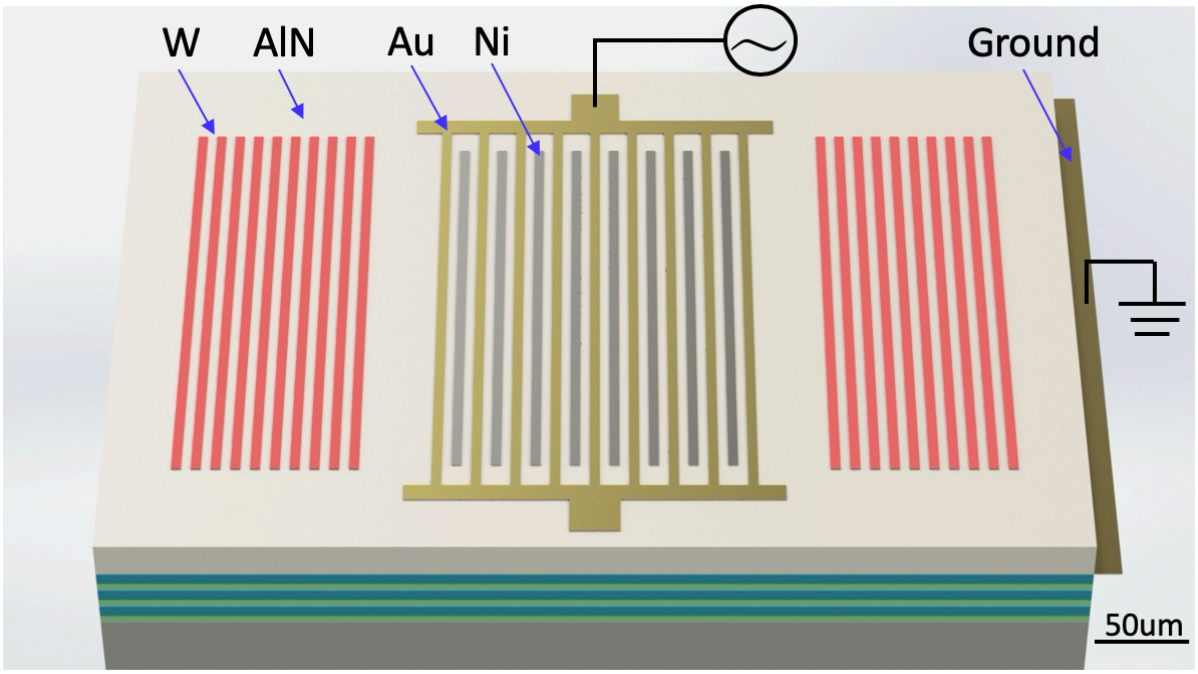

Figure 3-4: Lamb wave multiferroic antenna with energy reflectors.

The design of the Lamb wave multiferroic antenna with energy reflectors is based on a shear wave antenna and its energy trap. As shown in Figure 3-4, the multiferroic antenna is in the center of the energy trap. In this design, the acoustic gratings are made by W, the electrodes are made by Au, the magnetic resonators are made by Au while the piezoelectric substrate is 1um thick Aluminum Nitride (AlN). Here, both the multiferroic antenna and the acoustic gratings lay on the top of the AlN substrate. The global ground electrode is underneath the AlN substrate. Below the ground electrode, there is a set of acoustic Bragg mirrors that are comprised of high/low impedance multilayers. In this design, unlike in the shear wave antenna design, the shape of the Ni magnetic resonator is changed from rectangular to long stripe. This was done to ensure the waves are created and transferred along one direction and then be reflected back by the acoustic gratings.

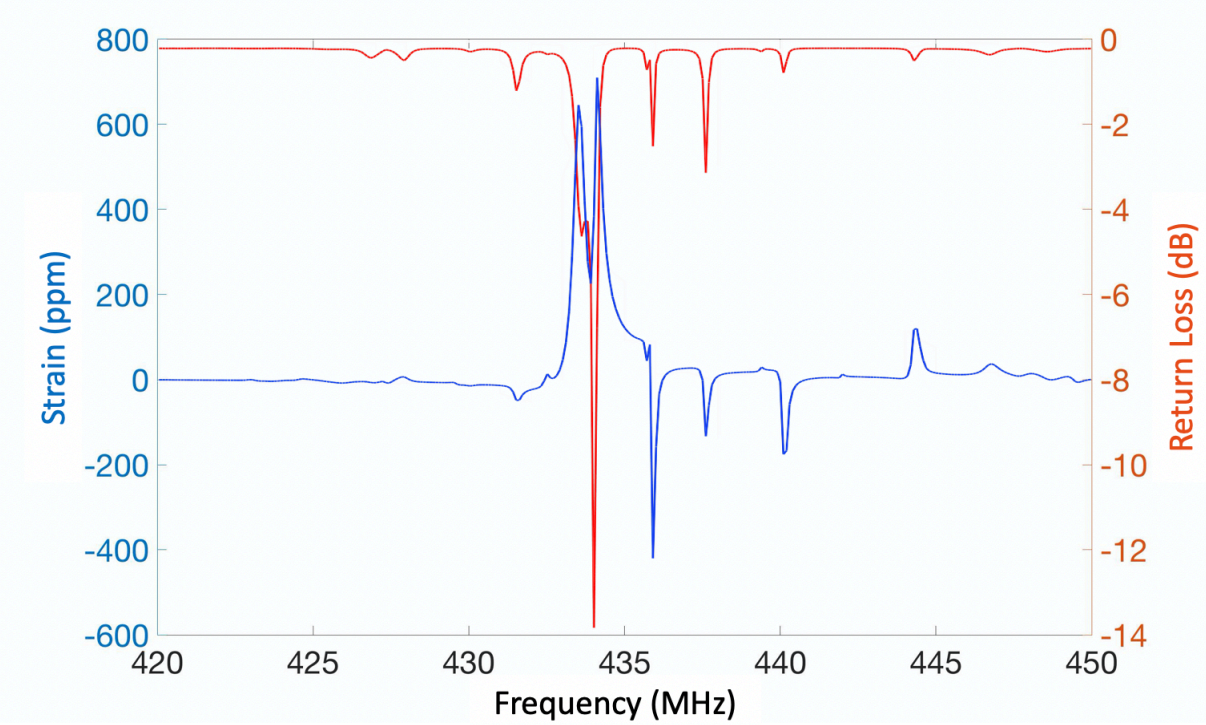

Figure 3-5: Simulation results on the lamb wave multiferroic antenna.

A 2-dimension finite element model is used here for predicting the performance of the antenna. The results are shown in Figure 3-5. Here, the acoustic Bragg mirror is made by W/SiO_2 multilayers. The thickness of the acoustic Bragg mirror from top to bottom are shown in Table 3-1. The design parameters of the antenna that get from optimization model are shown in Table 3-2.

Table 3-1: The thickness of the acoustic W/SiO_2 Bragg mirror from top to bottom.

Thickness	**Value**
SiO_2 for shear wave	2um
W for shear wave	1.5um
SiO_2 for shear wave	2um
W for shear wave	1.5um
SiO_2 for longitudinal wave	3.5um

W for longitudinal wave	3um
SiO_2 for longitudinal wave	3.5um
W for longitudinal wave	3um

Table 3-2: The design parameters of the antenna.

Design Parameter	Value
Width of the resonator	6.224um
Width of the electrode	6.224um
Width of the grating	6.224um
Thickness of the resonator	492nm
Thickness of the electrode	70nm
Thickness of the grating	352nm

Using these parameters, a finite element model was performed in frequency domain. The horizontal axis in Figure 3-5 is the frequency. The vertical axis on the left indicates the strain on the Ni magnetic resonator while the vertical axis on the right indicates the global return loss S11. With the parameters specified in Table 3-1 and Table 3-2, the return loss can reach near a value of -14 dB at around 435MHz. At the same time, the strain that can be transferred to the representative Ni magnetic resonator can reach 700ppm under 0.1 Watt's input (20dBm).

3.3 Fabrication and Test

The fabrication process begins with the acoustic Bragg mirror. In order to reduce the fabrication difficulties, for the real fabrication, Mo/Al multilayers are used to build the acoustic

Bragg mirror. The parameters detail for the thickness of each layer from top to bottom are shown in Table 3-3.

Table 3-3: The thickness of the Mo/Al acoustic Bragg mirror from top to bottom.

Thickness	Value
Al for shear wave	0.9um
Mo for shear wave	1um
Al for shear wave	0.9um
Mo for shear wave	1um
Al for longitudinal wave	1.8um
Mo for longitudinal wave	2um
Al for longitudinal wave	1.8um
Mo for longitudinal wave	2um
Ti adhesion layer	0.1um

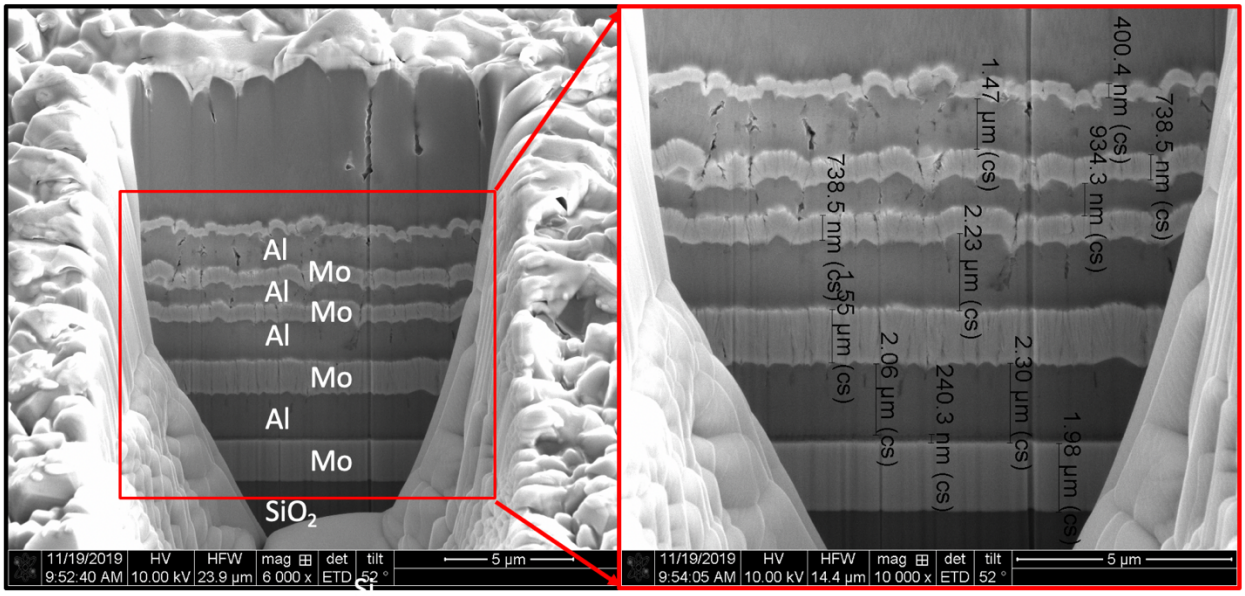

Figure 3-6: Acoustic Bragg mirror fabrication. FIB-SEM picture.

The Bragg mirror fabrication was completed in UCLA's nanolab. The multilayers were deposited by magnetron sputtering. A 6inch Silicon wafer with 2um thermal oxide layer was used here for better adhesion. After fabrication, focused ion beam/scanning electron microscopy (FIB-SEM) was used to characterize the quality of each layer. Figure 3-6 is the picture of the sample's side view under FIB-SEM. In this picture, the white layers indicate a Mo layer while the dark layers indicate the Al layers. The first several layers are good and flat, however, but after depositing several layers, the layer become wrinkled. Although the thickness of every layer is close to design parameter the wrinkled structure will distort the acoustic wave propagation path. Numerous difficulties were experienced attempting to solve this problem.

In order to solve this problem, a compromise on the fabrication was made. An air cavity like the FBAR device is used here to perform as the acoustic Bragg mirror and reflect the energy. In this process, after depositing the antenna structure with photolithography, the AlN substrate is etched with Chlorine gas. The etch time should be controlled carefully to make sure the Chlorine

gas can etch through the AlN substrate without etching all the photoresist. Here the etching time used was 4minutes + 4 minutes + 3 minutes. The gap between every etch step is for the system to cool down. If the photoresist (KMPR1005) is heated too much, it becomes difficult to remove.

After getting the etching holes, the wafer was put in the XeF_2 atmosphere for eating the silicon substrate. The XeF_2 atmosphere will etch the Silicon substrate isotopically and create an air cavity underneath the antenna as shown below.

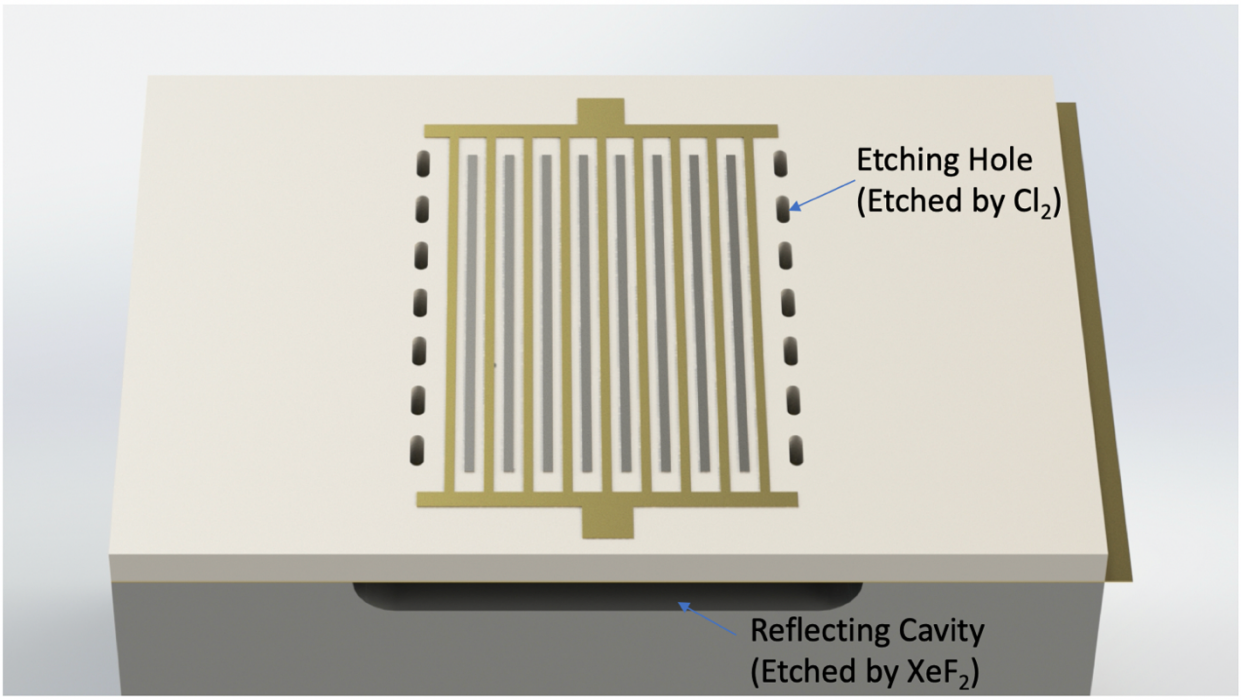

Figure 3-7: Real fabrication of the lamb wave multiferroic antenna.

Figure 3-7 shows the sketch of a real fabricated lamb wave multiferroic antenna. As can be seen here, the etching holes themselves perform as the metal gratings. They can reflect the wave that propagates in the horizontal direction. At the same time, the air cavity underneath the antenna performs as the acoustic Bragg mirror. The interface between the air and the solid can reflect the acoustic wave and then confine the acoustic energy in the resonator.

In order to increase the fabrication yield of the antenna array during the finalized fabrication procedure, the time that the antenna chip exposed in the XeF_2 atmosphere was carefully controlled. It is important to note that after etching the air cavity is not completely released. There is still some residual Silicon underneath the lamb wave antenna to provide more structural support. At last, a 2-dimension finite element model was used to simulate the system. The design parameters are shown in the Table 3-4.

Table 3-4: The design parameters of the real-fabricated antenna.

Design Parameter	Value
Width of the resonator	3.75um
Width of the electrode	3.75um
Thickness of the resonator	200nm
Thickness of the electrode	100nm

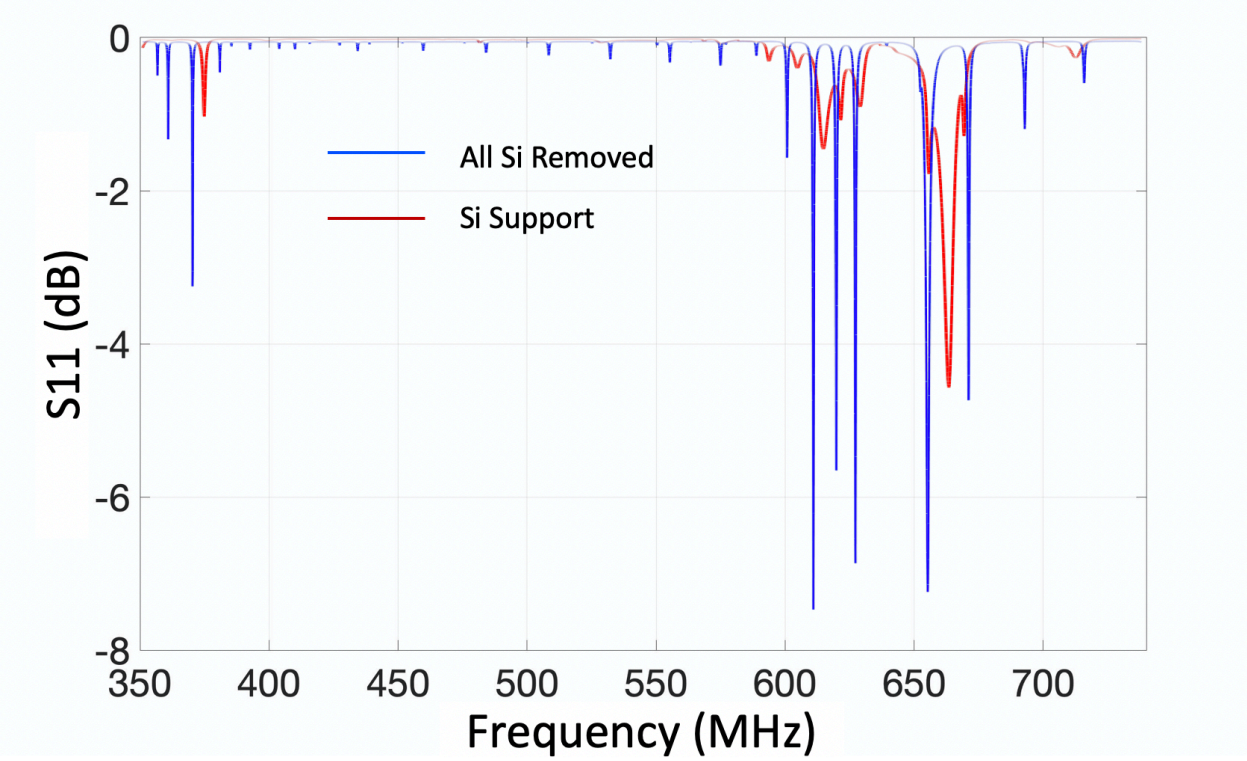

Figure 3-8: Simulation results on the real fabricated antenna with etching holes and air cavity.

Figure 3-8 shows the simulation results for the lamb wave multiferroic antenna with etching holes and air cavities included. In this figure, two devices are modeled. One is the device with all the silicon removed, and another is for the one with extra silicon support. The horizontal axis here is the frequency while the vertical axis here shows the return loss. Both of the devices are modeled according to the real length of the fabrication: 1mm. The blue line indicates the return loss of the device that all silicon substrate underneath the antenna be removed. At the same time, the red line here indicates the return loss of the device that has extra silicon support underneath the antenna. There are two main peak groups between 350MHz to 740MHz. From this plot, a phenomenon can be seen, the extra silicon support does not affect the frequency of the antenna significantly. However, it will make the antenna more lossy. This makes sense because some of

the acoustic energy will dissipate from the silicon base, instead of being confined with in the resonator.

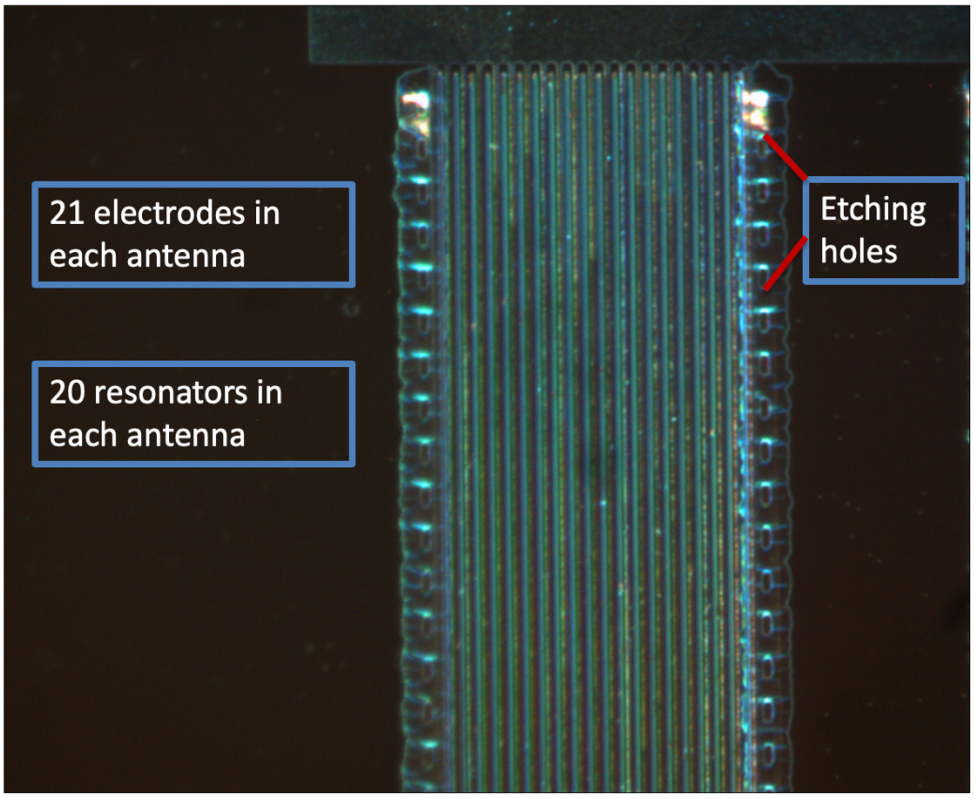

Figure 3-9: Picture of the antenna under microscope.

Figure 3-9 shows the lamb wave antenna under a microscope. In this antenna, there are 21 electrodes and 20 resonators are patterned on the top of AlN substrate. The thickness of the Au electrodes is 100nm while the thickness of the Ni resonators is 200nm. Here, the Ni resonators lay between the Au electrodes just like the 3-D sketch shows. All the electrodes are connected together by a bus electrode. On every bus electrode, there are 14 antennas like this. in this figure, the etching holes are on the side of the antenna and are next to the Au electrodes. In this way, the acoustic wave that propagate along the horizontal direction will be reflected better than if the etching holes were next to the Ni resonator according to the 2-D finite element model. However, this design, it

cannot provide nearly as much strain as the acoustic Bragg mirror design. The reason may because for the acoustic Bragg mirror design, the gratings can reflect the acoustic energy back to the acoustic Bragg mirror and then participate the following energy transformation. But for this design, the etching holes cannot reflect the energy from the side perfectly.

For the real device fabrication, using the same fabrication process, two different samples are fabricated. The only difference between them was that: for one sample, the resonators were made by magnetoelastic material Ni. It is been called “Nickel sample”. While for the other one, the resonators’ material was changed into nonmagnetic Au. Because of that, it is been called “Gold sample”. These gold samples were used as a control to determine the role and the effect of the magnetoelastic material in this design.

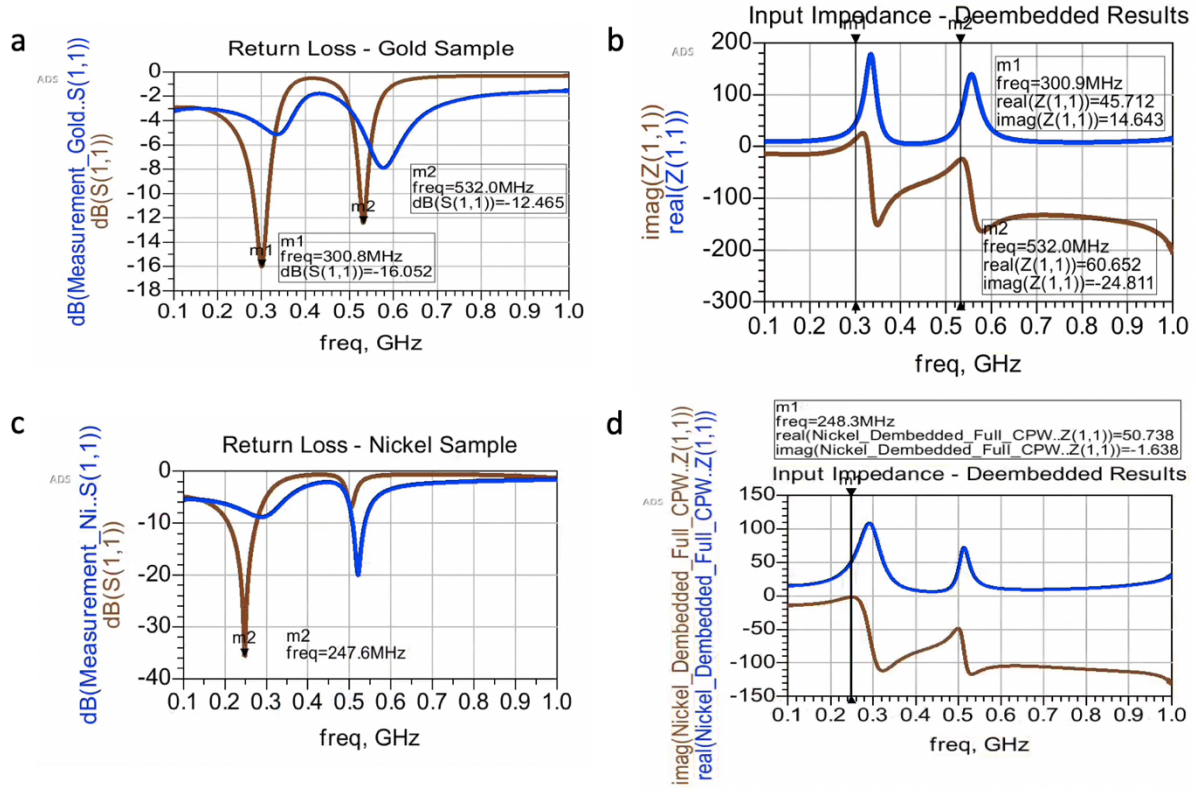

Figure 3-10: (a) Return loss of Gold sample. (b) Impedance of Gold sample. (c) Return loss of Nickel sample. (d) Impedance of Nickel sample.

In a test similar to those conducted with shear wave antennas, the lamb wave antenna was attached onto a PCB board. The antenna's detect electrode was attached to the transmission line of the PCB board with wire bonding. All the tests were conducted using port 1 of the VNA electronics.

Figure 3-10 shows the test results about the antenna as well as the Au reference sample. The blue lines show the test results with both the PCB board and the lamb wave antenna. For the return loss plots, the red lines show the test results that de-embedded the PCB board as well as the bonding wires with mathematical method. For the impedance plots, the red lines depict the imaginary part of the impedance while the blue lines depict the real part of the impedance of the antenna. For the impedance, all results eliminate the influence of the PCB board and the bonding wires with mathematical method.

Figure 3-10 (a) shows the return loss (S11) of the gold sample. Here two peaks can be observed. One is around 300MHz while another is around 532MHz if the influence of the PCB board and the bonding wires is eliminated. There is a bit of a shift from the model prediction. However, there are still two resonance peaks as the finite element model predicts. At the same time, because the bonding wires provide extra inductance in the system, the frequency will shift higher than the de-embedded one. Figure 3-10 (b) shows the impedance of the gold sample. The shape of the imaginary part of the impedance highly indicates that the two resonant peaks arise from the piezoelectric resonance of the substrate. The imaginary part of the impedance does not cross 0 axis, the reason for this may be the impact of the bus's electrical parameters in the antenna array.

Figure 3-10 (c) shows the return loss (S11) of the nickel sample. For the nickel sample, there are also two peaks. One is around 247MHz while another one is around 500MHz. The resonance frequencies are slightly different from the gold sample. This makes sense because of the different Young's moduli as well as the different material densities. Figure 3-10 (d) shows the impedance of the nickel sample. Again, the shape of the imaginary part of the impedance strongly indicates that the two resonant peaks are because of piezoelectric resonance. These test show that the system is indeed resonating and transferring some energy to the resonators.

3.4 Conclusion

In this section, in order to solve the energy dissipation problem, a lamb wave multiferroic antenna with energy reflectors is introduces. From the theoretical study, If the acoustic Bragg mirror as well as the acoustic gratings are used as the energy reflector, the strain on the represent Nickel resonator can reach about 700 ppm under -20dBm's input power. Limited by the fabrication difficulties of the acoustic Bragg mirror, air cavity and etching holes are used as a compromise of this design. The test results indicate that in this system, the antenna have mechanical resonance. In this case, the input power can be transferred the strain to the magnetoelastic resonators. The high return loss (about -36dB) shows the great potential of this system to be a practical multiferroic antenna array.

4. Broadband Multiferroic Antenna

4.1 Introduction

Both the shear wave antenna as well as the lamb wave antenna shows a potential to form a multiferroic antenna array. However, both of them are working around their natural frequency. That means, once the device is fabricated, the antenna's frequency cannot be changed. In order to solve this problem, a strain-mediated nanomagnetic oscillator is designed and theoretically studied. The phased-voltage-controlled nanomagnetic oscillators can form an array and radiate together in phase to radiate EM wave.

Nanomagnetic oscillators have been used for many applications such as nanoscale RF signal generators[87]–[89], microwave-assisted recording, nanoscale magnetic field sensors, and neuromorphic computing hardware. In a conventional nanomagnetic oscillator, steady magnetic oscillation is achieved when the current-induced spin torque cancels the Gilbert damping.[90]–[96] However, current-driven magnetic oscillations are power-consuming at the nanoscale due to ohmic losses. In contrast, voltage-driven magnetic oscillation is a more energy efficient control scheme.

In this chapter, a voltage-driven magnetic oscillator is designed. In this system, a cylindrical, magnetoelastic, single domain disk placed atop a piezoelectric substrate. The nano-magnetic-disk is surrounded by three individual electrodes with different AC voltage. Under this input, the magnetization in the magnetic disk can rotate continuously. The spinning single domain magnetization state can radiate electromagnetic energy into free space. Because in this system, the output frequency is depended on the input frequency, the antenna can work over broadband frequencies, from very-high frequency (VHF) to ultra-high frequency (UHF).

4.2 Design and Model Set-up

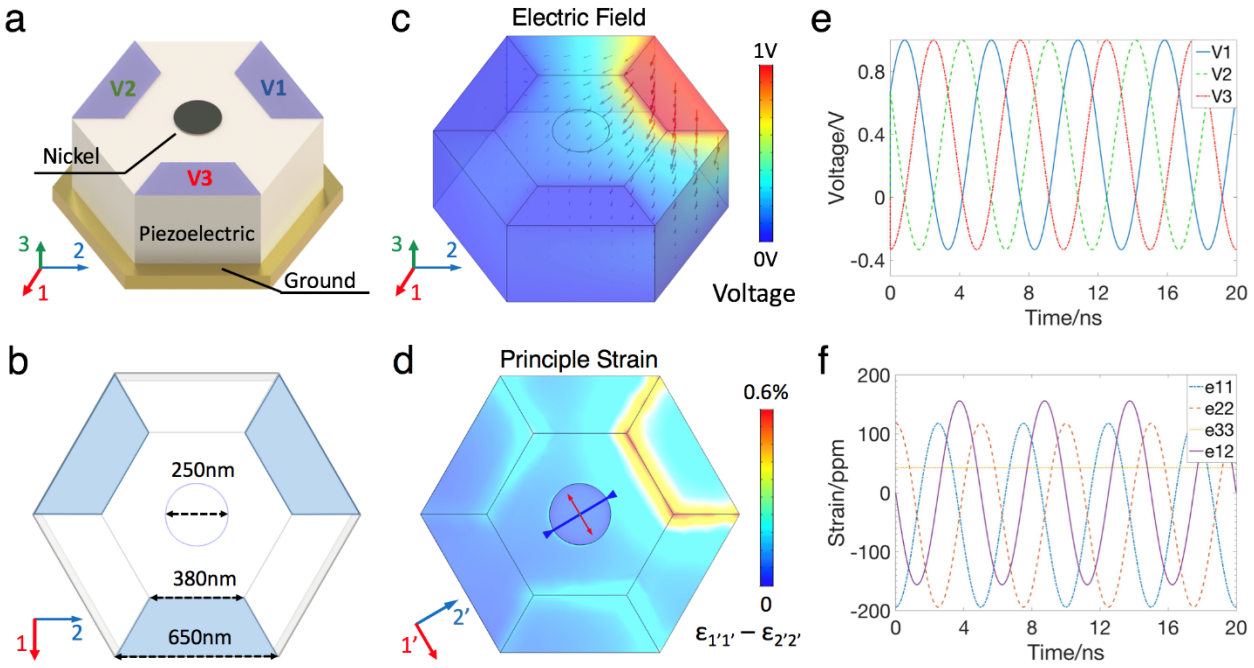

Figure 4-1: New design for multiferroics powered antenna.

Figure 4-1 (a) and (b) schematically show a single element of the antenna arrays. A circular amorphous polycrystalline Nickel layer (250nm×250nm×10nm) was positioned between three trapezoidal Ti/Au electrodes. The nanomagnet and the electrodes are patterned on the top of a hexagon-shaped 500nm thick piezoelectric thin film transducer (PZT-5H), which is pre-poled along the –3 direction. The sidewalls are limited by roller boundary conditions, which restrict the displacement in x-y plane. The bottom global Pt electrode is electrically grounded and is attached to a 2000nm thick silicon substrate (not show in the figure). The boundary conditions are provided in the Methods section and are chosen to reflect a real fabricated device.

In the model, a dynamic voltage is applied to the trapezoidal electrodes. Based on finite element model, and Figure 4-1 (c) and (d) shows the electrical field when 1 V is applied to only the right-top electrode at t = 0.84 ns. The red arrows in Figure 4-1 (c) indicate the applied voltage

generates electric fields. In this case, the electrical field mainly goes from top to grounded bottom, induces in-plane strain not only between the top and bottom electrodes, but also from one top electrode to another. That means that the current design must ensure that no electrical break down occurs through the thickness and in-plane directions (i.e., narrowest point between top electrodes). Here, between the two electrodes, the maximum electric field is 2.6 MV/m which is significantly lower than the breakdown voltage of PZT.[97] In Figure 4-1 (d), the red bar indicates the tensile strain while the blue bar indicates the compressive strain. In Nickel, which has negative magnetoelastic coupling coefficients, the magnetization will tend to align along the compressive strain principal axis.[98] Therefore, by causing the compressive strain to rotate circularly, the magnetization can rotate continuously and form magnetic current which generates EM wave radiation. The uniform voltage-induced strain field, as shown in Figure 4-1 (d), reduces incoherency in the magnetization rotation resulting in magnetic current that produces stable radiation.

Figure 4-1 (e) shows the applied voltage with V1, V2 and V3 corresponding to the three electrodes shown Figure 4-1 (a). The input signals are sinusoidal at 200 MHz with a DC bias of 0.3 V. The signal amplitude is 1.4 V resulting in a maximum applied voltage of 1 V (2MV/m) and minimum of -0.4 V (-0.6MV/m). The specific waveforms were chosen because this wave is easy to get and have high efficiency. Figure 4-1 (f) shows the idle voltage dynamic induced strain through piezoelectric material. The strain is calculated with the fully coupled model and input directly to the single/macro spin model as described in the Modeling and Methods sections. The magnetoelastic strains are negligible compared to the voltage-induced strains are not shown in the plot. This plot indicates that with voltage phase rotating, the principle strain is rotating counterclockwise in this system.

4.3 Results and Limitation of the Broadband Multiferroic Antenna

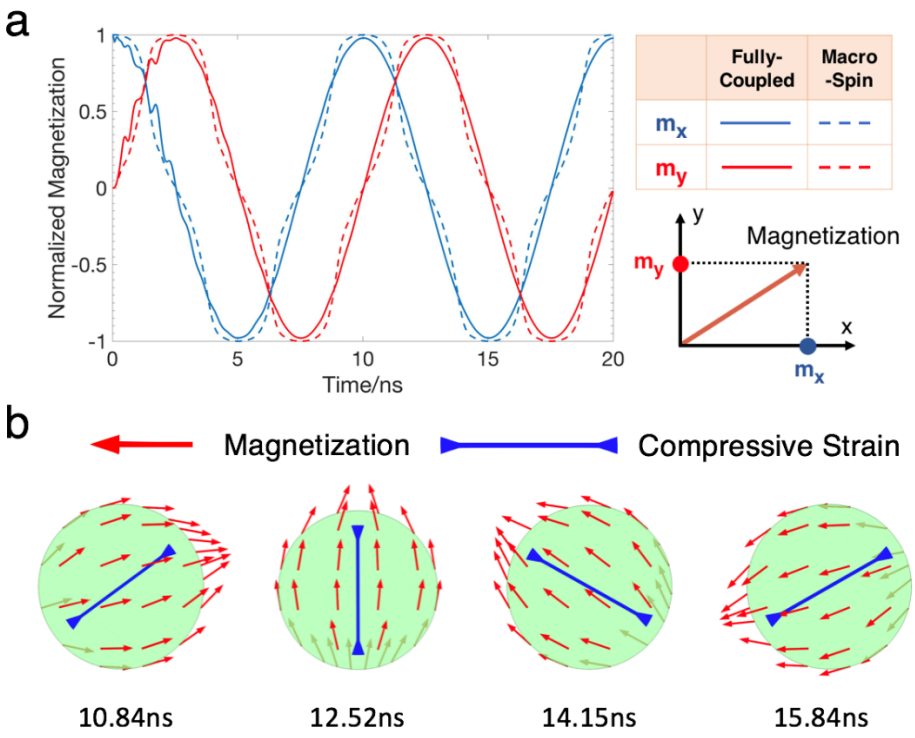

Figure 4-2: Numerical output for multiferroics powered antenna.

Figure 4-2 (a) shows how the magnetization of the single domain Ni element changes over time in response to 200 MHz voltages applied successively to the three electrodes. The magnetization is initialized along the x-axis, so that mx = 1 and my = 0 at t = 0ns. When the strain is first applied, the magnetization does not rotate smoothly as indicated by the fluctuations shown in Figure 4-2 (a) for t < 4 ns. These fluctuations are caused by the inertial response of the spins and not due to strain propagation speed since a uniform strain state is achieved within 0.05 ns (based on the sound of speed, 4500m/s in Nickel). Because neglecting the exchange energy between spins, results from single/macro spin do not have fluctuations and are always faster than results from fully coupled model. Further, this difference of the results show, under this dimension Nickel can only form meta single domains and requires uniform strain to rotate smoothly. Incoherent spins in magnetic dots not only cause the fluctuations of the magnetic waves at first,

but also cause loss of magnetic current. That's the key reason why wide electrodes are required to produce uniform strain.

Figure 4-2 (b), shows the Ni element's magnetization at four distinct times as it rotates in response to the applied voltages. The time is chosen after the system is totally stable and in half of the magnetization's cycle. The plots show a parametric-pumping-like phenomenon because the input strain (blue bar) is rotating with a frequency of 200 MHz while the magnetization (red arrows) rotates at 100 MHz. However, the cause of this frequency difference is different from parametric pumping, since the excitation here provides surplus energy to the system. The compressive strain is symmetric, but the magnetization is not. After compressive strain rotates a complete cycle (ω), the magnetization only goes half (ω/2). This phenomenon can be called as symmetry-pumping. This phenomenon will exist when electrodes are used to pump the magnetization rotation. Also, this phenomenon will help us separate the signal from magnetic dots and nanowires, so that it can raise the signal/noise ratio of the antenna.

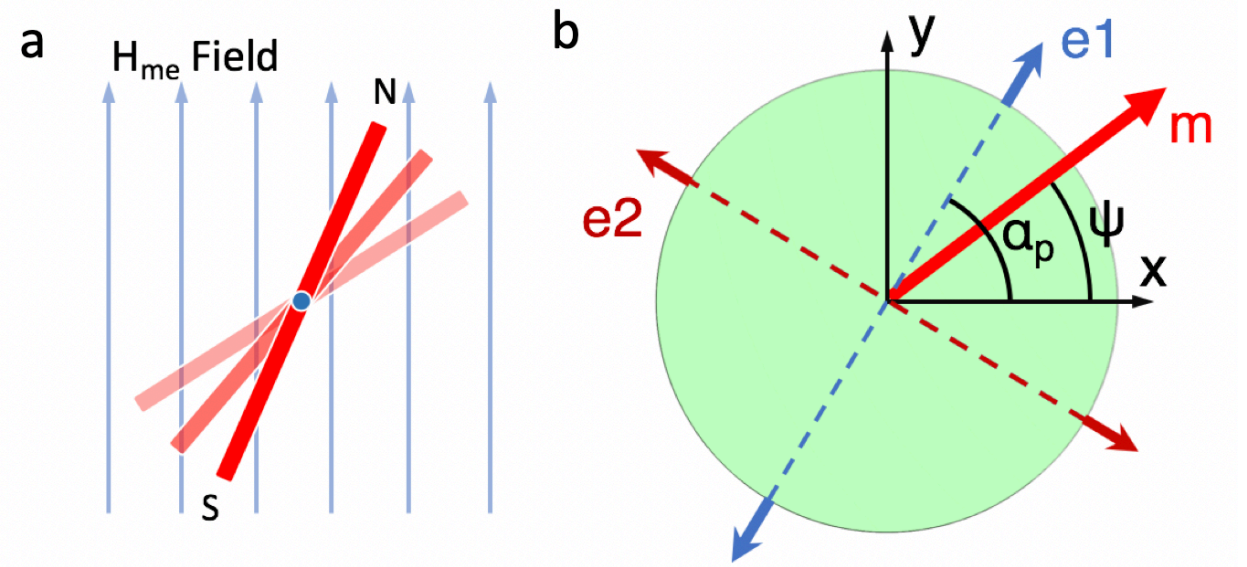

Figure 4-3: (a) Magnetization in the effective filed. (b) Relationship between the magnetization and the principle strains.

However, there is a frequency limitation of the system. Because of the existing of Gilbert damping, there will always be a lag angle between the magnetization and the principle strain. Figure 4-3 (a) shows the mechanism on how the magnetization rotate under the strain that produced by the electrodes. The strain can be transferred into the effective field by these equations:

$$H_1 = -\frac{2}{\mu_0 M_s}(B_1 m_1 e_{11} + B_2 m_2 e_{12}) \quad \text{Eq.4-1}$$

$$H_2 = -\frac{2}{\mu_0 M_s}(B_1 m_2 e_{22} + B_2 m_1 e_{12}) \quad \text{Eq.4-2}$$

where H_1 and H_2 are the effective fields on 1 and 2 direction. m_1 and m_2 are the magnetization's components on 1 and 2 direction. B_1 and $B_2$are first and second order magnetoelastic coupling coefficients. e_{ij} is the strain tensor.

Figure 4-3 (b) shows the relationship between the principle strains and the magnetization. e_1 and e_2 show the principle strains on the magnetic disk. In order to solve the continuous rotating problem, we assume the magnetization's components on 1 and 2 direction as:

$$m_1 = cos\ (\omega_0 t) \quad \text{Eq.4-3}$$

$$m_2 = sin(\omega_0 t) \quad \text{Eq.4-4}$$

After plugging Eq. 4-1~Eq.4-4 to Landau-Lifshitz-Gilbert (LLG) equation (Eq. 1-7), we can get the final equation about the frequency limitation:

$$\omega = -\frac{\gamma e_b}{2\alpha M_s} B_1 (sin2\delta) \quad \text{Eq.4-5}$$

where $e_b = e_1 - e_2$, δ is the angle difference between principle strain and the magnetization. In other words, $\delta = \alpha_p - \psi$.[18] At the same time, $B_1 = \frac{3E\lambda_s}{2(1+\nu)}$, where B_1 is the magnetoelastic coupling coefficients. From this equation, we can tell that the maximum value of $sin2\delta$ is 1. That

means the angle frequency ω has a limitation: $-\frac{\gamma e_b}{2\alpha M_s} B_1$, which is related to the strain on the magnetic disk as well as the material parameters.

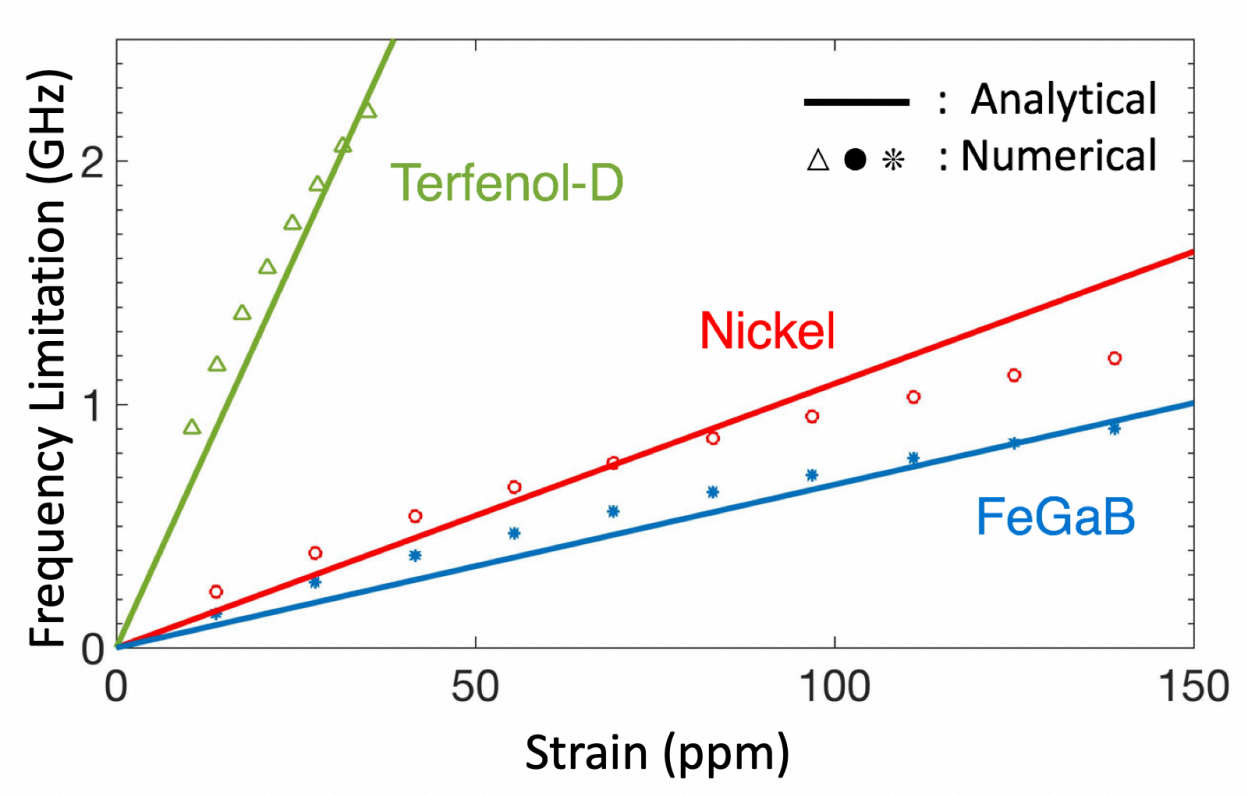

Figure 4-4: Frequency limitation for the magnetization rotating in the disk.

Figure 4-4 shows the frequency limitation of the system. Here, three different magnetic materials are studied: Ni, Terfenol-D and FeGaB. In this figure, the horizontal axis is the maximum value of the strain on the magnetic disk while the vertical axis is the frequency limitation of the system. The analytical results, which are obtained from Eq. 4-5, and the numerical results, which are obtained from macro-spin model framework, show a match between each other. However, under very high strain, the system is still limited by ferromagnetic resonance (FMR) and cannot be un-limited as the analytical results indicate.

The limitations for different material nanodisks are also different due to the material parameters. Here, the limitations for Nickel, Terfenol-D as well as FeGaB are studied. The key parameters are shown in Table 4-1[66], [99], [100]:

Table 4-1: Key parameters for different material.

Parameter	Description	Units	Nickel	Terfenol-D	FeGaB
$\boldsymbol{\lambda_s}$	Saturation Magnetization	A/m	4.8×10^5	8×10^5	978
$\boldsymbol{B_1}$	Magnetoelastic Coupling Coefficient	N/m^2	7.06×10^6	-1.11×10^8	-4.23×10^6

Finally, if the system is patterned as an array on a 2cm*2cm PZT substrate, the radiation power can be obtained from the equation:

$$\langle P \rangle = \frac{Z_0 k^4}{12\pi} |\mathbf{m}_F|^2 = \frac{\mu_0 \omega^4}{12\pi c^3} |\mathbf{m}_F|^2 \qquad \text{Eq.4-6}$$

Table 4-2: Predicted Radiation Power.

Frequency	Terfenol-D (dBm)	Nickel (dBm)	FeGaB (dBm)
10MHz	-116.1	-120.5	-114.3
100MHz	-76.1	-80.5	-74.3
500MHz	-48.1	-52.6	-46.4
1GHz	-36.1	-40.5	-34.3
2GHz	-24.0	-28.5	-22.3

This radiation power number is estimated. In Table 4-2, the red number means that this magnetic material cannot really reach such high frequency as well as the radiation power. Here, the radiation power is related to the frequency: higher frequency results in higher radiation power. However, for these three magnetic materials, the system shows an ability to radiate EM wave within a wide frequency range.

4.4 Conclusion

In this chapter, a broadband multiferroic antenna with tunable frequency is introduced. Here, phase-controlled AC voltage input is applied to the system. The input on individual electrode can provide continuously rotating strain to the magnetic disk. Because there is always a relationship: after compressive strain rotates a complete cycle (ω), the magnetization only goes half (ω/2). The frequency of the magnetization's rotation can be tuned by tuning the input strain's frequency, i.e. the frequency of the AC voltage that been applied on the electrodes. For different magnetic material: Ni, Terfenol-D and FeGaB, the system shows similar performance: that there is a frequency limitation. The analytical results and the numerical results show similar phenomenon, which gives us a path to find the best magnetic material for getting higher radiation power for this antenna.

Part II

Other Multiferroic Devices

5. Multiferroic Nano Logics

5.1 Introduction

Consumer electronics are responsible for approximately 18% of all US home energy consumption, a number predicted to increase in upcoming years.[101] With the increasing proliferation of always-on electronic devices like cell phones and computers, the energy efficiency of traditional CMOS (Complementary Metal Oxide Semiconductor) devices needs to be scrutinized and improved. In the early 2000's CMOS efficiency began rapidly decreasing due to leakage currents in transistors as the devices became smaller. Standby power is now comparable to the actual dynamic operating power in transistors.[102] While memory elements are commonly designed with 40kbT (~0.16 aJ) energy barriers to protect against thermal fluctuations, discharging a single transistor (i.e., flipping a single bit) dissipates around 450aJ.[103] Therefore, nearly 3000 times more energy is dissipated to flip a CMOS bit of information than the energy barrier actually requires (0.03% efficient). Nanomagnetic logic (NML) is proposed as a route to more energy efficient, non-volatile, memory and logic devices. These devices consume drastically less power to flip a bit of information and dissipate zero standby power.

NML evolved from Bennett's early work using quantum cellular automata (QCA) to store and process information.[104] Magnetic quantum cellular automata (MQCA) use magnetization as the information carrier, in contrast to electrostatic QCA devices that rely on charge transport. MQCA has been demonstrated as a viable room temperature technology, while electrostatic QCA devices tend to require cryogenic temperatures for operation.[105] NML is the modern term used to describe the use of MQCA systems,[106],[107] and it is the topic of this chapter. Figure 5-1 shows a typical manifestation of NML using ellipsoidal single domain nanomagnets that are

coupled via dipolar interactions (as described in Bennett's original work[104]). After the input bit is oriented in the desired position, a clocking field rotates the remaining magnets into a quasi-stable orientation. Removing the clocking field allows dipolar coupling to antiferromagnetically align the magnets. This causes information from the input bit to cascade along the nanomagnet wire. Therefore, controlling the orientation of the input magnet (0 or 1) allows the control an output magnet and transfer data when the system is clocked. This coupling scheme provides the basic mechanism used to transmit and store information in Bennet clocked NML devices.

A key advantage of NML is its low energy consumption. In NML systems, power dissipation occurs in two primary areas: within the magnetic element, and while generating the clocking field. Importantly, single domain magnets change state through near uniform spin rotation, so the energy dissipated within each magnetic element is very small and due primarily to Gilbert damping instead of domain wall motion.[108] In the limit of adiabatic switching, internal losses can become extremely small and have been predicted to approach Landauer's limit (i.e., 3 zJ at room temperature).[109] Hong et al. recently experimentally confirmed these predictions for an array of nanomagnets using a sensitive magnetometry setup.[110] As energy dissipation within the magnet is quite small, Bennett clocking losses are mainly attributable to the generation of the clocking field itself.

The majority of previous NML work has focused on clocking fields created by passing an electric current through a wire. Electric currents have been used to create magnetic fields that clock either all magnets at once,5,[107],10–13 or operate in specific clocking zones.[115] It has been noted that this clocking scheme dissipates orders of magnitude more energy than losses due to Gilbert damping.[112] This is why optimistic estimates only show 10x efficiency improvements over CMOS for this clocking technique.[116] Additionally, this approach is prone to large error

rates, as thermal fluctuations and slight manufacturing defects can cause premature bit flips in the middle of long nanomagnet chains.[112], [114] While introducing biaxial anisotropy[117] and using concave shapes[118] have both reduced error rates, bit errors still increase as the length of a clocking zone increases and the location of the error is very sensitive to manufacturing defects.[114] This indicates that local / individual control of the nanomagnets is highly desirable, to reduce the clocking zone size and therefore reduce error rates.

Recent efforts have focused on creating energy efficient localized clocking schemes using spin orbit torque, and strain mediated multiferroic heterostructures. A clocking scheme using spin orbit torque was experimentally demonstrated by Bhowmik et al in 2014 that used approximately 100x smaller currents than required for magnetic field based clocking.[119] This corresponds to a 3-4 order of magnitude improvement in energy efficiency. Furthermore, this approach had a 100% success rate, albeit with a very small sample size of only five attempts. Simultaneously, substantial work on strain mediated clocking has indicated it's highly energy efficient nature,[120]–[126] with recent predictions indicating only 1 aJ may be required to flip a bit of information.[126] Therefore, strain mediated clocking is expected to be 2-3 orders of magnitude more efficient than transistor based logic and 1 order of magnitude better than spin orbit clocking. The rest of this chapter will focus on strain mediated clocking.

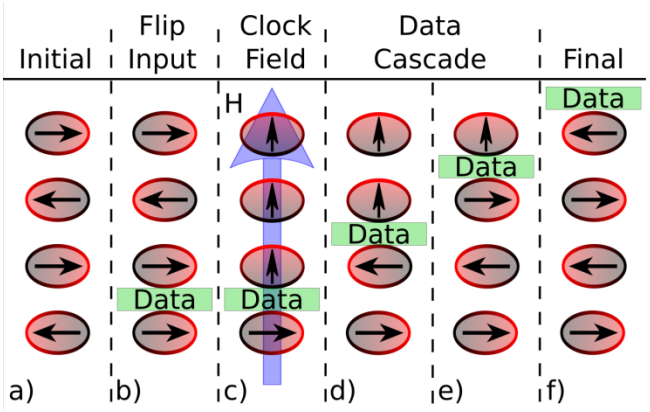

Figure 5-1: Bennett Clocking propagates information along a nanomagnet wire. (a) Initial state from previous computation. (b) The input magnet (bottom magnet), is flipped to a desired value, then (c) a clocking field is applied that causes (d-f) a data cascade due to dipolar interactions, creating (f) a new equilibrium state.

Strain mediated Bennett clocking provides highly localized and energy efficient control of NML devices. This approach deposits magnetoelastic nanomagnetic elements onto a piezoelectric substrate. Applying a voltage to nearby electrodes deformation is induced in the substrate which in turn locally strains the nanomagnet and clocks the magnetization with an effective magnetoelastic field. This approach has the advantage of being able to clock single magnets at a time in a highly energy efficient manner. However, strain mediated Bennett clocking has only recently been experimentally demonstrated, and suffered from high error rates.[126] Several models have been created to analyze error rates in strain mediated approaches, but they predominantly rely on macrospin models using the LLG equations with[125] or without[120]–[124] a stochastic thermal fluctuation field. While the use of macrospin models can be very useful for the initial evaluation of magnetic phenomena, more detailed models are required to aid in the fabrication of practical devices. Macrospin models assume that the magnetization, dipolar coupling field, and applied strain are all uniform throughout each magnetic element, which is a condition not met in actual devices. The predictions of macrospin models can vary substantially from experiments, and more detailed finite element models.[58] This is particularly true for thin film

heterostructures, where effects like shear lag lead to nonuniform strain and magnetization profiles, in contradiction with assumptions of uniformity. This chapter presents a numerical model that fully couples elastodynamics and micromagnetics to provide an in-depth analysis of strain mediated Bennett clocking. Room temperature is considered with no thermal fluctuations in the model. The model shows how incoherent rotations may result from the uniaxial nature of the magnetoelastic coupling.

5.2 Model Setup

The objective of the simulation is to analyze the single-domain rotation behavior of Nickel and Terfenol-D nano-ellipses while Bennett clocking. Figure 5-2 shows the Bennett clocking geometry used in this chapter. Four pairs of nano-ellipses and electrodes are perfectly bonded to a 500 nm thick PZT-5H thin film with platinum ground electrode, mounted on a rigid Si/SiO2 substrate. Figure 5-2 (a) shows a perspective view of the four ellipse/electrode pairs used to form a Bennett clocking wire. Figure 5-2 (b) shows the in-plane dimensions for each ellipse, which are 100 nm × 90 nm with a 10 nm thickness. Each nano-ellipse is centered between the two 10 nm thick 90 nm square Au electrodes. The center-to-center distance between the electrode and the ellipse is 280 nm. The center-to-center distance between adjacent ellipses is 140 nm (i.e., a gap of 50 nm). Above the PZT layer is 1 μm x 1 μm x 500nm of air to capture field propagation. The Si/SIO2 substrate is assumed mechanically rigid and modeled using fixed boundary conditions in the numerical model. Therefore, the entire model, containing the ellipses, electrodes, piezoelectric substrate, and surrounding air, is 1 μm x 1 μm x 1 μm. Under these dimensions and distance between the elements, the energy required for per flip in the Bennett clocking system is 8.7 fJ ($E =$

$\frac{1}{2}QV$where V is the voltage on the electrodes and Q is the total charge for the period of time that the voltage is applied on the electrodes).

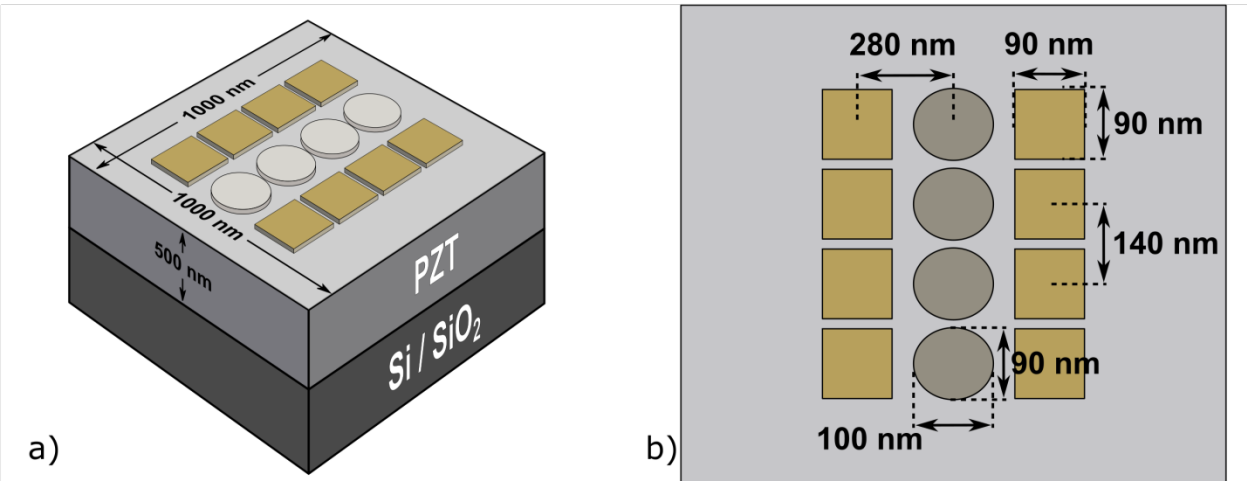

Figure 5-2: The geometry settings of the model. Four ellipses form a line with their electrodes, with the distance between every 2 ellipses is 140 nanometers. Every ellipse has the same aspect ratio (0.9). The 1000nm cross 1000nm's PZT layer lies on a silicon layer. When positive or negative voltage is applied to the electrodes one by one, the PZT layer will produce enough strain to help change the shape anisotropy and drive the circuit.

Two magnetic materials were studied in this chapter, the material properties for Nickel and Terfenol-D are shown in Table 5-1. The Nickel and Terfenol-D nano-ellipses were assumed polycrystalline, therefore crystalline anisotropy is neglected. Our model shows that in this caes, the Gilbert damping do not influence the final states and general trends but dramatically improve the calculation complexity. In this situation, the Gilbert damping ratio is set as $\alpha = 0.5$ to improve model stability and reduce run time for numerical purposes.[127] The final equilibrium state is not affected by this compromise. Transversely isotropic PZT-5H is modeled with piezoelectric coefficient $d_{33} = 5.93 \times 10^{-10}$ C/N, $d_{31} = -2.74 \times 10^{-10}$ C/N, stiffness $c_{11} = c_{22} = 127$ GPa, $c_{12} = 80.2$ GPa, $c_{13} = c_{23} = 84.6$ GPa, $c_{33} = 117$ GPa, $c_{44} = c_{55} = 22.9$ GPa, and density $\rho = 7500$ kg/m^3. The z-direction is treated as the transverse c-axis. Young's modulus and Poisson's ratio for the Au electrodes are $E = 70$ GPa and $\nu = 0.44$, respectively.

Table 5-1: Simulated Material Properties.

Parameter	Description	Units	Nickel	Terfenol-D
M_s	Saturation Magnetization	A/m	4.8×10^5	8×10^5
A_{ex}	Exchange Stiffness	J/m	1.05×10^{-11}	1×10^{-11}
L_{ex}	Exchange Length	nm	8.5	5
λ_s	Saturation Magnetostriction	-	-34×10^{-6}	1200×10^{-6}
E	Young's Modulus	GPa	180	80
ρ	Density	kg/m^3	8900	9210
ν	Poisson's Ratio	-	0.3	0.3

The boundary conditions and element discretization are as follows. Zero-displacement boundary conditions were applied to all four sides and the bottom surface of the piezoelectric film. The bottom surface was also electrically grounded. The top surface of the piezoelectric layer is free to deform and interact with the Bennett clocking wire. The nano-ellipses are discretized using tetrahedral elements with element size on the order of exchange length $L_{ex} = \sqrt{2A_{ex}/\mu_0 M_s^2}$. The remainder of the structure (i.e., PZT-5H thin film, Au electrodes) is discretized using tetrahedral elements with graded element sizes dependent upon local geometry.

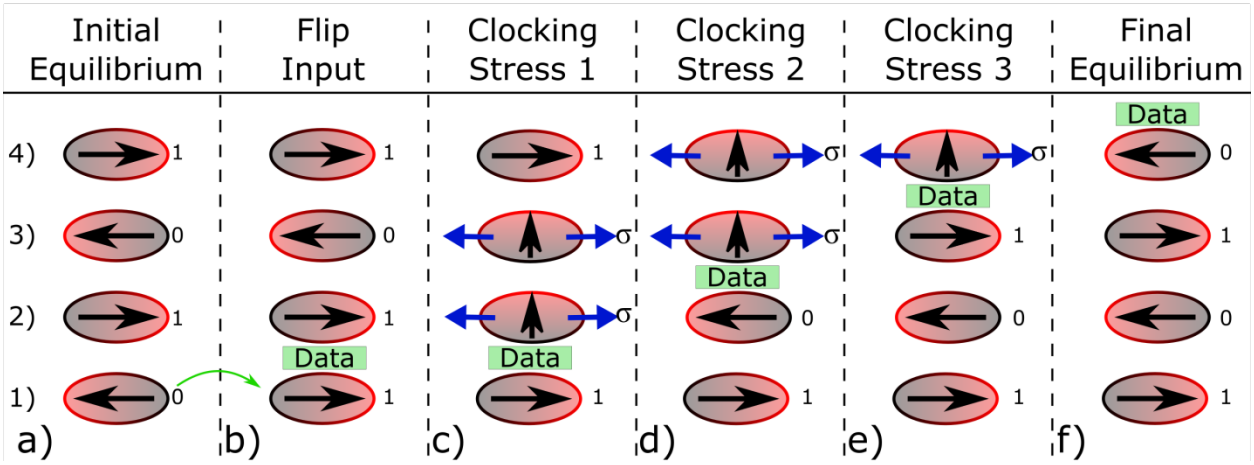

Figure 5-3: Strain mediated Bennett clocking. a) Initial equilibrium position from previous computation. b) An input signal flips ellipse 1 and initiates the clocking sequence. c) Stress is applied to ellipses 2 and 3 to create an easy axis perpendicular to the initial magnetization. d) The voltage is advanced one ellipse, allowing dipolar coupling to flip ellipse 2. e) The process is repeated to flip ellipse 3, and then ellipse 4. f) The final equilibrium positions.

Figure 5-3 shows a schematic of the strain mediated Bennett Clocking control sequence modeled in this chapter. In a classical logic circuit, the goal is to process information from one element to another. Therefore, if ellipse 1 is made to switch from 0 to 1 (i.e., an input signal switches its magnetization from left to right), the goal is to make ellipse 4 switch accordingly. Figure 5-3 (a) shows the system's initial antiferromagnetic equilibrium state with zero strain (voltage) applied. When ellipse 1 rotates to the right, ellipse 2 does not spontaneously flip to the left because dipole coupling with ellipse 1 is too weak to overcome the combined energy barrier from shape anisotropy and dipole coupling with ellipse 3. To flip ellipse 2, magnetoelastic anisotropy is used to eliminate the energy barrier, and allow dipolar coupling to rotate the magnetization. Figure 5-3 (c) shows anisotropic strain is applied to ellipse 2 and 3 by applying a voltage to their Au electrodes. This creates an easy axis in the up/down direction, causing the ellipses to rotate as shown in Figure 5-3 (c). The same voltage is then applied to ellipse 4 (Figure 5-3 (d)), while the voltage on ellipse 2 is released. This allows ellipse 2 to antiferromagnetically

couple with ellipse 1 and propagates the data forward one ellipse. This same procedure is repeated to clock subsequent ellipses. Figure 5-3 (f) shows the final equilibrium position following Bennett clocking, illustrating the transfer of information from ellipse 1 to ellipse 4. The simulated clock uses 1V that is sequentially applied to the Au electrodes while the PZT bottom remains electrically grounded (i.e., a 2 MV/m electric field is applied through the PZT film thickness). As Terfenol-D is positive magnetoelastic, and Nickel is negative magnetoelastic, the polarity of the applied voltage is reversed for the two materials.

5.3 Results

This section presents the dynamic response of the Nickel and Terfenol-D Bennett clocking wires. First the Nickel ellipses will be analyzed and shown to rotate coherently when strained. Subsequently, the stronger magnetoelastic coupling in Terfenol-D will lead to faster switching times but becomes nonuniformly magnetized and rotates incoherently.

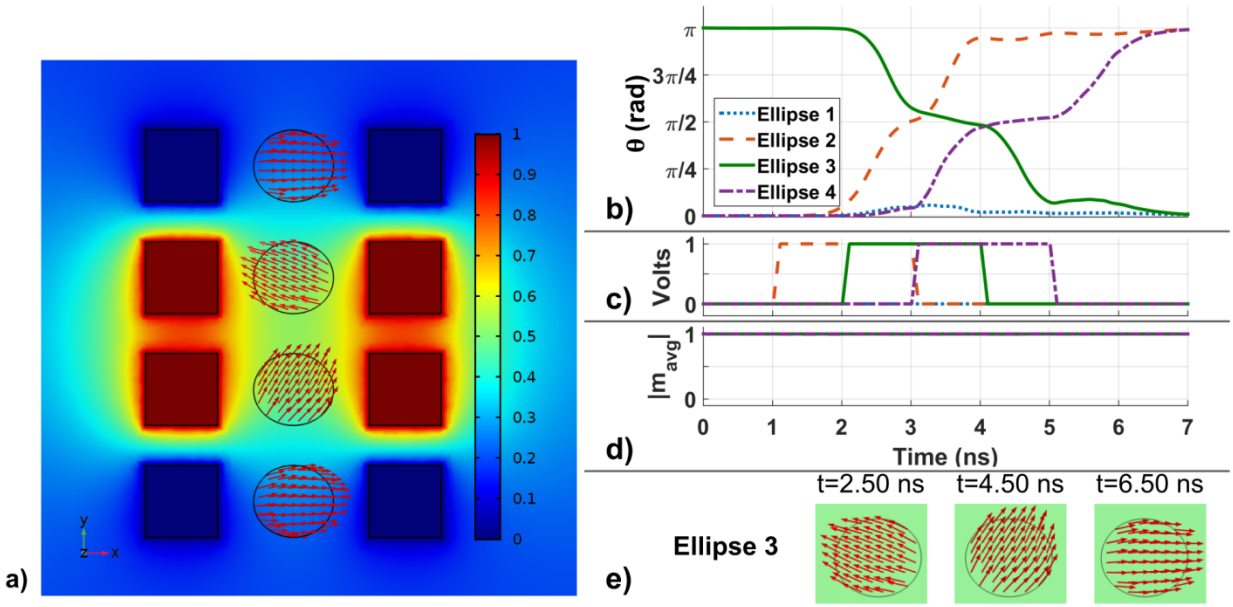

Figure 5-4: Results for Nickel Bennett clocking. (a) Entire Nickel Bennett clocking wire at t=2.5ns. (b) Magnetization rotation angles of four ellipses. (c) Voltage on four electrode pairs. (d) Maximum average magnetization component in four ellipses. (e) Highlight ellipse 3 at t=2.5, 4.5 and 6.5 ns.

Figure 5-4 (a) shows the entire Nickel Bennett clocking wire at t=2.5 ns. The magnetic orientation is indicated with red arrows, while the surface color shows the electric potential. When voltage is applied to the relevant electrode pairs, a tensile strain is generated in the x-direction, creating a magnetoelastic easy axis in the y-direction. As a result, the magnetization in ellipses 2 and 3 begins rotating into the y-direction. Based on the voltage distribution shown in the figure, it can clearly be seen that the piezoelectric strain is highly localized on the space between each electrode pair and does not affect the magnetic orientation of adjacent ellipses.

Figure 5-4 (a) to (e)show a summary of the entire Bennett clocking sequence for the Nickel ellipses. Figure 5-4 (b) shows the average rotation angle (θ) for each of the four ellipses as a function of time. Figure 5-4 (c) shows the voltage on each electrode pair as a function of time. Each ellipse shows a three-stage switching behavior, corresponding to turning the voltage on, the

constant voltage dwell time, and turning the voltage off. By t=7 ns, each ellipse has successfully rotated 180 degrees, and the Bennett clocking wire finishes in a stable antiferromagnetic arrangement. It takes approximately 1 ns apiece for ellipses 2 and 3 to rotate 90 degrees when voltage is applied and creates a magnetoelastic easy axis. Another 1 ns is taken to rotate the final 90 degrees when the voltage is turned off, and the combination of dipole coupling, and shape anisotropy forces each ellipse to antiferromagnetically couple. It takes approximately 1 ns for ellipse 4 to rotate when voltage is turned on, but 2 ns to rotate its final 90 degrees. Due to use of a large Gilbert damping coefficient, it is anticipated that actual materials may flip faster than reported here, but also exhibit transient oscillations prior to stabilizing.

Figure 5-4 (d) and (e) highlight the coherent magnetization rotation in the Nickel ellipses. Figure 5-4 (d), shows the magnitude of the maximum average in-plane magnetization component in each ellipse, defined by

$$\left|m_{avg}\right| = \sqrt{m_{avg,x}^2 + m_{avg,y}^2 + m_{avg,z}^2} \quad \text{(Eq. 1)}$$

where $m_{avg,x}$, $m_{avg,y}$ and $m_{avg,z}$ are the average components in the x, y and z directions. For a coherent / uniform configuration, a magnitude of $\left|m_{avg}\right| = 1$ indicates all spins are in-plane and pointing in the same direction. While for an incoherent / nonuniform configuration, spins partially cancel each other and therefore the average component in each direction is reduced. As a result, a reduction $\left|m_{avg}\right| < 1$ would indicate that some elements' spins are pointing in different directions. The extreme case is $\left|m_{avg}\right| = 0$, which means $\left|m_{avg,x}\right| = \left|m_{avg,y}\right| = \left|m_{avg,z}\right|0$ and all the spins are in random state.[127] It is evident in Figure 5-4 (d) that the average moment always has a magnitude of 1 for each ellipse, indicating coherent rotation at all time steps. This finding is confirmed in Figure 5-4 (e), which highlights ellipse 3 at t = 2.5, 4.5 and 6.5 ns. Each picture

indicates the magnetic moments coherently rotate for the Nickel ellipses. The results in Figure 5-4 indicate a new antiferromagnetic ground state was reached via coherent magnetization rotation, and information was successfully transmitted from ellipse 1 to ellipse 4.

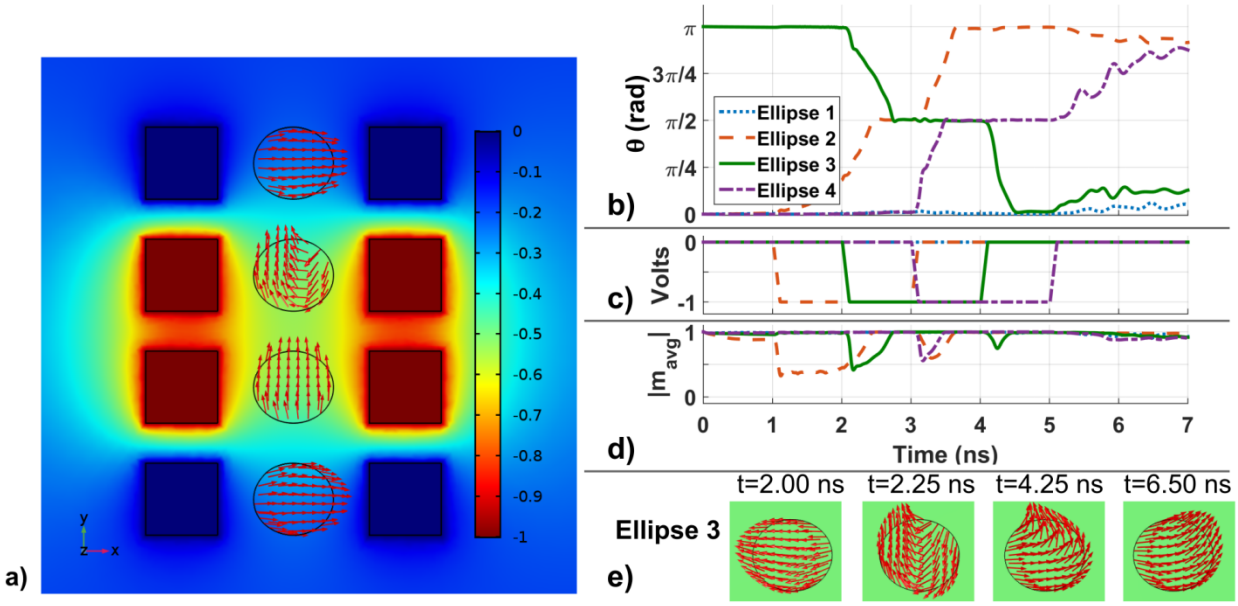

Figure 5-5: Results for Terfenol-D Bennett clocking. (a) Entire Terfenol-D Bennett clocking wire at t=2.5ns. (b) Magnetization rotation angles of four ellipses. (c) Voltage on four electrode pairs. (d) Maximum average magnetization component in four ellipses. (e) Highlight ellipse 3 at t=2.0, 2.25, 4.25 and 6.5 ns.

Figure 5-5 (a) shows the entire Terfenol-D Bennett clocking wire at t=2.5 ns. The magnetic orientation is indicated with red arrows, while the surface color shows the electric potential. When voltage is applied to the relevant electrode pairs, a compressive strain is generated in the x-direction, creating a magnetoelastic easy axis in the y-direction. The applied voltage is of the opposite polarity but same magnitude from the Nickel study (i.e., -1V). A key difference between the Nickel and Terfenol-D studies is evident in this figure, with ellipse 3 clearly rotating in an incoherent manner.

Figure 5-5 (b) and (c) shows a summary of the entire Bennett clocking sequence for the Terfenol-D ellipses. Figure 5-5 (b) shows the average rotation angle (θ) for each of the four ellipses as a function of time. Figure 5-5 (c) shows the voltage on each electrode pair as a function of time. Each ellipse shows the same three step switching behavior seen in the Nickel results. While each ellipse has primarily rotated to the new equilibrium configuration by t=7ns, ellipses 2, 3, and 4 are still approximately 20 degrees from the desired final orientation. Ellipse 2 takes approximately 1.5 ns to initially rotate 90 degrees, but only an additional 0.5 ns to reach its final equilibrium position. Ellipse 3 takes 0.5 ns for both stages of rotation, and ellipse 4 initially takes 0.5 ns, followed by nearly 2ns to reach its final equilibrium. It should be noted that the Terfnol-D rotation speed is nearly twice as fast as the fastest Nickel rotation (i.e., 0.5 ns vs. 1.0 ns).

Figure 5-5 (d) and (e) show the switching in Terfenol-D ellipses was predominantly an incoherent process. The incoherent and vortex phenomenon have been observed in several papers.[128], [129] Figure 5-5 (d) shows that each ellipse becomes non-uniformly magnetized when the strain is applied or released. Non-uniformities lead to incoherent rotation due to the uniaxial nature of magnetoelastic coupling (i.e., up and down are both easy directions when strained). Figure 5-5 (d) shows that even before the first voltage is applied at 1ns, the average moment of ellipse 2 has clearly fallen below 1. This initial nonuniform magnetization occurs due to larger dipolar coupling between the ellipses and internal demagnetization energy as compared to the one experienced with Nickel. The M_s of Terfenol-D is 1.6 times larger than Nickel's, but the exchange constant is nearly equal. This increases the ratio of demagnetization and dipolar energy to the exchange anisotropy and leads to a nonuniform ground state. Figure 5-5 (e) shows that with the existence of residual strain caused by magnetoelastic, effects at t=2 ns, ellipse 3 is non-uniformly magnetized, with the left half canted up and right half canted down. Given that

$B_1 = B_2 = \frac{3E\lambda_s}{2(1+\nu)}$, where B_1 and B_2 are the magnetoelastic coupling coefficients[127], considering Terfenol-D's extremely high λ_s, Terfenol-D's magnetization will be very sensitive to any input strain. Because of the non-straight initial state (left half canted up and right half canted down), magnetoelastic anisotropy forces the left half to point up and the right half to point down when the ellipse is subsequently strained, creating an unstable domain wall in the ellipse (t=2.25ns frame of Figure 5-5 (e)). When this happens, every single magnetization spin finds its shortest way to reach the local minimum state of total energy.[108] After some time, the dipole-dipole effect between magnets forces the magnetization spins to come to the global minimum point of the total energy and switching is completed. The total switching time is then dependent on the time it takes the domain-wall-like magnetization to propagate across the ellipse and restore a stable equilibrium configuration. Propagation of the unstable domain wall explains the initially slow 1.5 ns switching time for ellipse 2. At t=7 ns, the ellipses have rotated the majority of the way into a new antiferromagnetic ground state but are approximately 20 degrees from the desired alignment. Importantly, these observations cannot be made with the macrospin models prevalent in this field, and instead, requires analysis of the spatial and temporal magnetization distribution in each ellipse. This model simulates a similar recent work by Atulasimha et. al[129], [130] but also including strain feedback. by modeling nonuniform elastodynamics interactions in each ellipse, instead applying spatially uniform uniaxial anisotropies to simulate strain.

It should be highlighted that the incoherent rotation seen in the Terfenol-D ellipses can be ameliorated with further device design. By shrinking the overall dimensions of each ellipse and adjusting the inter-ellipse spacing, both the demagnetization and dipolar energies can be reduced to achieve the uniform magnetization profiles seen in the Nickel study. This will reduce the time

for unstable domain propagation out of the ellipse and further improve switching times and device reliability.

5.4 Conclusion

This chapter uses a numerical model which fully couples elastodynamics and micromagnetics to examine Nickel and Terfenol-D Bennett clocking wires. Nickel ellipses rotated in a coherent manner and produced a stable antiferromagnetically coupled ground state after the wire was clocked. Terfenol-D ellipses were capable of rotating nearly twice as fast as Nickel but were also highly susceptible to incoherent rotations. The larger saturation magnetization for Terfenol-D resulted in non-uniformly magnetized equilibrium states that subsequently led to incoherent rotations. The observations made in this study highlight the need for advanced models that examine the spatial magnetization distribution, in contrast to macrospin modeling. Finally, it was hypothesized that decreasing the size of the Terfenol-D ellipses and altering the inter-ellipse distance will prevent the nonuniformities from initiating incoherent behavior. The incoherent flip indicates that because of the large saturation magnetization of Terfenol-D, the system is much more sensitive to strain compared with Ni system. This should facilitate the use of Terfenol-D in Bennett clocking devices.

6. High Frequency Nano Magnetization Switch

6.1 Introduction

In the last couple of decades, considerable research has been conducted on how to perform magnetization switching in the nanoscale due to its promise for applications in magnetic memory and magnetic logic. Switching has previously been achieved using current-induced spin transfer torque (STT), spin orbit torque (SOT).[19], [42]–[45], [131]–[135] However, a successful switch using these methods is usually accompanied by substantial resistive heat losses resulting in inefficiencies. For this reason, eliminating the need for electric current in switching methods is of great importance. An alternative to this, is using voltage-controlled methods. A promising example of such, is using strain-mediated multiferroic composites (ferromagnetic–ferroelectric heterostructure) due to their ultra-high energy efficiency.[12,21,22,13–20] Wang et al. have shown that using strain-mediated multiferroic composites with perpendicular magnetic anisotropy (PMA) can be used to achieve 180 degree magnetization switching.[66], [100] However, these structures have limited switching frequencies and there are very few approaches that can be used to increase their performance. The most commonly used method is increasing the input voltage to the system, but this sacrifices the energy efficiency of these strain-mediated multiferroic structures.

One of the main reasons for the limitation of the switching speed in strain-mediated PMA structures is the incoherence at the beginning of the switching process. Some portions of the magnet switch before the others. In order to avoid this, the breaking of structural symmetries in the nanomagnetic system has attracted substantial interest. This symmetry-breaking gives the magnetization a preferable switching direction. Previous researchers have demonstrated several

methods for breaking this magnetization switch symmetry. [42], [138], [139] One approach is using a sloped surface to help break the structural symmetry and this has been shown to work experimentally. [42] However, there is currently little simulation work done on this symmetry-breaking for 180-degree PMA switching. In addition, most simulations previously done on micromagnetics systems only consider one-way coupling from mechanical strain to magnetization.[140]–[142] To address this, we've created a model that reflects the influence of magnetization change on strain distribution. This change makes noticeable differences in the magnetoelastic behavior of materials.

6.2 Model Setup

The fully coupled model includes mechanically free boundary conditions for the patterned electrodes and top surface of the PZT layer. The bottom surface is fixed to simulate clamping of the PZT thin film grown on a Si/Pt substrate. To simulate a device fabricated on a larger substrate, roller boundary conditions are placed on all sidewalls. These boundary conditions are chosen to simulate a fabricated device.

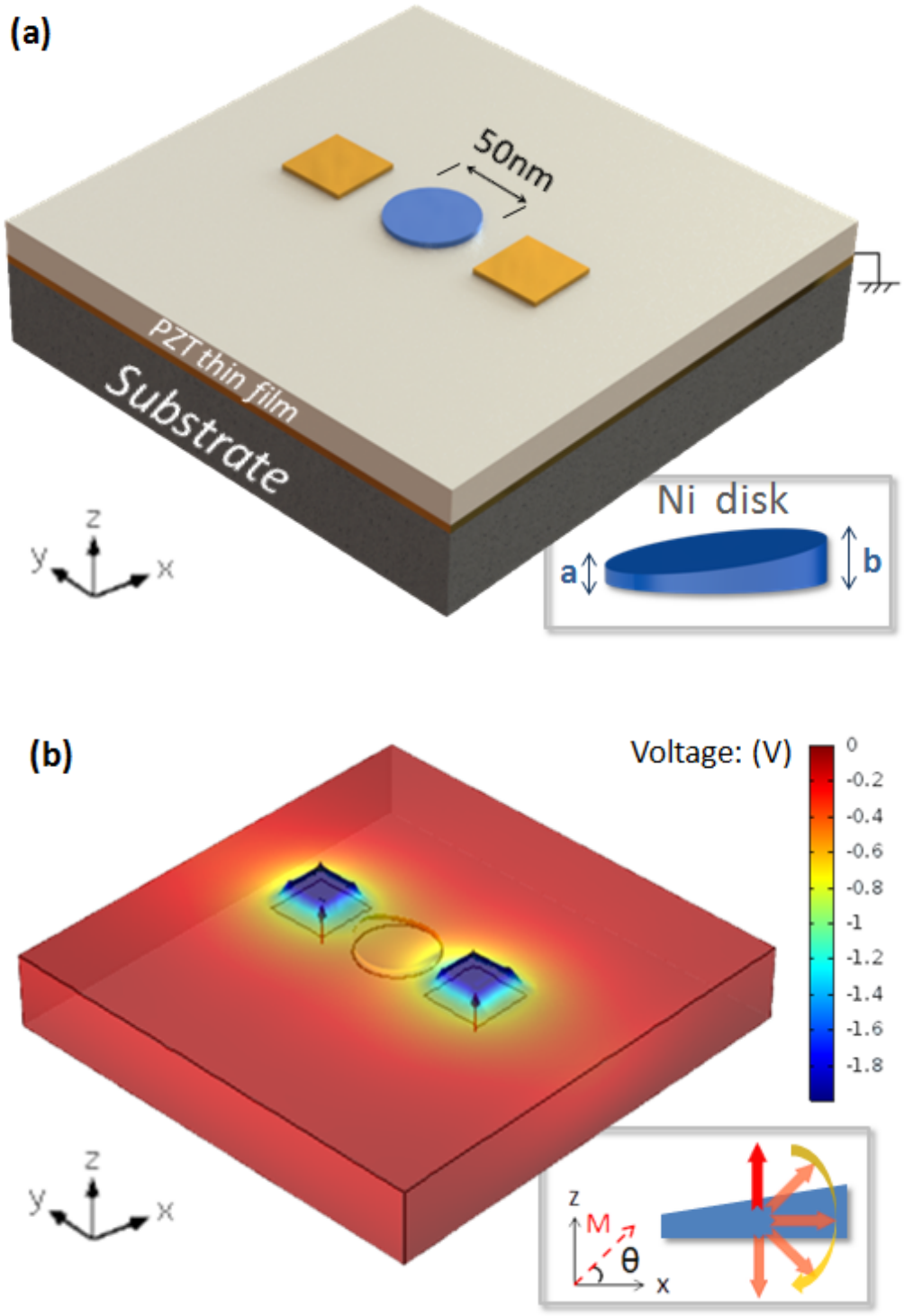

Figure 6-1: (a) Model setup illustration and schematics of the Ni disk. (b) Voltage value with deformation and schematics of 180° precessional magnetization switching.

The Ni/PZT island structure of the MTJ system is shown schematically in Figure 6-1 (a) including a Ni disk with non-uniform thickness. The diameter of the disk is fixed at 50nm, and the thickness varies from a (2.5 nm) to b (3.5 nm). The local enlarged image of the disk shows that the thickness varies along $\hat{x}$. The Nickel disk is adhesively attached to the PZT thin film. This disk is originally magnetically pre-poled along $\hat{z}$. Beside the Ni disk, two Au electrodes (50nm×50nm) are located 20 nanometers away from the edge of the disk. The bottom of the PZT film is fixed to a thick Si substrate and electrically grounded. At the same time, roller boundary conditions were applied on the side walls of the PZT which limits their displacement to only the vertical direction.

Figure 6-1 (b) shows the deformation of the electrodes and the Ni disk when negative voltage is applied on the electrodes. The color bar shows the voltage value (V) and the arrows underneath the electrodes indicate the direction of the electrical field: from bottom to up along the $\hat{z}$ axis. This deformation induces tension along $\hat{y}$ and compression along $\hat{x}$ within the nanondisk.[62] Due to the negative $\boldsymbol{\lambda_s}$ and small Gilbert damping of Ni, the magnetization will rotate along $\hat{x}$ and overshoot. By then releasing the voltage at a proper time, 180° magnetic switching can be achieved within the nanodisk, as shown in the inset. As shown in the cross-section view of the Ni nanodisk, the big red arrow indicates the volume average magnetization. If the voltage is applied and released properly, the volume average magnetization will rotate 180 degree. The angle between the volume average magnetization and the $\hat{x}$ axis is defined as θ. As described previously the thickness of the Ni disk is set to 2.5nm-3.5nm originally and can be modified as long as the energy barrier and PMA effects conditions are satisfied. Specifically, the energy barrier should be larger than $40k_BT$ (about 0.2 aJ) to avoid spontaneous magnetization switching and the

thickness should stay in proper range (about 1.5nm-6nm) where the PMA effect dominates.[66] The parameters used in this model are presented in the following Table 6-1[66], [100]:

Table 6-1: Material parameters.

Parameter	Description	Value
$\mathbf{M_s}$	Saturation magnetization	4.8×10^5 (A/m)
$\boldsymbol{\alpha}$	Gilbert damping factor	0.038
$\mathbf{A_{ex}}$	Exchange stiffness	1.05×10^{-11} (J/m)
$\boldsymbol{\lambda_s}$	Saturation magnetostriction coefficient	-34×10^{-6}
E	Young's modulus	219×10^9 (Pa)
$\boldsymbol{\rho}$	Density	8900(kg/m^3)
$\boldsymbol{\upsilon}$	Poisson's ratio	0.31

6.3 Results

6.3.1 Precession of the Magnetization

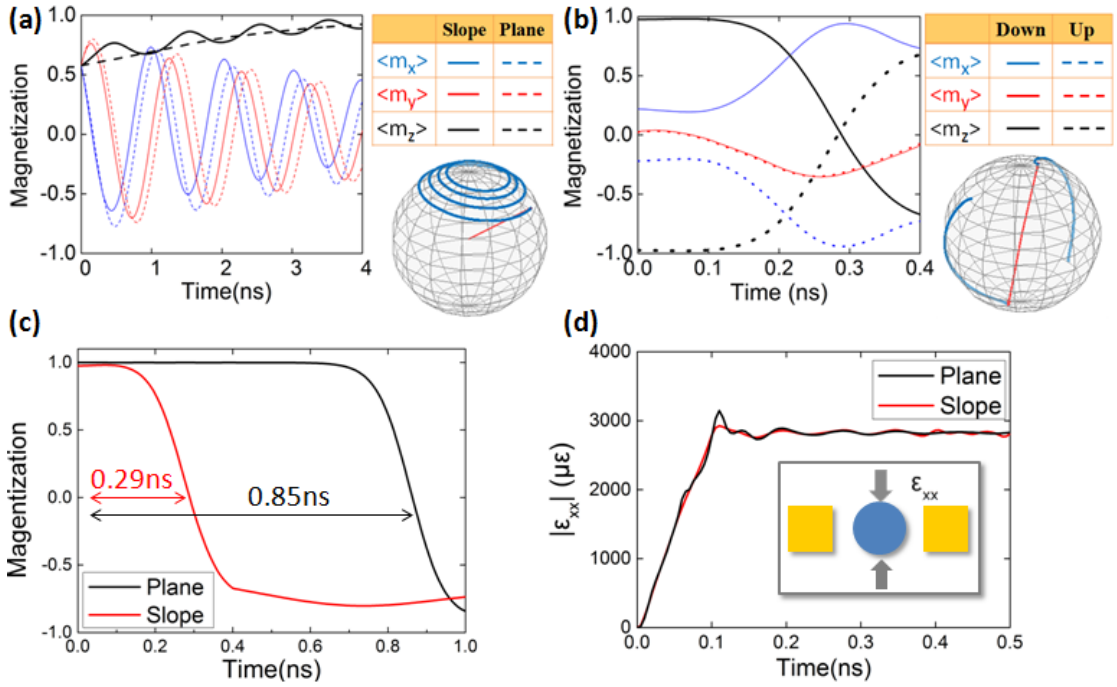

Figure 6-2: (a) Free precession to equilibrium state after releasing from (1, 1, 1) direction of planar and sloped nanodots. (b) Switching up and down process of the sloped nanodot with applied voltage. (c) Switching time comparison of planar and sloped disks when the voltage is released.

Figure 6-2 (a) shows the dynamic response of the normalized magnetization of sloped and planar Ni disks after releasing it from the (1, 1, 1) direction. The solid line represents the dynamic response of the sloped disk while the dashed line represents the planar one. As shown in the figure, the magnetization components m_x, m_y, m_z precess towards the $\hat{z}$ axis with m_x, m_y oscillating. Finally, the magnetization reaches an equilibrium position in the $\hat{z}$ direction. Both the sloped and planar disk equilibrium processes are similar with the one significant difference being that the m_z of the sloped disk does not increase as monotonically as the planar one. In the global plot,

the trace of the volume average magnetization for the sloped disk is shown. Figure 6-2 (b) illustrates the dynamic response of the magnetization for a sloped Ni disk after an electric field is applied. The solid line represents the dynamic response from $\hat{z}$ to $-\hat{z}$ and the dotted line represents the response from $-\hat{z}$ to $\hat{z}$. Again, the global plot shows the trace of the volume average magnetization for the sloped disk. The electric field E_c is applied after the magnetization reaches equilibrium, which is the 0 ns state specifically. The duration of the 40MV/m electrical field application is 0.4ns. The relaxation time RC of PZT film (0.2ps) and the mechanical strain propagation time from the electrodes to the disk (4.0ps) can be assumed negligible. Evidently, for the planar nanodisk, the m_z component of two switching processes is symmetric due to the geometry. However, for the sloped Ni nanodisk, m_x is antisymmetric, indicating that the magnetization always switches clockwise. This is due to the fact that the sloped disk results in broken structural symmetry about $\hat{x}$ axis. Figure 6-2 (c) shows that, under similar strain, the magnetization switching time varies significantly. A large reduction of the switching time is observed in the sloped disk when compared to the planar disk. The planar disk takes 0.85ns (1176MHz) for the volume average magnetization to become in-plane ($m_z = 0$) while the sloped one takes only 0.29ns (3448MHz and 65% faster). Traditionally, for the planar disk, m_z changes little before 0.6ns due to the incoherence of the magnetization switching. In other words, in the planar disk the magnetization hesitates to choose a direction of switching. To increase the switching speed higher voltages would have to be applied.[65] However, for the sloped disk case, the PMA effect in the thicker part is weaker. So that all magnetization spins switch together toward the thicker part of the nanodisk and thus respond much faster. Figure 6-2 (d) shows that, although the nanodot dimension is smaller than the approximate single-domain limit of Nickel ($L_{SD} = 10\sqrt{\frac{2A_{ex}}{\mu_0 M_s^2}} = 85\text{nm}$), strain inside the element still vary with time at the beginning of the switching,

indicating non-uniform strain distribution and incoherent switching which reduce the energy efficiency. However, by breaking the shape symmetry, the sloped nanodot can provide a solution for the dilemma between fast reaction speed and coherence of switching.

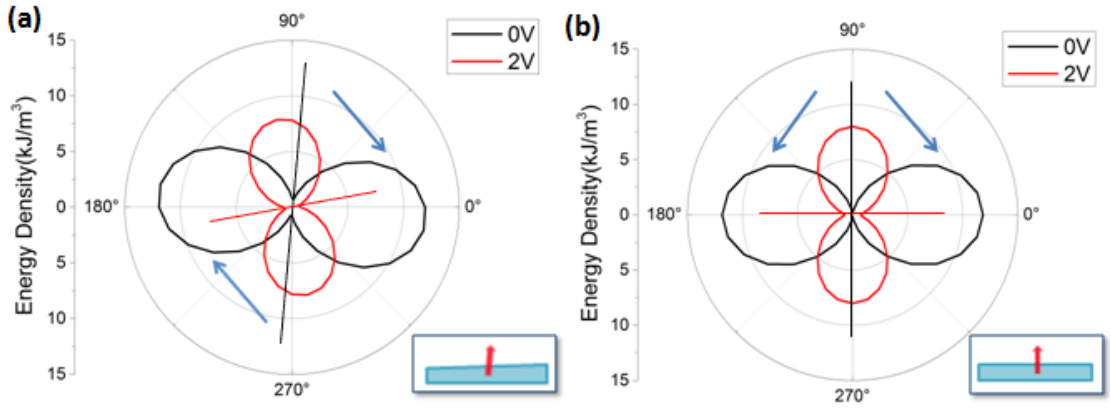

Figure 6-3: (a) Energy profiles in x-z plane of the sloped nanodot before and after the voltage is applied. Black and red lines indicate EA correspondingly. (b) Energy profiles in x-z plane of the planar nanodot.

Figure 6-3 shows the energy profile of sloped and planar elements before and after the voltage is applied. It can provide an explanation for the deterministic rotation from the perspective of energy. From Figure 6-3 (a), the free easy axis (EA) of the sloped disk is along $\theta = 84°$ and the EA with voltage applied is along $\theta = 10°$. The hard axis (HA) is always perpendicular to the EA in each case. This property induced by creating shape anisotropy is a little different from the planar disk whose EA lies along exactly at $\theta = 90°$ and $\theta = 0°$ before and after the magnetization rotation respectively, as can be seen in Figure 6-3 (b). The energy asymmetry can determine the magnetization rotating direction. For example, starting from $\hat{z}$, when the strain is introduced, the volume average magnetization tends to reorient along positive $\hat{x}$ because reaching negative $\hat{x}$ will

require more energy. Similarly, it rotates from $-\hat{z}$ to $\hat{z}$ clockwise. But for the planar disk, rotating through positive $\hat{x}$ or negative $\hat{x}$ needs equal energy. Therefore, incoherence emerges, part of the spins tends to rotate through one direction while others tend to rotate though other direction, and the reaction time is prolonged.

6.3.2 Discussion on the Energy Profiles

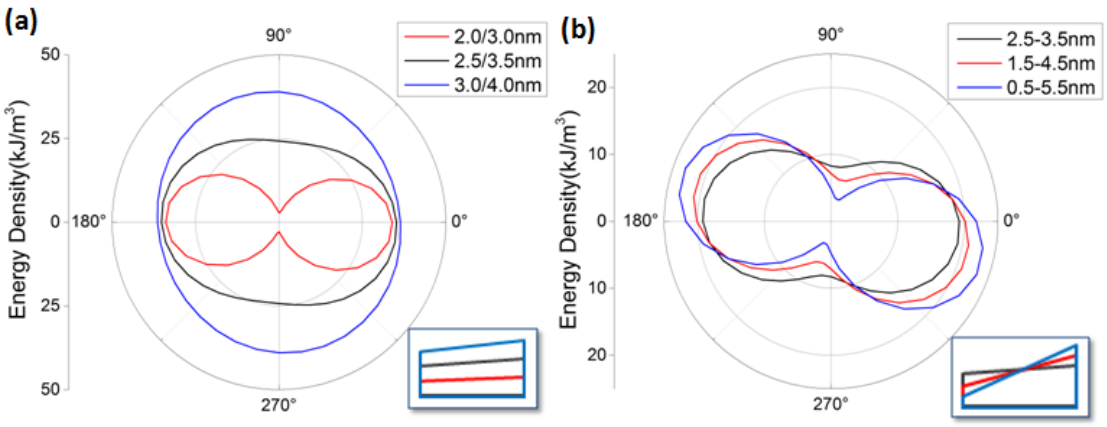

Figure 6-4: Free energy profiles of nanodots with different thickness and inclination.

So far, the article has focused on the dynamic magnetic response of a sloped nanodot. Now we will look at the effect that changing certain geometry parameters of the nanodot (thickness and inclination) will have on the overall performance. Figure 6-4 shows the energy profiles of sloped nanodots with different thicknesses and inclinations. The nanodot schematics are shown in the insets. Setting average thickness to 2.5nm/3nm/3.5nm with a specified height difference value of 1nm between the highest and lowest points, the energy profiles' shape looks different as seen in Figure 6-4 (a). It is important to note that the energy profile shape itself can be changed by adjusting the zero potential energy position. However, putting them in the same plot, we realize that the energy barrier is decreasing when the sloped nanodot becomes thicker. This tendency

matches the former conclusion that the PMA effect is inversely proportional to thickness. The magnetostatic energy will drag the magnetization EA from out-of-plane to in-plane at thickness greater than 6nm in Ni nanodots. The EA direction also changes but is negligible compared to the dramatic change of energy barrier. However, for sloped nanodots with different inclinations, the change of EA direction dominates and has a distinct tendency. In Figure 6-4 (b), the difference value of a and b is set to 1nm/3nm/5nm with the average thickness remaining at 3nm. The EA directions corresponding these inclinations are $\theta = 84°$, $\theta = 76°$, $\theta = 74°$. It is evident that the magnetization tends to become in-plane as the slope of the nanodots become larger. The tendency shown in the data above suggests that the degree of deterministic rotation can be strengthened by breaking the symmetry more drastically. Nonetheless, sharply sloped nanodots are not required to achieve deterministic rotation. Little inclination combined with mild voltage can avoid incoherence, saving both switching time and wasted energy.

6.4 Conclusion

In this chapter, the simulation results demonstrated that under voltage induced strain the magnetization can archive 180-degree OOP switch in Nickel nanodisk. When the symmetry is broken, the switch speed can increase 66% according to the simulation results. Under 40MV/m electrical field, the switch time for plane nanodisk is 0.85ns while for the sloped nanodisk is 0.29ns. This work avoids the trade-off between energy efficiency and coherence of magnetization as traditional way has. Results validate the feasibility that use geometric way to break the symmetry and then avoid the incoherence. However, additional work is required for developing an easy way for fabricating the system shown in this chapter.

Part III

Conclusions

7. Summary and Conclusions

Multiferroic devices set the bridge between electrical field and magnetic field. The advantages of multiferroic devices include high energy efficiency, non-volatile features and small size. A literature review on the development of multiferroic devices was provided in Chapter 1. Based on these advantages, this dissertation focuses on the use of multiferroic systems for high frequency applications, including antenna, logic and memory. For the case of multiferroic antenna applications, inducing vibration of the magnetization to radiate electromagnetic waves has been considered to be a promising way to reduce the antenna's size. Indeed, showing, experimentally, the ability of multiferroic heterostructures to radiate electromagnetic waves is it itself a challenge. Prior work has offered no ability for forming a practical working antenna array. On multiferroic logic and memory, this dissertation focuses on how to improve the working frequency, i.e. response speed of the devices.

For the antenna fabrication aspects of the work introduced in this dissertation, cross-arranged electrodes and magnetoelastic resonators are deposited on the top of a piezoelectric substrate， offering the ability of forming a practical antenna array. The shear wave antenna shows an experimental proof-of-concept on the ability for radiating of such multiferroic heterostructures. The Gold electrodes cooperate with the Nickel resonators to transfer the electromagnetic wave signal into the circuit by transforming it into an acoustic wave or verse versa. The S parameters are tested by the vector network analyzer electronics under different bias fields applied on the multiferroic antenna sample. Further, in order to improve the efficiency of the transformation between electromagnetic waves and acoustic waves, a new antenna design with an energy trap was introduced. This was realized by placing a Bragg mirror under the piezoelectric layer and metal gratings on the sides to reflect as much strain energy as possible. Within the fabrication facilities

available, it was not possible to fabricate a successful Bragg mirror. A compromise design and fabrication process were conducted, showing the ability for improving the transformation efficiency of such cross-arranged multiferroic heterostructures. The fabrication works as well and the test results are presented in chapters 2 and 3, respectively.

The simulation work in this dissertation was performed by both a fully coupled finite element framework and a macro spin framework. The patterned electrodes on the piezoelectric substrate are considered to be able to provide local strain to the nanomagnets. By architecting the geometric shape of nanomagnets as well as the relative position of the electrodes, the multiferroic heterostructures can perform as antenna, logic and memory devices. For example, the local strain controlled multiferroic antenna can adjust its radiating frequency and volume of magnetic material for more application scenarios.

The study on the multiferroic heterostructures used on logic applications gives also a new concept on improving the frequency of the logic system. The broken symmetry of the nanomagnets offers a much faster non-volatile memory device. The simulation works are presented in chapters 4, 5 and 6, respectively.

In summary, the present work provides a path for future antenna array structures with extremely small size and good efficiency. Even if this research did not provide a working prototype for the improved design, due to fabrication limitations, shows the potential of the technology. Fabrication techniques have to be improved as a critical step for bringing the multiferroic antenna technology towards commercial industry usage. Based on the proof of concept and the simulation work presented in this work, we attain the necessary insight and tools to improve existing designs in the future. Thus, this work brings the novel high frequency multiferroic devices closer to reality.

8. References

[1] H. Hertz, *Electric Waves*. Macmillian and Company, 1893.

[2] J. C. Maxwell, P. Trans, and R. S. Lond, *A Dynamical Theory of the Electromagnetic Field*, no. January. 1865.

[3] K. B. Alici, F. Bilotti, L. Vegni, and E. Ozbay, "Miniaturized negative permeability materials Miniaturized negative permeability materials," vol. 071121, pp. 2005–2008, 2007.

[4] T. J. Warnagiris, S. Member, and T. J. Minardo, "Performance of a Meandered Line as an Electrically Small Transmitting Antenna," vol. 46, no. 12, pp. 1797–1801, 1998.

[5] A. Erentok and R. W. Ziolkowski, "AN EFFICIENT METAMATERIAL- INSPIRED ELECTRICALLY-SMALL ANTENNA," vol. 49, no. 6, pp. 1287–1290, 2007.

[6] E. E. Altshuler and L. Fellow, "Electrically Small Self-Resonant Wire Antennas Optimized Using a Genetic Algorithm," vol. 50, no. 3, pp. 297–300, 2002.

[7] S. R. Best and S. Member, "The Radiation Properties of Electrically Small Folded Spherical Helix Antennas," vol. 52, no. 4, pp. 953–960, 2004.

[8] A. Planar, "Metamaterial-Inspired Efficient Electrically Small Antennas," vol. 56, no. 3, pp. 691–707, 2008.

[9] K. Van Caekenberghe, N. Behdad, K. M. Brakora, and K. Sarabandi, "A 2 . 45-GHz Electrically Small Slot Antenna," vol. 7, pp. 346–348, 2008.

[10] S. Lim and H. Ling, "Design of thin , efficient , electrically small antenna using multiple

foldings," vol. 42, no. 16, pp. 6–8, 2006.

[11] R. W. Ziolkowski and A. An, "An Efficient , Electrically Small Antenna Designed for VHF and UHF Applications," vol. 7, pp. 217–220, 2008.

[12] A. Ibraheem, "Implanted Antennas and Intra-Body Propagation Channel for Wireless Body Area Network Implanted Antennas and Intra-Body Propagation Channel for Wireless Body Area Network," *Thesis*, 2014.

[13] J. Faerber, G. Cummins, and M. P. Y. Desmulliez, "Design of conformal wideband antennas for capsule endoscopy within a body tissue environment," *Eur. Microw. Week 2016 "Microwaves Everywhere", EuMW 2016 - Conf. Proceedings; 46th Eur. Microw. Conf. EuMC 2016*, pp. 1223–1226, 2016.

[14] P. Soontornpipit, "Design of an Implantable Antenna Feasibility Study for Continuous Glucose Monitoring," *ECTI Trans. Electr. Eng., Electron. Commun.*, vol. 12, no. 1, pp. 44–52, 2014.

[15] S. Tehrani ; J.M. Slaughter ; E. Chen ; M. Durlam ; J. Shi ; M. DeHerren, "Progress and outlook for MRAM technology," *IEEE Trans. Magn.*, vol. 35, no. 5, pp. 2814–2819, 1999.

[16] Cai Chen, "Simulation and Optimization for Strain-Mediated Multiferroic Applications: Memory, Logics and Sensor/Actuator," 2018.

[17] M. Liu, J. Lou, S. Li, and N. X. Sun, "E-field control of exchange bias and deterministic magnetization switching in AFM/FM/FE multiferroic heterostructures," *Adv. Funct. Mater.*, vol. 21, no. 13, pp. 2593–2598, 2011.

[18] J. P. Domann, “On Magnetoelastodynamics,” University of California, Los Angeles, 2017.

[19] K. L. Wang, J. G. Alzate, and P. Khalili Amiri, “Low-power non-volatile spintronic memory: STT-RAM and beyond,” *J. Phys. D. Appl. Phys.*, vol. 46, no. 8, 2013.

[20] B. C. Regan, S. Aloni, K. Jensen, R. O. Ritchie, and A. Zettl, “Nanocrystal-powered nanomotor,” *Nano Lett.*, vol. 5, no. 9, pp. 1730–1733, 2005.

[21] Y. Chu, L. W. Martin, M. B. Holcomb, R. Ramesh, M. S. Division, and L. Berkeley, “Controlling magnetism with multiferroics Multiferroics , materials combining multiple order parameters , offer an,” *Mater. Today*, vol. 10, no. 10, pp. 16–23, 2007.

[22] L. W. Martin, S. P. Crane, C. A. F. Vaz, D. Sando, and M. Bibes, “Spintronics with multiferroics,” vol. 3, 2008.

[23] B. G. Catalan and J. F. Scott, “Physics and Applications of Bismuth Ferrite,” pp. 2463–2485, 2009.

[24] K. F. Wang, J. Liu, and Z. F. Ren, “Advances in Physics Multiferroicity : the coupling between magnetic and polarization orders,” vol. 8732, no. November, 2017.

[25] J. T. Heron, “Electric Field Control of Ferromagnetism and Magnetic Devices Using Multiferroics,” University of California, Berkeley, 2013.

[26] Y. LU, “ELECTRICAL CONTROL OF FERROMAGNETISM IN MULTIFERROIC BISMUTH FERRITE-BASED HETEROSTRUCTURES,” Nanyang Technological University, 2011.

[27] N. A. Spaldin and M. Fiebig, “The Renaissance of Magnetoelectric Multiferroics,” vol. 309,

no. July, pp. 391–393, 2005.

[28] W. Eerenstein, N. D. Mathur, and J. F. Scott, “Multiferroic and magnetoelectric materials,” vol. 442, no. August, pp. 759–765, 2006.

[29] S. State and P. Related, “Temperature dependence of the crystal and magnetic structures of BiFeO 3,” 1980.

[30] T. Kimura, S. Kawamoto, I. Yamada, M. Azuma, M. Takano, and Y. Tokura, “Magnetocapacitance effect in multiferroic BiMnO 3,” pp. 2–5, 2003.

[31] O. Lufe *et al.*, “Ferroelectricity from iron valence ordering in the,” vol. 436, no. August, pp. 1136–1138, 2005.

[32] I. K. Yang, J. Kim, S. H. Lee, S. Cheong, and Y. H. Jeong, “scanning probe microscopy Charge ordering , ferroelectric , and magnetic domains in LuFe 2 O 4 observed by scanning probe microscopy,” vol. 152902, no. 2015, 2017.

[33] T. Lottermoser, T. Lonkai, U. Amann, and M. Fiebig, “Magnetic phase control by an electric field,” vol. 193, no. May, pp. 541–544, 2004.

[34] E. F. Bertaut, R. Pauthenet, and M. Mercier, *Proprietes magnetiques et structures du manganite d’yttrium*, vol. 7. 1963.

[35] J. P. Joule, “On a new class of magnetic forces,” vol. 8, pp. 219–224, 1842.

[36] E. Villari, *Intorno alle modificazioni del momento magnetico di una verga di ferro e di acciaio, prodotte per la trazione della medesima e pel passaggio di una corrente attraverso la stessa*, no. 2. 1864.

[37] Y. Wang, J. Hu, Y. Lin, and C. Nan, “Multiferroic magnetoelectric composite nanostructures,” vol. 2, no. 2, pp. 61–68, 2010.

[38] A. Clark, R. Bozorth, and B. Desavage, “Anomalous thermal expansion and magnetostriction of single crystals of dysprosium,” 1976, no. December.

[39] J. J. Rhyne and S. Legvold, “Magnetostriction of tb single crystals,” vol. 509, no. 1962, 1965.

[40] A. E. Clark and H. S. Belson, “Giant room-temperature magnetostrictions in TbFe2 and DyFe2,” vol. 5, no. 9, pp. 2–4, 1972.

[41] A. Barthélémy *et al.*, “Magnetoresistance and spin electronics,” *J. Magn. Magn. Mater.*, vol. 242–245, no. PART I, pp. 68–76, 2002.

[42] G. Yu *et al.*, “Switching of perpendicular magnetization by spin-orbit torques in the absence of external magnetic fields.,” *Nat. Nanotechnol.*, vol. 9, no. May, p. 548, 2014.

[43] S. Fukami, T. Anekawa, C. Zhang, and H. Ohno, “A spin–orbit torque switching scheme with collinear magnetic easy axis and current configuration,” *Nat. Nanotechnol.*, vol. 11, no. 7, pp. 621–625, 2016.

[44] A. Brataas, A. D. Kent, and H. Ohno, “Current-induced torques in magnetic materials,” *Nat. Mater.*, vol. 11, no. 5, pp. 372–381, 2012.

[45] L. Liu, C.-F. Pai, Y. Li, H. W. Tseng, D. C. Ralph, and R. A. Buhrman, “Spin-Torque Switching with the Giant Spin Hall Effect of Tantalum,” *Science (80-.).*, vol. 336, no. 6081, pp. 555–558, 2012.

[46] Z. Diao *et al.*, "Spin-transfer torque switching in magnetic tunnel junctions and spin-transfer torque random access memory Spin-transfer torque switching in magnetic tunnel junctions and spin-transfer torque random access," 2007.

[47] T. Maruyama *et al.*, "Large voltage-induced magnetic anisotropy change in a few atomic layers of iron," *Nat. Nanotechnol.*, vol. 4, no. 3, pp. 158–161, 2009.

[48] W.-G. Wang, M. Li, S. Hageman, and C. L. Chien, "Electric-field-assisted switching in magnetic tunnel junctions," *Nat. Mater.*, vol. 11, no. 1, pp. 64–68, 2011.

[49] R. Ramesh and N. A. Spaldin, "Multiferroics: progress and prospects in thin films," *Nat. Mater.*, vol. 6, no. 1, pp. 21–29, 2007.

[50] J. P. Domann, W. Y. Sun, L. T. Schelhas, and G. P. Carman, "Strain-mediated multiferroic control of spontaneous exchange bias in Ni-NiO heterostructures," *J. Appl. Phys.*, vol. 120, no. 14, 2016.

[51] A. K. Biswas, H. Ahmad, J. Atulasimha, and S. Bandyopadhyay, "Experimental Demonstration of Complete 180° Reversal of Magnetization in Isolated Co Nanomagnets on a PMN-PT Substrate with Voltage Generated Strain," *Nano Lett.*, vol. 17, no. 6, pp. 3478–3484, 2017.

[52] N. D'Souza, M. Salehi Fashami, S. Bandyopadhyay, and J. Atulasimha, "Experimental Clocking of Nanomagnets with Strain for Ultralow Power Boolean Logic," *Nano Lett.*, vol. 16, no. 2, pp. 1069–1075, 2016.

[53] P. K. Nordeen, "High Frequency Dynamics of Magnetoelastic Composites and their Application in Radio Frequency Sensors," University of California, Los Angeles, 2016.

[54] G. Nader, E. Silva, and J. Adamowski, “Effective damping value of piezoelectric transducers determined by experimental techniques and numerical analysis,” *ABCM Symp. Ser. Mechatronics*, vol. 1, pp. 271–279, 2004.

[55] J. D. . I. Larson, S. R. Gilbert, and B. X. B. Xu, “PZT material properties at UHF and microwave frequencies derived from FBAR measurements,” *IEEE Ultrason. Symp. 2004*, vol. 1, no. c, pp. 0–4, 2004.

[56] T. L. Gilbert, “Classics in Magnetics A Phenomenological Theory of Damping in Ferromagnetic Materials,” vol. 40, no. 6, pp. 3443–3449, 2004.

[57] L. Landau and E. Lifshits, “on the Theory of the Dispersion of Magnetic Permeability in Ferromagnetic Bodies,” *Phys. Zeitsch. der Sow.*, vol. 169, no. 14, pp. 14–22, 1935.

[58] C.-Y. Liang *et al.*, “Modeling of magnetoelastic nanostructures with a fully coupled mechanical-micromagnetic model.,” *Nanotechnology*, vol. 25, no. 43, p. 435701, 2014.

[59] C. Chen, A. Barra, A. Mal, G. Carman, and A. Sepulveda, “Voltage induced mechanical / spin wave propagation over long distances Voltage induced mechanical / spin wave propagation over long distances,” vol. 072401, 2017.

[60] C. Y. Liang *et al.*, “Electrical control of a single magnetoelastic domain structure on a clamped piezoelectric thin film - Analysis,” *J. Appl. Phys.*, vol. 116, no. 12, pp. 0–9, 2014.

[61] G. Di Fratta, “The Newtonian potential and the demagnetizing factors of the general ellipsoid,” *Proc. R. Soc. A Math. Phys. Eng. Sci.*, vol. 472, no. 2190, p. 20160197, 2016.

[62] C.-Y. Liang *et al.*, “Modeling of magnetoelastic nanostructures with a fully coupled

mechanical-micromagnetic model," *Nanotechnology*, vol. 25, no. 43, p. 435701, 2014.

[63] C. Liang *et al.*, "Electrical control of a single magnetoelastic domain structure on a clamped piezoelectric thin film - analysis," *Appl. Phys. Lett.*, vol. 44, no. 26, p. 265001, 2014.

[64] C. Chen, A. Barra, A. Mal, G. Carman, and A. Sepulveda, "Voltage induced mechanical / spin wave propagation over long distances," *Appl. Phys. Lett.*, vol. 110, no. 07, p. 072401, 2017.

[65] Q. Wang *et al.*, "Strain-mediated 180° switching in CoFeB and Terfenol-D nanodots with perpendicular magnetic anisotropy," *Appl. Phys. Lett.*, vol. 110, no. 10, pp. 1–6, 2017.

[66] X. Li *et al.*, "Strain-mediated 180° perpendicular magnetization switching of a single domain multiferroic structure," *J. Appl. Phys.*, vol. 118, no. 1, 2015.

[67] J. H. Rowen, F. G. Eggers, and W. Strauss, "Generation of Microwave Electromagnetic Radiation in Magnetic Materials," *J. Appl. Phys.*, vol. 32, no. 3, 1961.

[68] R. D. Mindlin, "Electromagnetic radiation from a vibrating quartz plate," *Int. J. Solids Struct.*, vol. 9, no. 6, pp. 697–702, 1973.

[69] P. C. Y. Lee, "Electromagnetic radiation from an AT-cut quartz plate under lateral-field excitation," *J. Appl. Phys.*, vol. 65, no. 4, pp. 1395–1399, 1989.

[70] P. C. Y. Lee, Y. G. Kim, and J. H. Prevost, "Electromagnetic radiation from doubly rotated piezoelectric crystal plates vibrating at thickness frequencies," *J. Appl. Phys.*, vol. 67, no. 11, pp. 6633–6642, 1990.

[71] Z. Yao, Y. E. Wang, S. Keller, and G. P. Carman, "Bulk Acoustic Wave-Mediated

Multiferroic Antennas: Architecture and Performance Bound," *IEEE Trans. Antennas Propag.*, vol. 63, no. 8, pp. 3335–3344, 2015.

[72] S. Tiwari *et al.*, "Ferromagnetic Resonance in Bulk-Acoustic Wave Multiferroic Devices," vol. 1, no. 1, pp. 420–423, 2016.

[73] S. M. Keller, "Wave Propagation in Multiferroic Materials," University of California, Los Angeles, 2013.

[74] K. P. Wetzlar, "Leveraging anisotropy to enhance multiferroic transduction," University of California, Los Angeles, 2015.

[75] Z. Yao and Y. Ethan Wang, "Dynamic analysis of acoustic wave mediated multiferroic radiation via FDTD methods," *IEEE Antennas Propag. Soc. AP-S Int. Symp.*, pp. 731–732, 2014.

[76] J. P. Domann and G. P. Carman, "Strain powered antennas," *J. Appl. Phys.*, vol. 121, no. 4, 2017.

[77] P. C. Y. Lee, "Electromagnetic radiation from an AT-cut quartz plate under lateral-field excitation," *J. Appl. Phys.*, vol. 65, no. February, pp. 1395–1399, 1989.

[78] P. C. Y. Lee, Y.-G. Kim, and J. H. Prevost, "Electromagnetic radiation from doubly rotated piezoelectric crystal plates vibrating at thickness frequencies," *J. Appl. Phys.*, vol. 6633, no. 1990, 1990.

[79] S. M. Keller, "Wave Propagation in Multiferroic Materials," University of California, Los Angeles, 2013.

[80] T. Nan *et al.*, “Acoustically actuated ultra-compact NEMS magnetoelectric antennas,” *Nat. Commun.*, pp. 1–7, 2017.

[81] L. Arapan, “Thin Film Plate Acoustic Resonators for Frequency Control and Sensing Applications,” Uppsala Universitet, 2012.

[82] Lord Rayleigh, “On waves propagating along the plane surface of an elastic solid,” *Proc. London Math. Soc.*, vol. 17, pp. 4–11, 1885.

[83] J. L. Bleustein, “A new surface wave in piezoelectric materials,” *Appl. Phys. Lett.*, vol. 13, no. 12, pp. 412–413, 1968.

[84] L. D. and M. G. H. R.H.Tancrell, M.B.Schulz, H.H.Barett, “Disperive delay lines using ultrasonic surface waves,” *Proc. IEEE*, vol. 57, no. 6, pp. 1211–1213, 1969.

[85] M. Lakin, K. T. McCarron, and R. Rose, “Solidly mounted resonators,” *Proc. - IEEE Ultrason. Symp.*, pp. 905–908, 1995.

[86] E. Godshalk and G. Bouche, “Bragg Mirror Optimized for Shear Waves,” 2010.

[87] A. Mourachkine, O. V. Yazyev, C. Ducati, and J. P. Ansermet, “Template nanowires for spintronics applications: Nanomagnet microwave resonators functioning in zero applied magnetic field,” *Nano Lett.*, vol. 8, no. 11, pp. 3683–3687, 2008.

[88] S. I. Klselev *et al.*, “Microwave oscillations of a nanomagnet driven by a spin-polarized current,” *Nature*, vol. 425, no. 6956, pp. 380–383, 2003.

[89] F. Badets, L. Lagae, S. Cornelissen, T. Devolder, and C. Chappert, “Injection locked CMOS buffer dedicated to nanomagnetic based voltage controlled oscillator,” *Proc. 15th IEEE Int.*

Conf. Electron. Circuits Syst. ICECS 2008, pp. 190–193, 2008.

[90] P. M. Braganca, B. A. Gurney, B. A. Wilson, J. A. Katine, S. Maat, and J. R. Childress, "Nanoscale magnetic field detection using a spin torque oscillator," *Nanotechnology*, vol. 21, no. 23, 2010.

[91] J. Torrejon *et al.*, "Neuromorphic computing with nanoscale spintronic oscillators," *Nature*, vol. 547, no. 7664, pp. 428–431, 2017.

[92] Z. Zeng *et al.*, "Ultralow-current-density and bias-field-free spin-transfer nano-oscillator," *Sci. Rep.*, vol. 3, pp. 1–5, 2013.

[93] Y. Zhou, H. Zhang, Y. Liu, and J. Åkerman, "Macrospin and micromagnetic studies of tilted polarizer spin-torque nano-oscillators," *J. Appl. Phys.*, vol. 112, no. 6, 2012.

[94] M. D'Aquino, C. Serpico, R. Bonin, G. Bertotti, and I. D. Mayergoyz, "Micromagnetic study of phase-locking in spin-transfer nano-oscillators driven by currents and ac fields," *J. Appl. Phys.*, vol. 109, no. 7, 2011.

[95] Y. Zhou, C. L. Zha, S. Bonetti, J. Persson, and J. Åkerman, "Spin-torque oscillator with tilted fixed layer magnetization," *Appl. Phys. Lett.*, vol. 92, no. 26, pp. 1–4, 2008.

[96] C. H. Sim, M. Moneck, T. Liew, and J. G. Zhu, "Frequency-tunable perpendicular spin torque oscillator," *J. Appl. Phys.*, vol. 111, no. 7, pp. 3–6, 2012.

[97] and R. P. B. Andersen, E. Ringgaard, T. Bove, A. Albareda, "PERFORMANCE OF PIEZOELECTRIC CERAMIC MULTILAYER COMPONENTS BASED ON HARD AND SOFT PZT," no. August, 2000.

[98] R. C. O'HANDLEY, *Modern magnetic materials*. 2000.

[99] M. Liu *et al.*, "Electrically controlled non-volatile switching of magnetism in multiferroic heterostructures via engineered ferroelastic domain states," *NPG Asia Mater.*, vol. 8, no. 9, 2016.

[100] Q. Wang *et al.*, "magnetic anisotropy Strain-mediated 180 switching in CoFeB and Terfenol-D nanodots with perpendicular magnetic anisotropy," *Appl. Phys. Lett.*, vol. 110, p. 102903, 2017.

[101] A. Fanara, U. S. Epa, R. Clark, and R. Duff, "How Small Devices are Having a Big Impact on U.S. Utility Bills."

[102] Nam Sung Kim *et al.*, "Leakage current: Moore's law meets static power," *Computer (Long. Beach. Calif).*, vol. 36, no. 12, pp. 68–75, Dec. 2003.

[103] S. Datta, V. Q. Diep, and B. Behin-Aein, "What Constitutes a Nanoswitch? A Perspective," in *Emerging Nanoelectronic Devices*, Chichester, United Kingdom: John Wiley & Sons Ltd, 2014, pp. 15–34.

[104] C. H. Bennett, "The Thermodynamics of Computation--a Review," vol. 21, no. 12, pp. 905–940, 1982.

[105] A. Imre, G. Csaba, L. Ji, A. Orlov, G. H. Bernstein, and W. Porod, "Majority Logic Gate for Magnetic Quantum-Dot Cellular Automata," *Science (80-.).*, vol. 311, no. 5758, 2006.

[106] W. Porod *et al.*, "Nanomagnet Logic (NML)," Springer Berlin Heidelberg, 2014, pp. 21–32.

[107] K. Roy, "Critical analysis and remedy of switching failures in straintronic logic using Bennett clocking in the presence of thermal fluctuations," *Appl. Phys. Lett.*, vol. 104, no. 1, 2014.

[108] R. P. Cowburn, D. K. Koltsov, A. O. Adeyeye, M. E. Welland, and D. M. Tricker, "Single-Domain Circular Nanomagnets," *Phys. Rev. Lett.*, vol. 83, no. 5, pp. 1042–1045, 1999.

[109] B. Lambson, D. Carlton, and J. Bokor, "Exploring the thermodynamic limits of computation in integrated systems: Magnetic memory, nanomagnetic logic, and the landauer limit," *Phys. Rev. Lett.*, vol. 107, no. 1, pp. 1–4, 2011.

[110] J. Hong, B. Lambson, S. Dhuey, and J. Bokor, "Experimental test of Landauer's principle in single-bit operations on nanomagnetic memory bits," *Sci. Adv.*, vol. 2, no. 3, 2016.

[111] G. H. Bernstein *et al.*, "Magnetic QCA systems," *Microelectronics J.*, vol. 36, no. 7, pp. 619–624, 2005.

[112] M. T. Niemier *et al.*, "Clocking Structures and Power Analysis for Nanomagnet-Based Logic Devices," *Acm*, pp. 26–31, 2007.

[113] F. M. Spedalieri, A. P. Jacob, D. E. Nikonov, and V. P. Roychowdhury, "Performance of Magnetic Quantum Cellular Automata and Limitations Due to Thermal Noise," *IEEE Trans. Nanotechnol.*, vol. 10, no. 3, pp. 537–546, May 2011.

[114] D. Carlton *et al.*, "Investigation of Defects and Errors in Nanomagnetic Logic Circuits," vol. 11, no. 4, pp. 760–762, 2012.

[115] M. Vacca, M. Graziano, and M. Zamboni, "Majority Voter Full Characterization for

Nanomagnet Logic Circuits," *IEEE Trans. Nanotechnol.*, vol. 11, no. 5, pp. 940–947, Sep. 2012.

[116] X. Ju, M. T. Niemier, M. Becherer, W. Porod, P. Lugli, and G. Csaba, "Systolic Pattern Matching Hardware With Out-of-Plane Nanomagnet Logic Devices," *IEEE Trans. Nanotechnol.*, vol. 12, no. 3, pp. 399–407, May 2013.

[117] D. B. Carlton, N. C. Emley, E. Tuchfeld, and J. Bokor, "Simulation studies of nanomagnet-based logic architecture.," *Nano Lett*, vol. 8, no. 12, pp. 4173–4178, 2008.

[118] B. Lambson, Z. Gu, M. Monroe, S. Dhuey, A. Scholl, and J. Bokor, "Concave nanomagnets: Investigation of anisotropy properties and applications to nanomagnetic logic," *Appl. Phys. A Mater. Sci. Process.*, vol. 111, no. 2, pp. 413–421, 2013.

[119] D. Bhowmik, L. You, and S. Salahuddin, "Spin Hall effect clocking of nanomagnetic logic without a magnetic field," *Nat. Nanotechnol.*, vol. 9, no. 1, pp. 59–63, 2013.

[120] J. Atulasimha and S. Bandyopadhyay, "Bennett clocking of nanomagnetic logic using multiferroic single-domain nanomagnets," *Appl. Phys. Lett.*, vol. 97, no. 17, pp. 12–15, 2010.

[121] M. Salehi Fashami, K. Roy, J. Atulasimha, and S. Bandyopadhyay, "Magnetization dynamics, Bennett clocking and associated energy dissipation in multiferroic logic," *Nanotechnology*, vol. 22, no. 30, p. 155201, 2011.

[122] N. D'Souza, J. Atulasimha, and S. Bandyopadhyay, "Four-state nanomagnetic logic using multiferroics," *J. Phys. D Appl. Phys*, vol. 44, pp. 265001–7, 2011.

[123] M. S. Fashami, J. Atulasimha, and S. Bandyopadhyay, "Magnetization Dynamics, Throughput and Energy Dissipation in a Universal Multiferroic Nanomagnetic Logic Gate with Fan-in and Fan-out," *Nanotechnology*, vol. 23, p. 105201, 2012.

[124] N. D'Souza, J. Atulasimha, and S. Bandyopadhyay, "Energy-Efficient Bennett Clocking Scheme for Four-State Multiferroic Logic," *IEEE Trans. Nanotechnol.*, vol. 11, no. 2, pp. 418–425, Mar. 2012.

[125] M. S. Fashami, K. Munira, S. Bandyopadhyay, A. W. Ghosh, and J. Atulasimha, "Switching of dipole coupled multiferroic nanomagnets in the presence of thermal noise: Reliability of nanomagnetic logic," *IEEE Trans. Nanotechnol.*, vol. 12, no. 6, pp. 1206–1212, 2013.

[126] N. D'Souza, M. Salehi Fashami, S. Bandyopadhyay, and J. Atulasimha, "Experimental Clocking of Nanomagnets with Strain for Ultralow Power Boolean Logic," *Nano Lett.*, vol. 16, no. 2, pp. 1069–1075, Feb. 2016.

[127] Q. Wang, J. Z. Hu, C. Y. Liang, A. Sepulveda, and G. Carman, "Voltage-induced strain clocking of nanomagnets with perpendicular magnetic anisotropies," *Sci. Rep.*, vol. 9, no. 1, pp. 1–7, 2019.

[128] Z. Zhao *et al.*, "Giant voltage manipulation of MgO-based magnetic tunnel junctions via localized anisotropic strain: A potential pathway to ultra-energy-efficient memory technology," *Appl. Phys. Lett.*, vol. 109, no. 9, 2016.

[129] D. Bhattacharya, M. M. Al-Rashid, N. D'Souza, S. Bandyopadhyay, and J. Atulasimha, "Incoherent magnetization dynamics in strain mediated switching of magnetostrictive nanomagnets," *Nanotechnology*, vol. 28, no. 1, p. 015202, Jan. 2017.

[130] M. M. Al-Rashid, S. Bandyopadhyay, and J. Atulasimha, "Dynamic Error in Strain-Induced Magnetization Reversal of Nanomagnets Due to Incoherent Switching and Formation of Metastable States: A Size-Dependent Study," *IEEE Trans. Electron Devices*, vol. 63, no. 8, pp. 3307–3313, Aug. 2016.

[131] Z. Diao *et al.*, "Spin-transfer torque switching in magnetic tunnel junctions and spin-transfer torque random access memory," *J. Phys. Condens. Matter*, vol. 19, no. 16, p. 165209, 2007.

[132] D. Bedau *et al.*, "Ultrafast spin-transfer switching in spin valve nanopillars with perpendicular anisotropy," *Appl. Phys. Lett.*, vol. 96, no. 2, pp. 98–101, 2010.

[133] G. E. Rowlands *et al.*, "Deep subnanosecond spin torque switching in magnetic tunnel junctions with combined in-plane and perpendicular polarizers," *Appl. Phys. Lett.*, vol. 98, no. 10, 2011.

[134] Y. Shiota, T. Nozaki, F. Bonell, S. Murakami, T. Shinjo, and Y. Suzuki, "Induction of coherent magnetization switching in a few atomic layers of FeCo using voltage pulses," *Nat. Mater.*, vol. 11, no. 1, pp. 39–43, 2012.

[135] S. Kanai, M. Yamanouchi, S. Ikeda, Y. Nakatani, F. Matsukura, and H. Ohno, "Electric field-induced magnetization reversal in a perpendicular-anisotropy CoFeB-MgO magnetic tunnel junction," *Appl. Phys. Lett.*, vol. 101, no. 12, pp. 2010–2013, 2012.

[136] Y. H. Chu, L. W. Martin, M. B. Holcomb, and R. Ramesh, "Controlling magnetism with multiferroics," *Mater. Today*, vol. 10, no. 10, pp. 16–23, 2007.

[137] W. G. Wang, M. Li, S. Hageman, and C. L. Chien, "Electric-field-assisted switching in magnetic tunneljunctions," *Nat. Mater.*, vol. 11, no. 1, pp. 64–68, 2012.

[138] Q. Wang, J. Domann, G. Yu, A. Barra, K. L. Wang, and G. P. Carman, "Strain-Mediated Spin-Orbit-Torque Switching for Magnetic Memory," *Phys. Rev. Appl.*, vol. 10, no. 3, p. 1, 2018.

[139] J. H. Franken, H. J. M. Swagten, and B. Koopmans, "Shift registers based on magnetic domain wall ratchets with perpendicular anisotropy," *Nat. Nanotechnol.*, vol. 7, no. 8, pp. 499–503, 2012.

[140] J. J. Wang, J. M. Hu, J. Ma, J. X. Zhang, L. Q. Chen, and C. W. Nan, "Full 180° magnetization reversal with electric fields," *Sci. Rep.*, vol. 4, pp. 1–6, 2014.

[141] J. M. Hu *et al.*, "Fast Magnetic Domain-Wall Motion in a Ring-Shaped Nanowire Driven by a Voltage," *Nano Lett.*, vol. 16, no. 4, pp. 2341–2348, 2016.

[142] J. M. Hu *et al.*, "Purely electric-field-driven perpendicular magnetization reversal," *Nano Lett.*, vol. 15, no. 1, pp. 616–622, 2015.